Development of Novel Techniques for Signal Acquisition and Representation on Spherical Manifolds

A Dissertation
Presented By

Wajeeha Nafees
2014-06-0020

In Partial Fulfillment
of the requirements of the degree of
Doctor of Philosophy in
Electrical Engineering

Supervisor: Dr. Zubair Khalid

Department of Electrical Engineering
Syed Babar Ali School of Science and Engineering
Lahore University of Management Sciences
May 2020

To my beloved Parents

Acknowledgements

The work presented in this thesis would not have been possible without the support of a number of individuals and organizations and they are gratefully acknowledged below:

- First and the foremost, I would like to thank Almighty Allah for bestowing His countless blessings and favours upon me and giving me the capabilities and directions to carry out and complete this work.

- My sincere and distinguished thanks goes to my supervisor Dr. Zubair Khalid for being exceptionally helpful and patient throughout my PhD studies. Without his guidance this work would never have been possible. His persistent encouragement and appreciation always boosted my motivational level towards this work. He was always available to help and discuss in detail for which I am very much grateful to him. I also thank him for carefully going through my publication drafts, and helping me in learning the various skills of academic research and technical writing.

- Special thanks to Dr. Jason McEwen for providing remote supervision and guidance in one of the projects covered in this thesis.

- It was my great pleasure to study in the Signal, Image and Video Processing (SIVP) and the Smart Data Systems and Applications (SDSA) groups at the School of Science and Engineering (SSE). I would like to thank my colleagues in the SIVP and SDSA Labs for providing a friendly and supportive research environment.

- Thanks must go to the Office of the Dean, School of Science and Engineering for awarding me the SSE Dean's Office Travel Grant for supporting my visit to attend and present my research paper at the International Conference on Acoustics, Speech, and Signal Processing (ICASSP) held in Brighton, UK in 2019. I would also like to acknowledge the support provided by the Higher Education Commission (HEC) Pakistan's NRPU project funding scheme (Project No. 5925).

- I thank my parents for providing me with prayers and constant support and for babysitting my children every time I was in a difficult situation.

- I also thank all my friends and colleagues who provided me with immense motivation and whose company made this journey of accomplishing this task much easier. A special thanks to my very dear friends Naima Munir and Atiqa Kiani for always being available to help and lifting my spirits during tough times.

- I would like to express my sincere gratitude towards my husband, Fahad, for being the one to motivate me to start the PhD program, and my daughters, Eshal and Mishal, for sacrificing their mummy-time whenever I was overwhelmed with academic commitments. -

Abstract

The study of spherical signal processing methods enables signal analysis in a variety of diverse fields of science and engineering including, but not limited to, planetary sciences, geophysics, acoustics, medical imaging, quantum mechanics, etc. The proposed dissertation is thus directed towards processing and analysis of signals on spherical objects: the sphere $\mathbb{S}^2$ and the ball $\mathbb{B}^3$.

The first part of the thesis focuses on the study of the Slepian concentration problem on the sphere and the ball. We present a generalized formulation of the Slepian concentration problem on the sphere for finding band-limited functions with an optimal concentration in the spatial domain. By introducing weighting functions in the formulation of classical Slepian concentration problem and assigning different values to these weighting functions, we present two variants of the concentration problem namely the *differential* and the *weighted* Slepian concentration problem. For the Slepian problem on the ball, we design a new set of optimal basis functions with an optimality criterion that the bases are simultaneously concentrated in both the spatial and spectral domains. The optimal basis functions are designed as a linear combination of space-limited functions with maximal concentration in the spectral region and band-limited functions with maximal concentration in the spatial region.

In the second part of this thesis, we focus our attention on sampling schemes on the sphere. It is desirable for a sampling scheme and its associated spherical harmonic transform (SHT) algorithm to utilize the least number of samples, exhibit stability, be computationally efficient and have low complexity in order to exactly or accurately represent a band-limited signal on the sphere. We develop novel methods to improve one or more of the aforementioned attributes of the existing sampling schemes on the

sphere. For the optimal-dimensionality sampling scheme, we propose the placement of samples on the sphere such that the matrices involved in the computation of the SHT are well-conditioned, and develop an iterative algorithm which reduces the error by a factor of 10∼100. Using the proposed method, we also investigate the error in such case when only a small part of the sphere is inaccessible to support the signal analysis in applications (e.g., geophysics, cosmology, acoustics) where samples cannot be taken over the whole sphere due to practical limitations. We further propose an antipodally symmetric sampling scheme of optimal dimensionality for the sampling of band-limited signals. The proposed scheme takes (asymptotically) L^2 number of samples for the sampling of spherical signal of band-limit L and computing its SHT accurately. Since the number of samples are asymptotically equal to the degrees of freedom of the signal in harmonic space, the proposed scheme attains optimal spatial dimensionality. We also formulate the SHT associated with proposed sampling scheme. We employ the antipodal symmetry of the sampling points which is exploited to separate the signal into antipodally symmetric and asymmetric components due to which the signal splits in harmonic space into the signals of even and odd spherical harmonic degrees. The exploitation of this splitting in the formulation of the SHT makes our method computationally efficient by a factor of four in comparison with the existing methods developed for sampling schemes that attain optimal spatial dimensionality. Lastly, to support the applications where the measurements can only be taken over spatially limited region on the sphere due to practical limitations, we design a spatially-limited sampling scheme on the sphere for the computation of SHT of band-limited signals. By enclosing the inaccessible region with an (anisotropic) ellipsoidal region followed by the rotation of the region to the pole or the equator, we propose an iso-latitude sampling scheme on the sphere. We also present a method to place the samples over the spatially-limited region such that the SHT can be computed accurately.

We also present a variant of the equiangular sampling scheme which requires fewer number of samples as compared to the current schemes: an exact method with a slight increase in complexity of the associated SHT algorithm.

List of Acronyms

3D	three-dimensional
CMB	cosmic microwave background
dMRI	diffusion magnetic resonance imaging
FFT	fast Fourier transform
GL	Gauss-Legendre
HRTF	head-related transfer function
PSWF	prolate spheroidal wave function
SHT	spherical harmonic transform

Notations

x	scalar variable
$\boldsymbol{x}$	vector variable
$\hat{\boldsymbol{x}}$	unit vector
$\boldsymbol{X}$	matrix variable
$X(x, y)$	element in row x and column y of $\boldsymbol{X}$
$\langle f, g \rangle$	inner product of two variables f and g
$\|(\cdot)\|_2$	Euclidean norm
$\|(\cdot)\|$	absolute value of parameter $(\cdot)$
$\bar{(\cdot)}$	conjugate operation
$(\cdot)'$	transpose operation on vector
$(\cdot)^T$	transpose operation on vector
$(\cdot)^H$	Hermitian (conjugate transpose) operation
$\delta_{p,q}$	Kronecker delta
$\delta()$	Dirac delta function
$(f)_l^m$	spherical harmonic coefficient of degree ℓ and order m

Contents

List of Figures

List of Publications

Journal Articles:

J1. **W. Nafees**, Z. Khalid, and R. A. Kennedy, "Differential and Weighted Slepian Concentration Problems on the Sphere," *IEEE Trans. Signal Process.*, accepted, 2020.

J2. **W. Nafees**, and Z. Khalid, "Efficient Equiangular Sampling Scheme on the Sphere," *IEEE Signal Process. Letters*, (to be submitted), 2020.

J3. **W. Nafees**, Z. Khalid, and J. D. McEwen, "Polar-optimized Equiangular Sampling Scheme on the Sphere," *IEEE Signal Process. Letters*, (to be submitted), 2020.

Conference Papers:

C1. **W. Nafees**, Z. Khalid, and R. A. Kennedy, "An Antipodally Symmetric Optimal Dimensionality Sampling on the Sphere," in *Proc. IEEE Int. Conf. Acoust., Speech and Signal Process., ICASSP'2019*, Brighton, UK, April 2019, pp. 5097–5101.

C2. **W. Nafees**, Z. Khalid, and R. A. Kennedy, "Spatially-Limited Sampling of Band-Limited Signals on the Sphere," in *Proc. IEEE Int. Conf. Acoust., Speech and Signal Process., ICASSP'2018*, Alberta, Canada, April 2018, pp. 4579–4583.

C3. **W. Nafees**, Z. Khalid, R. A. Kennedy, and J. D. McEwen, “Optimal-dimensionality sampling on the sphere: Improvements and variations,” in *Proc. Int. Conf. Sampling Theory and Applications (SampTA)*, Tallin, Estonia, July 2017 pp. 87–91.

C4. **W. Nafees**, Z. Khalid, and R. A. Kennedy, “Signal analysis on the ball: Design of optimal basis functions with maximal multiplicative concentration in spatial and spectral domains,” in *2017 Int. Conf. Systems, Signals and Image Process. (IWSSIP)*, Poznan, Poland, May 2017, pp. 1–5.

C5. **W. Nafees**, and Z. Khalid, “Differential and weighted Slepian functions on the Ball,” in *IEEE Int. Conf. Acoust., Speech and Signal Process., ICASSP'2021*, Toronto, Canada, June 2021, (to be submitted).

Chapter 1

Introduction

1.1 Motivation and Literature Review

The observable universe and most of the celestial bodies can be considered spherical in shape. On the other hand, the smallest existing particles that make up matter are also modeled as spheres. Measurements taken from these sources comprise of data sets in which the samples are inherently defined on the sphere. In the past decades, most of the signal processing techniques and methods were developed for signals defined in one-dimensional time domain, or more recently in the 2D Euclidean domain. There were no signal processing techniques suitable for spherical signals. Consequently, these signals had to be mapped to a two-dimensional plane thus enabling the researcher to use signal processing methods developed for the Euclidean domain. However, a major drawback of this approach was that it did not cater for the curvature of the sphere. As a result, the computations became erroneous and inaccurate. Hence, there was a dire need for the development of novel signal processing methods which could deal with data measured on a sphere or a ball – the spherical signal processing.

Spherical signal processing forms the backbone of a wide variety of fields of science and engineering. It has received tremendous amount of attention over the past two decades as a mainstream tool to explain various phenomena in the fields of geodesy, geomagnetics, acoustics, computer graphics and computer vision, geophysics, cosmology, medical imaging, wireless communications, 3D beamforming, etc (e.g. [3–25]).

Recently, several signal processing methods have been developed and extended from the Euclidean domain to the spherical domain to support signal analysis in these applications. These include convolution [26–28], filtering [29–32], spectrum estimation [4, 33], wavelets on the sphere and ball [13, 20] Slepian concentration problem on the sphere [23, 33, 34] and on the ball [41] and many more [35, 36].

This thesis is predominantly focussed on the formulation and development of signal processing techniques to analyse signals defined on the sphere and the ball (denoted by $\mathbb{S}^2$ and $\mathbb{B}^3$ respectively). In the remainder of this chapter, we first review the previous work on Slepian problem on the sphere and the ball and various sampling techniques on the sphere. Then we discuss the research problems considered in this thesis and finally we provide the summary of our contributions and an outline of this thesis.

1.1.1 Slepian Concentration Problem

According to the uncertainty principle, it is not possible for a signal to have finite support in the time domain and frequency domain simultaneously. In other words, a function that is limited in the spatial (or temporal) domain has an infinite support in the spectral (or frequency) domain and vice versa. However, it is possible to find the maximal concentration of a function in a particular region of one domain while it is strictly limited in the other domain. The problem of finding functions that are optimally concentrated in spatial and spectral domains simultaneously is known as the Slepian concentration problem, which was first proposed in a series of classical papers [37–40] for the one-dimensional time-frequency domain. The orthogonal family of functions, or data tapers, that arise thereby are known as the Prolate Spheroidal Wave Functions (PSWFs) or more commonly as the (classical) Slepian functions on the real line. Although the problem of finding band-limited functions or space-limited functions with maximal energy concentration in spatial or spectral domain, respectively, was solved nearly sixty years ago for one-dimensional case (time and frequency), its generalizations for various geometries, for example sphere [23, 34], ball [41] and two-dimensional space [14], have also been explored over the last two decades.

Owing to their many interesting properties [42], the Slepian functions have found a wide variety of applications in several diverse fields of science and engineering such as information and communication theory [43, 44], signal detection and estimation [45], signal interpolation and extrapolation [46,47], compressed sensing [48], signal recovery and reconstruction [49–51], sampling theory [52–54], neuroscience [55, 56], optics [57], and many more.

The wide applicability of the one-dimensional time-domain Slepian functions motivated researchers to extend this concept to higher dimensions. The authors in [37] laid the foundation for the extension of the concentration problem to the two-dimensional case, i.e., the Cartesian plane [39] where the spatial region in the form of circular disks has been considered. Later, the planar Slepian functions for other geometries and arbitrary regions in general were also explored in [14]. Slepian functions were used to estimate power spectra of time-series data [58]. Extension of this work to two-dimensional space was given by Bronez [59], Liu et. al [61] and Hanssen [60] and, in more general settings, by Daubechies [62].

Despite all these developments, there were some application for which the planar Slepian functions could not be exploited. For instance, in planetary sciences, the use of the two-dimensional planar Slepian functions based on the local flat area approximation was prohibited due to the inherent curved surface of a planet. To support such applications and beyond, the spherical analogue for the one-dimensional Slepian concentration problem was proposed in [23] (herein referred to as the (classical) Slepian concentration problem on the sphere). The authors consider a problem where data is given on a belt on the sphere, not including the polar caps and use the spherical harmonic basis functions to represent a signal in the harmonic domain. Slepian problem on the sphere has also been investigated in [34], where the authors develop the Slepian functions with special attention to applications in geophysics and planetary sciences. The spherical Slepian functions can be computed either in the spectral domain (by solving an algebraic eigenvalue problem) or in the spatial domain (by solving a Fredholm integral equation). The Slepian functions on the sphere have been utilized for applications in geophysics [33,63], cosmology [64], geodesy [65], acoustics [66,67], planetary sciences [34], signal estimation [68,69], spectral analysis [4], hydrology [70], graph theory [71–74], and so on. Furthermore, the Slepian problem has also been extended to the three-dimensional ball, denoted by $\mathbb{B}^3$, [41], wherein the authors have introduced new basis functions for representation of signal in harmonic domain, the Fourier-Laguerre basis functions (to be explained in Section 2.2.2).

The development of efficient algorithms for the computation of the Slepian functions has been widely investigated [33,34,65,75]. For estimating the potential fields of a planet, the spherical Slepian functions provide a more practical solution as compared to the commonly used damped least-squares spherical harmonic approach [65]. The spherical Slepian functions also find applications in geophysics, e.g., in the decomposition of lithospheric magnetic field models [63].

Apart from potential field estimation in geodesy, an important problem arises in cosmology: the estimation of the spectrum of the cosmic microwave background (CMB) radiation. To address this problem several works have appeared in the recent years documenting spectral analysis on the sphere which utilize the Slepian functions [76,77]. These studies indicate that the spectral analysis and estimation have gained fundamental importance for explaining the behaviour of random processes on spherical bodies. However, in some settings one does not have access to, or may simply not be interested in, the value of the function outside some particular region of the sphere (e.g., due to noise contamination). In such cases it is convenient to use the spatially limited data for signal analysis on the sphere [25]. In [64], the authors use Slepian functions to estimate the spectrum of a noisy, isotropic process in a bounded region on the sphere. The Slepian functions have also been used as localization windows for energy spectrum estimation [4,33,68,78].

In a recent work, the Slepian functions have been utilized for the reconstruction of the head-related transfer function (HRTF) on the sphere, where it has been demonstrated that the proposed reconstruction technique allows more accurate results as compared to the methods based on using the conventional spherical harmonic basis functions [67]. Since the Slepian functions optimally reduce the estimation bias and leakage effects in hydrology as compared to other methods, they have been used for deriving estimates of water storage variations in different regions of the Earth using data collected by satellites [70].

1.1.2 Sampling on the Sphere

W. Freeden says in his book "'Spherical Sampling"' [79]:

> *Sampling of a spherical signal has two aspects: first, stating that a band-limited function is completely determined by its samples, second, describing how to reconstruct the signal (or function) using its discrete samples.*

A sampling scheme is a set of rules that define the location points where data is to be sampled on a spherical object. The signal obtained in this manner is said to be in the spatial domain. The harmonic (frequency) content of a signal is studied in the spectral domain, which is enabled by the spherical harmonic transform (SHT) which serves as a counterpart of Fourier transform for analysis of signals on the sphere. To support harmonic domain analysis, the ability to compute spherical harmonic transform of the signal from its samples is of significant importance. Since the acquisition of measurements (samples) is time consuming, it is desirable to have a sample-acquisition strategy which (*i*) takes the minimum possible number of samples for the accurate computation of spherical harmonic transform, (*ii*) exhibits structure in the placement of samples to facilitate the acquisition and (*iii*) has spatially uniform distribution of samples. A large number of sampling schemes and pixelizations on the sphere have been devised in the literature for sampling band-limited signals which result in theoretically exact or accurate computation of the SHT (e.g., see [2, 25, 27, 80–92] and the references therein). Different sampling schemes have different spatial dimensionality (defined as the number of sample points required to (approximately or exactly) compute the SHT and capture the information content of band-limited signals).

For the exact computation of SHTs of a signal band-limited at L (defined in

Section 2.1.4), Driscoll and Healy [27] developed a method which uses $2L-1$ latitude rings where each ring had $2L-1$ samples. This results in $\sim$ (asymptotically) $4L^2$ equiangular samples on the sphere. In comparison, the sampling scheme presented by McEwen and Wiaux [85] requires $\sim 2L^2$ equiangular samples to exactly compute the SHT. The Gauss-Legendre (GL) sampling scheme [85, 93] also requires $\sim 2L^2$ for exact computation of the SHT. The computational complexity of the stable SHT associated with these sampling methods is $O(L^3)$. To the best of our knowledge, there does not exist any theoretically exact sampling scheme with dimensionality less than $\sim 2L^2$.

Recently, an optimal-dimensionality sampling scheme has been proposed in [2] that takes optimal L^2 number of samples equal to the degrees of freedom of the band-limited signal in the harmonic space, for the accurate computation of the SHT of band-limited signals. Optimal-dimensionality sampling has been customized to serve the needs of applications in acoustics [6] and diffusion MRI (dMRI) [25]. Although the SHT associated with this sampling scheme requires the optimal number of samples, the computational complexity of the associated SHT is of the order $O(L^4)$ due to the series of matrix inversions involved in the computation. The samples are placed in iso-latitude rings but appear unstructured and asymmetric around the equator.

Sampling schemes that support approximate computation of the SHTs include the `HEALPix` and `IGLOO` schemes. The `HEALPix` [81] is an acronym for Hierarchical Equal Area iso-Latitude Pixelization of a sphere. According to this scheme the surface of a sphere is divided into partitions of equal area known as the pixels. The center of each partition occurs on a discrete number of rings of constant latitude. The `IGLOO` [89] scheme also divides the sphere into pixels of almost equal area. Pixel centers lie on iso-latitude rings which enables fast transform through separation of variables. Both these schemes compute the SHTs approximately. Some of the other approximate schemes include the least-squares based method proposed by Sneeuw [80], which, although requiring L^2 samples, becomes inaccurate and computationally inefficient for large band-limits.

All of the aforementioned sampling schemes require the samples to be taken over the whole sphere. However there are applications where the measurements and samples are available over the spatially-limited region due to practical limitations. For example satellites collecting Earth's data follow an inclined orbit, meaning they cannot take samples near the North and South Pole. This is known as the problem of "polar gap" [94]. In problems related to the measurement of the Earth's gravitational field, we see an unsampled area of about $10°$ co-latitudinal radius [95]. In an effort to fill in the missing measurements, scientists have recently developed methods for collecting the gravity data over the poles using specially equipped aircrafts [96]. However, the polar gap problem remains largely unsolved in other fields of science. For instance, studies related to geomagnetism indicate that it is better to exclude the data sampled closer than $30°$ to either pole because they tend to exhibit higher noise contamination as compared to the data sampled near the equator [65]. In cosmology, the sky is considered an analog to the sphere where observations are made from inside out. Hence, we can see only a limited region of the sky from a particular location on Earth [97]. In addition, large portions of the sky remain unobservable owing to the position of the Sun in the Milky Way galaxy and the surrounding stars, gas and dust [98]. Furthermore, the measurements of the head-related transfer function (HRTF) in acoustics in the South polar region (i.e., closer than $36°$ to the pole) are not considered reliable due to the ground reflections [6, 7].

There exist methods in the literature for the computation of the SHT when the measurements are unavailable or unreliable over the single or double polar cap region. The spherical harmonic basis functions are orthogonal over the sphere. When spatially-limited samples are used for the computation or estimation of the SHT, errors are introduced since the spherical harmonic basis functions no longer remain orthogonal. In other words, the spherical harmonic spectrum suffers from leakage due to the polar gap [99]. In [65], Slepian functions have been used as basis functions for the representation of functions exploiting the orthogonality of Slepian functions over the spatially-limited region. For the accurate computation of the SHT of the HRTF in acoustics, a novel sampling scheme is proposed in [6] that is able to compute sufficiently accurate SHTs over the band-limits of interest without requiring the (unreliable) measurement samples in the South polar cap region.

1.2 Overview and Contribution of Thesis

The focus of this thesis is to revisit existing signal processing theories on the sphere and the ball and develop new techniques which enable the analysis of signals in spatio-spectral domain. Moreover, the problem of developing fast algorithms for the proposed techniques is also addressed.

1.2.1 Questions to be Answered

Following the literature review presented in Section 1.1, we pose the following questions that are answered in this thesis:

Q1. Can we formulate a generalized version of the Slepian concentration problem on the unit sphere?

Q2. Is it possible to generate band-limited Slepian functions on the sphere with maximum energy concentration in one region at the expense of diminishing energy in some other region? How can we use such functions for spectrum estimation to support applications in cosmology, geophysics, etc?

Q3. Can we compute band-limited Slepian functions with non-negative weighting which can be used for robust signal modeling on the sphere?

Q4. Is it possible to combine band-limited and space-limited Slepian functions on the unit ball so that they form a set of new optimal basis functions for signal representation?

Q5. How can we improve the accuracy of the SHT associated with the optimal-dimensionality sampling scheme?

Q6. Can we devise a sampling technique for signal acquisition on the sphere in applications where measurements cannot be taken on the whole sphere?

Q7. Can we design an equiangular sampling scheme that requires fewer samples as compared to the state-of-the-art? In the design and optimization of this scheme how are precision, efficiency (number of samples), and complexity affected?

1.2.2 Thesis Contribution and Organization

The mathematical background is presented in Chapter 2. To answer the research questions posed in the previous section, the first original contribution in this thesis (Chapter 3) is based on finding the differential and weighted Slepian functions on the unit sphere wherein we also propose a set of optimal basis functions for the unit ball. The second part of the thesis (Chapters 4-6) brings about innovation in the existing sampling schemes on the sphere. We present variations of the optimal-dimensionality sampling scheme and the associated SHT algorithm to improve the accuracy of the transform (Chapter 4). We also present a spatially-limited sampling scheme for applications where it is impossible to take samples on the entire sphere (Chapter 5). Lastly, we present a variant of the equiangular sampling scheme in which we show that it is possible to reduce the number of samples if we compromise on some other attribute of the scheme, like complexity or accuracy (Chapter 6).

The summary of the contributions in each chapter is as follows:

Chapter 3 – Slepian Concentration Problems on the Sphere and Ball

In this chapter, we introduce weighting functions in the formulation of the classical Slepian concentration problem on the sphere. We assign different values to the weighting functions in the proposed generalized formulation to present two variants, differential and weighted, of the concentration problem on the sphere for finding band-limited functions with optimal energy concentration in the spatial domain. In the first variant, we consider two spatial regions on the sphere and determine band-limited functions on the sphere such that the difference in the energy concentration of the function over the regions is maximised. Such maximisation enables enhancement of the energy over one region at the cost of it in the other region. In the second variant, we use non-negative weighting as a window function in the formulation of the Slepian problem to optimally concentrate the signal energy in the spatial domain. We formulate each of the problems in the harmonic domain as an eigenvalue problem and review the properties of the eigenfunctions, referred to as Slepian functions, which serve as an alternative basis for the representation of band-limited signals on the sphere. We also demonstrate the use of Slepian functions for localized energy spectrum estimation and robust modeling of the signal on the sphere.

In spherical signal processing we seldom encounter band-limited functions that are only accessible over a specific region in space due to physical restrictions, or space-limited functions that may be spectrally limited due to practical limitations of the measuring equipment. To support these applications, we consider the problem of maximising the product of concentration of energy of signals defined on the ball. The problem of finding optimal basis with maximum energy concentration in spatial and harmonic domains, has already been considered for Euclidean [100] and spherical (unit sphere) [101] domains. In this context, we consider a problem to design optimal basis, with optimal concentration in spatial and spectral domains, for the representation of signals defined on the ball.

Furthermore, we design a set of functions, referred to as optimal basis, which are maximally and simultaneously concentrated in both the spectral and spatial domains. We consider the design of basis functions for a joint subspace, formed by the vector sum of subspace spanned by space-limited spectrally concentrated and band-limited spatially concentrated functions which arise as a solution of Slepian concentration problem on the ball [41]. Using the band-limited and space limited eigenfunctions (obtained as a solution of Slepian concentration problem) in a weighted linear combination, we design optimal bases such that the product of concentration of energy in the spatial and spectral domain is maximised. We further show that the proposed optimal bases serve as complete bases for the representation of a signal in the subspace$-$vector sum of subspaces. We also show that the basis functions are the eigenfunctions of an integral operator that maximises the product of energy concentration of the signal in the spatial and spectral domains.

The results in Chapter 3 have been presented in the following publications which are listed again for ease of reference:

J1. **W. Nafees**, Z. Khalid, and R. A. Kennedy, "Differential and Weighted Slepian Concentration Problems on the Sphere," *IEEE Trans. Signal Process.*, accepted, 2020.

C4. **W. Nafees**, Z. Khalid, and R. A. Kennedy, "Signal analysis on the ball: Design of optimal basis functions with maximal multiplicative concentration in spatial and spectral domains," in *2017 Int. Conf. Systems, Signals and Image Process. (IWSSIP)*, Poznan, Poland, May 2017, pp. 1–5.

Chapter 4 – Improvements in the Optimal Dimensionality Sampling Scheme

One of the tasks in this thesis is to improve the accuracy of the SHT associated with the optimal-dimensionality sampling scheme. We serve this objective by developing a new method for the placement of samples and proposing a variation in the computation of the SHT. We develop a method, referred to as the elimination method, for the placement of iso-latitude rings of samples such that the condition number (ratio of the largest to the smallest eigenvalue value) of the matrices used in the computation of the SHT is minimized. Due to the iterative nature of the resulting SHT algorithm, the error builds-up in the computation of the SHT. To resolve this issue, we also propose a multi-pass SHT algorithm which iteratively reduces the residual between the given signal and the reconstructed signal. We also analyse the changes in the complexity of the SHT with the use of these methods. Through numerical experiments, we demonstrate the improvement in accuracy with the use of the proposed methods.

We also propose an antipodally symmetric sampling scheme of asymptotic optimal dimensionality for the acquisition of band-limited signals. For a signal band-limited at L, the proposed scheme takes $\sim$(asymptotically) L^2 number of samples. We develop the transform associated with the proposed sampling scheme for the accurate computation of the SHT. The SHT developed in this work (having complexity of the order $O(L^4)$) is computationally efficient by a factor of four thanks to the symmetry of placement of samples which is exploited to reduce the size of the matrices required to be inverted for the computation of the SHT. We also propose a method for iterative placement of rings of samples along co-latitude and conduct numerical experiments to analyse the accuracy of the SHT.

The results in Chapter 4 have been presented in the following publications which are listed again for ease of reference:

C3. **W. Nafees**, Z. Khalid, R. A. Kennedy, and J. D. McEwen, "Optimal-dimensionality sampling on the sphere: Improvements and variations," in *Proc. Int. Conf. Sampling Theory and Applications (SampTA)*, Tallin, Estonia, July 2017 pp. 87–91.

C1. **W. Nafees**, Z. Khalid, and R. A. Kennedy, "An Antipodally Symmetric Optimal Dimensionality Sampling on the Sphere," in *Proc. IEEE Int. Conf. Acoust., Speech and Signal Process., ICASSP'2019*, Brighton, UK, April 2019, pp. 5097–5101.

Chapter 5 – Spatially-Limited Sampling of Band-Limited Signals on the Sphere

In this chapter, we devise a sampling scheme for the computation of the SHT when an arbitrary region on the sphere is inaccessible. Since the ellipsoidal region is anisotropic (directional) in nature, we use it to enclose any arbitrary region on the sphere and develop a sampling scheme for the inaccessible ellipsoidal region on the sphere. We propose iso-latitude sampling where we place rings of samples along co-latitude. Based on the parameters of the ellipsoidal region, we rotate the ellipsoidal region to either polar region or equatorial belt region to maximise the surface area available for the placement of iso-latitude rings of samples. We develop the formulation of the SHT for the proposed sampling scheme and present a method for the placement of iso-latitude rings in such a way that ensures accurate computation of the SHT. We also carry out the accuracy analysis of the SHT associated with the proposed sampling scheme and provide an illustration to demonstrate that the proposed scheme enables more accurate computation of the HRTF than the existing schemes.

The results in Chapter 5 have been presented in the following publication which is listed again for ease of reference:

C2. **W. Nafees**, Z. Khalid, and R. A. Kennedy, "Spatially-Limited Sampling of Band-Limited Signals on the Sphere,"in *Proc. IEEE Int. Conf. Acoust., Speech and Signal Process., ICASSP'2018*, Alberta, Canada, April 2018, pp. 4579–4583.

Chapter 6 – Efficient Equiangular Sampling on the Sphere

Lastly, we propose a variant of the equiangular sampling scheme for the computation of spherical harmonic coefficients of band-limited signals on the sphere. The proposed sampling scheme is an exact and efficient method to compute the SHT. We present the harmonic formulation and method of computation of the SHT algorithm associated with the proposed scheme in great detail. The proposed sampling scheme uses fewer number of samples in comparison with the equiangular sampling scheme. Consequently, we obtain favourable outcomes in terms of sampling efficiency, and certain geometrical properties, namely normalized minimum geodesic distance, mesh norm, mesh ratio and Riesz s-energy.

The results in Chapter 6 will be presented in the following manuscript which is listed again for ease of reference:

J2. **W. Nafees**, and Z. Khalid, "Efficient Equiangular Sampling Scheme on the Sphere," *IEEE Signal Process. Letters*, (to be submitted), 2020.

Finally, **Chapter 7** gives a summary of the thesis results and provides an overview of the future research work and manuscripts under progress which are listed here for ease of reference:

J3. **W. Nafees**, Z. Khalid, and J. D. McEwen, "Polar-optimized Equiangular Sampling Scheme on the Sphere," *IEEE Signal Process. Letters*, (to be submitted), 2020.

C5. **W. Nafees**, and Z. Khalid, “Differential and weighted Slepian functions on the Ball,” in *IEEE Int. Conf. Acoust., Speech and Signal Process., ICASSP’2021*, Toronto, Canada, June 2021, (to be submitted).

Chapter 2

Preliminaries

2.1 The Sphere $\mathbb{S}^2$

2.1.1 Signals on the Sphere

Let us first study what a sphere is and how a signal is defined on a spherical manifold. A unit sphere or 2-sphere, denoted by $\mathbb{S}^2$, is defined as

$$\mathbb{S}^2 \triangleq \left\{ \hat{\boldsymbol{u}} \in \mathbb{R}^3 : \|\hat{\boldsymbol{u}}\|_2 = 1 \right\}, \tag{2.1}$$

where $\|\cdot\|_2$ is the Euclidean norm and $\hat{\boldsymbol{u}}$ denotes a vector in 3D Euclidean domain. In the spherical coordinates system, a point on the unit sphere is described using two parameters, namely the co-latitude $\theta \in [0, \pi]$ and longitude $\phi \in [0, 2\pi)$, and mathematically written as $\hat{\boldsymbol{u}} \equiv \hat{\boldsymbol{u}}(\theta, \phi) \triangleq (\sin\theta\cos\phi, \sin\theta\sin\phi, \cos\theta) \in \mathbb{S}^2$, see Fig. 2-1.

We consider complex-valued, square-integrable functions on the unit sphere $\mathbb{S}^2$ denoted by $f(\hat{\boldsymbol{u}}) \equiv f(\theta, \phi)$. These functions form a Hilbert space, denoted by $L^2(\mathbb{S}^2)$, equipped with an inner product given by

$$\langle f_1, f_2 \rangle \triangleq \int_{\mathbb{S}^2} f_1(\theta, \phi)\overline{f_2(\theta, \phi)}\, ds(\theta,\, \phi), \tag{2.2}$$

for any two functions $f_1,\, f_2 \in L^2(\mathbb{S}^2)$. In (2.2), $\overline{(\cdot)}$ denotes the complex conjugate

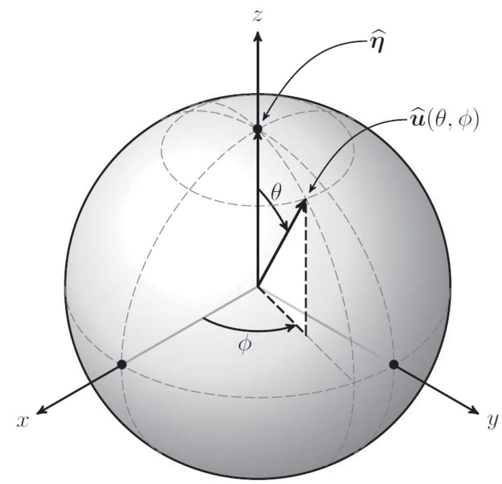

Figure 2-1: Spherical coordinates. (Image courtesy [1])

operation, $ds(\theta,\, \phi) \triangleq \sin\theta d\theta d\phi$ is the differential surface element and $\displaystyle\int_{\mathbb{S}^2} \equiv \int_{\theta=0}^{\pi}\int_{\phi=0}^{2\pi}$ is an integral over the whole sphere. The inner product in (2.2) induces a norm $\|f\| \triangleq \langle f, f\rangle^{1/2}$. We call the functions with finite induced norm (or finite energy), i.e., $\|f\| < \infty$, as "signals on the sphere".

2.1.2 Spherical Harmonic Basis Functions

To study the harmonic content of a signal on the sphere, we can transform the signal to the harmonic domain using the natural bases for the space $L^2(\mathbb{S}^2)$ – spherical harmonic basis functions (or simply spherical harmonics). Spherical harmonics, denoted by $Y_\ell^m(\hat{\boldsymbol{u}}) = Y_\ell^m(\theta, \phi)$ for integer degree $\ell \geq 0$ and integer order $-\ell \leq m \leq \ell$, are defined as

$$Y_\ell^m(\theta, \phi) \triangleq \sqrt{\frac{2\ell+1}{4\pi}\,\frac{(\ell-m)!}{(\ell+m)!}}\,P_\ell^m(\cos\theta)e^{im\phi}, \tag{2.3}$$

where $P_\ell^m(\cdot)$ is the associated Legendre function of degree ℓ and order m [1]. With the adopted definition, the spherical harmonics are orthonormal, i.e.,

$$\langle Y_\ell^m, Y_{\ell'}^{m'}\rangle \triangleq \int_{\mathbb{S}^2} Y_\ell^m(\theta,\phi)\overline{Y_{\ell'}^{m'}(\theta,\phi)}\sin\theta d\theta d\phi = \delta_{\ell\ell'}\delta_{mm'}, \tag{2.4}$$

where $\delta_{\ell\ell'}$ represents the Kronecker delta. The spherical harmonics also have the conjugation property:

$$\overline{Y_\ell^m(\theta,\phi)} = (-1)^m Y_\ell^{-m}(\theta,\phi). \tag{2.5}$$

We also note one of the important property of spherical harmonics, known as spherical harmonics addition theorem [1]

$$\sum_{m=-\ell}^{\ell} Y_\ell^m(\hat{\boldsymbol{u}})\overline{Y_\ell^m(\hat{\boldsymbol{v}})} = \frac{2\ell+1}{4\pi} P_\ell^0(\cos\Delta), \tag{2.6}$$

where $\cos\Delta = \hat{\boldsymbol{u}} \cdot \hat{\boldsymbol{v}}$ is the dot product between two vectors $\hat{\boldsymbol{u}}$ and $\hat{\boldsymbol{v}}$, representing two points on the sphere, and is given as

$$\hat{\boldsymbol{u}} \cdot \hat{\boldsymbol{v}} = \cos\Delta\big(\,(\theta,\phi)\,,(\vartheta,\varphi)\,\big) = \sin\theta\sin\vartheta\cos(\phi-\varphi) + \cos\theta\cos\vartheta. \tag{2.7}$$

2.1.3 Spherical Harmonic Transform

Due to the completeness of the spherical harmonics, any function $f \in L^2(\mathbb{S}^2)$ on the sphere can be expanded in terms of these bases as

$$f(\theta,\phi) = \sum_{\ell=0}^{\infty}\sum_{m=-\ell}^{\ell} (f)_\ell^m Y_\ell^m(\theta,\phi). \tag{2.8}$$

Here $(f)_\ell^m$ denotes the spherical harmonic coefficient of degree $\ell \geq 0$ and order $-\ell \leq m \leq \ell$ and is given by the spherical harmonic transform (SHT) as

$$(f)_\ell^m \triangleq \langle f, Y_\ell^m \rangle = \int_{\mathbb{S}^2} f(\theta,\phi)\overline{Y_\ell^m(\theta,\phi)}\,\sin\theta\, d\theta\, d\phi. \tag{2.9}$$

The synthesis equation, (2.8), to reconstruct the signal from its spherical harmonic coefficients is referred to as inverse SHT, whereas the forward SHT is given by the analysis equation (2.9).

2.1.4 Space-limited and Band-limited Functions

A signal $f \in L^2(\mathbb{S}^2)$ is said to be space-limited within the spatial region $R \subset \mathbb{S}^2$ if it has the form

$$f(\hat{\boldsymbol{u}}) = \begin{cases} f(\hat{\boldsymbol{u}}), & \hat{\boldsymbol{u}} \in R, \\ 0, & \text{otherwise}. \end{cases} \tag{2.10}$$

A signal $f \in L^2(\mathbb{S}^2)$ is said to be band-limited at L if $(f)_\ell^m = 0,\ \forall \ell \geq L$, and can be expanded using the spherical harmonic functions as

$$f(\hat{\boldsymbol{u}}) = \sum_{\ell m=0}^{L-1} (f)_\ell^m Y_\ell^m(\hat{\boldsymbol{u}}), \tag{2.11}$$

where the notation $\sum\limits_{\ell m}^{\infty} \equiv \sum\limits_{\ell=0}^{\infty} \sum\limits_{m=-\ell}^{\ell}$ has been adopted for succinct representation. These band-limited signals form a subspace, denoted by $\mathcal{H}_L$, of dimension L^2. We use the vector notation $\boldsymbol{f}$ to represent a column vector of length L^2 containing the spherical harmonic coefficients such that

$$\boldsymbol{f} \triangleq [\dots (f)_n \dots] = [(f)_0^0, (f)_1^{-1}, (f)_1^0, (f)_1^1, \dots, (f)_{L-1}^{L-1}]^T \in \mathbb{C}^{L^2} \tag{2.12}$$

where the index $n = \ell^2 + \ell + m + 1$ takes the values $n = 1, 2, \dots, L^2$. The spatial and spectral representations of the signal are related through isomorphism [1]

$$\langle f_1, f_2 \rangle = \langle \boldsymbol{f}_1, \boldsymbol{f}_2 \rangle_{\mathbb{C}} \triangleq \boldsymbol{f}_2^H \boldsymbol{f}_1, \tag{2.13}$$

where $(\cdot)^H$ denotes the Hermitian operation.

2.1.5 Rotation on the Sphere

We define the rotation operator $\mathcal{D}(\alpha, \beta, \gamma)$ that rotates a function on the sphere, following the 'zyz' Euler convention, in the sequence of $\gamma \in [0, 2\pi)$ rotation around z-axis, $\beta \in [0, \pi]$ rotation around y-axis and $\alpha \in [0, 2\pi)$ rotation around z-axis. The effect of the rotation operator on the signal $f \in L^2(\mathbb{S}^2)$ can be realized as the inverse rotation of the coordinates, that is,

$$\big(\mathcal{D}(\alpha,\beta,\gamma)f\big)(\hat{\boldsymbol{u}}) = f(\boldsymbol{R}^{-1}\hat{\boldsymbol{u}}) \tag{2.14}$$

where $\boldsymbol{R}$ is the rotation matrix associated with the rotation operator $\mathcal{D}(\alpha,\beta,\gamma)$ [1] and therefore depends on the rotation parameters α,β,γ. We also note that the spherical harmonic coefficients of the original signal f and the rotated signal $\mathcal{D}(\alpha,\beta,\gamma)f$ are related by

$$(\mathcal{D}(\alpha,\beta,\gamma)f)_\ell^m = \sum_{m'=-\ell}^{\ell} D^\ell_{m,m'}(\alpha,\beta,\gamma)(f)_\ell^{m'}, \tag{2.15}$$

where $D^\ell_{m,m'}(\alpha,\beta,\gamma)$ denotes the Wigner-D function [1].

2.1.6 Energy Spectrum

Using Parseval's theorem, we can find the total energy[1] of a function $f \in L^2(\mathbb{S}^2)$ on the sphere in terms of its spherical harmonic coefficients as [4]

$$\|f\|^2 = \int_{\mathbb{S}^2} |f(\hat{\boldsymbol{u}})|^2 ds(\hat{\boldsymbol{u}}) = \sum_{\ell=0}^{\infty} S_{ff}(\ell), \tag{2.16}$$

where S_{ff} is the energy per degree defined as

$$S_{ff}(\ell) = \sum_{m=-\ell}^{\ell} (f)_\ell^m \overline{(f)_\ell^m}. \tag{2.17}$$

The cross-energy spectrum of two functions $f_1, f_2 \in L^2(\mathbb{S}^2)$ is

$$\int_{\mathbb{S}^2} f_1(\hat{\boldsymbol{u}})\overline{f_2(\hat{\boldsymbol{u}})} ds(\hat{\boldsymbol{u}}) = \sum_{\ell=0}^{\infty} S_{f_1 f_2}(\ell)\,, \tag{2.18}$$

where $S_{f_1 f_2}$ is the cross-energy per degree defined as

$$S_{f_1 f_2}(\ell) = \sum_{m=-\ell}^{\ell} (f_1)_\ell^m \overline{(f_2)_\ell^m}. \tag{2.19}$$

[1]The total energy is 4π times the total power for signals on the sphere.

2.2 The Ball $\mathbb{B}^3$

2.2.1 Signals on the Ball

The unit ball, denoted by $\mathbb{B}^3$, is defined as

$$\mathbb{B}^3 \triangleq \mathbb{R}^+ \times \mathbb{S}^2, \tag{2.20}$$

where $\mathbb{R}^+$ denote the domain $[0, \infty)$ on the real line and and $\mathbb{S}^2$ represents the 2-sphere (see Section 2.1.1). We consider complex-valued, square-integrable functions defined on the ball. These functions form a Hilbert space, denoted by $L^2(\mathbb{B}^3)$, equipped with the inner product given by

$$\langle f_1, f_2 \rangle \triangleq \int_{\mathbb{B}^3} f_1(\hat{\boldsymbol{r}})\overline{f_2(\hat{\boldsymbol{r}})}\, dv(\hat{\boldsymbol{r}}), \qquad f_1,\ f_2 \in L^2(\mathbb{B}^3). \tag{2.21}$$

Here $\hat{\boldsymbol{r}} \equiv \hat{\boldsymbol{r}}(r, \theta, \phi) \triangleq (r \sin\theta \cos\phi,\ r\sin\theta\sin\phi,\ r\cos\theta)^T \in \mathbb{R}^3$ represents a vector which parametrizes a point on the ball with $r \in \mathbb{R}^+$, $\theta \in [0, \pi]$ and $\phi \in [0, 2\pi)$ denoting radial distance, co-latitude and longitude, respectively. The integration in (2.21) is carried out over entire $\mathbb{B}^3$ i.e. $\displaystyle\int_{\mathbb{B}^3} \equiv \int_{r=0}^{\infty}\int_{\theta=0}^{\pi}\int_{\phi=0}^{2\pi}$, $dv(\hat{\boldsymbol{r}}) = r^2 \sin\theta\, dr d\theta\, d\phi$ is the differential volume element on $\mathbb{B}^3$ and $\overline{(\cdot)}$ denotes the complex conjugate operation. The inner product given in (2.21) induces a norm $\|f\| \triangleq \langle f, f\rangle^{1/2}$. We refer to the functions with finite induced norm (finite energy) i.e., $\|f\| < \infty$ as "signals on the ball".

Furthermore, for any region $R \subset \mathbb{B}^3$, we define $\langle f_1, f_2\rangle_R \triangleq \displaystyle\int_R f_1(\hat{\boldsymbol{r}})\overline{f_2(\hat{\boldsymbol{r}})}\, dv(\hat{\boldsymbol{r}})$. We also define a linear integral operator $\mathcal{S}$ with kernel $S(\hat{\boldsymbol{r}}, \hat{\boldsymbol{r}}')$ using Fredholm integral equation, that is

$$(\mathcal{S}f)(\hat{\boldsymbol{r}}) = \int_{\mathbb{B}^3} S(\hat{\boldsymbol{r}}, \hat{\boldsymbol{r}}')\, f(\hat{\boldsymbol{r}}') dv(\hat{\boldsymbol{r}}'). \tag{2.22}$$

2.2.2 Fourier-Laguerre Transform and Spectral Representation

For the harmonic representation of signals on the ball, we choose the Fourier-Laguerre basis functions, denoted by $Z_{\ell mp}$ for angular degree $\ell \geq 0$, order $|m| \leq \ell$ and radial integer degree $p \geq 0$ [13, 41], and defined as

$$Z_{\ell mp}(\hat{\boldsymbol{r}}) \triangleq K_p(r)\, Y_\ell^m(\theta, \phi)\,, \quad \hat{\boldsymbol{r}} \equiv \hat{\boldsymbol{r}}(r, \theta, \phi), \tag{2.23}$$

where $Y_\ell^m(\theta, \phi)$ is the spherical harmonic function of degree ℓ and order m and $K_p(r)$ is defined for non-negative integer radial degree p as

$$K_p(r) \triangleq \sqrt{\frac{p!}{(p+2)!}}\, e^{-r/2}\, L_p^{(2)}(r) \tag{2.24}$$

with $L_p^{(2)}$ representing the p-th generalized Laguerre polynomial of second order, defined as

$$L_p^{(2)}(r) \triangleq \sum_{j=0}^{p} \binom{p+2}{p-j} \frac{(-r)^j}{j!}\,. \tag{2.25}$$

Due to the completeness of the Fourier-Laguerre basis functions [13], we can expand any signal $f \in L^2(\mathbb{B}^3)$ as

$$f(\hat{\boldsymbol{r}}) = \sum_{\ell=0}^{\infty} \sum_{m=-\ell}^{\ell} \sum_{p=0}^{\infty} f_{\ell mp} Z_{\ell mp}(\hat{\boldsymbol{r}}), \tag{2.26}$$

where $f_{\ell mp} \triangleq \langle f, Z_{\ell mp} \rangle$ denotes the Fourier-Laguerre coefficient and forms the harmonic domain representation of the signal. A signal f is said to be band-limited in the spectral region $A_{PL} \triangleq \{0 \leq \ell \leq L-1,\, |m| \leq \ell,\, 0 \leq p \leq P-1\}$ if $f_{\ell mp} = 0$, $\forall \ell > L$ and $\forall p > P$. These functions form a PL^2 dimensional space, $\mathcal{H}_{PL}$. In the sequel, we adopt the short-hand notation $\sum\limits_{\ell mp}^{(L,P)} = \sum\limits_{\ell=0}^{L-1} \sum\limits_{m=-\ell}^{\ell} \sum\limits_{p=0}^{P-1}$ for succinct representation.

Part I

The Slepian Concentration Problem

Chapter 3

Slepian Concentration Problems on the Sphere and Ball

This chapter covers the Slepian problem for the sphere and the ball. In the first part, we present a generalized formulation of the Slepian concentration problem on the sphere for finding band-limited functions with an optimal concentration in the spatial domain. By introducing weighting functions in the formulation of classical Slepian concentration problem and assigning different values to these weighting functions, we present two variants of the concentration problem namely the *differential* and the *weighted* Slepian concentration problem. In the differential Slepian concentration problem, we consider two regions on the sphere and find band-limited functions such that the energy is maximised in one region at the expense of the energy in the other region. We note that the differential Slepian problem was first introduced in [51] for one-dimensional (time-domain) signals. We propose non-negative weighting using a spatial window function to formulate and solve the weighted Slepian concentration problem. Each problem can be solved by formulating it in the harmonic domain as an eigenvalue problem, the solution of which yields eigenfunctions that serve as alternative basis functions for the representation of band-limited signals and are referred to as Slepian functions. We also present and analyse the properties of the Slepian functions. To support the applications in acoustics and cosmology, we also provide a demonstration for the use of the proposed Slepian functions for the robust signal modeling and the estimation of the energy spectrum of red and white stochastic processes on the sphere. In the second part of this chapter, we design a set of complete orthonormal optimal basis functions for signals defined on the ball. We design the basis functions by maximising the product of their energy concentration in some spatial region and that in some spectral region. The optimal basis functions are designed as a linear combination of space-limited functions with maximal concentration in the spectral region and band-limited functions with maximal concentration in the spatial region. The proposed optimal basis functions are shown to form a complete set for signal representation in a subspace formed by the vector sum of the subspaces spanned by space-limited and band-limited functions. We also formulate an integral operator which projects the signal to the joint subspace and maximises the product of energy concentrations in harmonic and spatial domains. With the help of some properties of proposed optimal basis functions we show that these functions are the only eigenfunctions of the integral operator.

3.1 Slepian Concentration Problems on the Sphere

The Slepian concentration problem has been formulated and analysed for signals defined on the one-dimensional time domain, the two-dimensional Cartesian plane and the higher dimensions (in the Euclidean setting). In [34] and [41], the Slepian concentration problem has been formulated for signals defined on the unit sphere and the unit ball respectively. In this section, we revisit the Slepian concentration problem for signals on the unit sphere and present a generalized framework and the variations of the concentration problem. We define the generalization of the Slepian concentration problem of finding band-limited function $f \in \mathcal{H}_L$ as

$$\lambda = \max_{f \in \mathcal{H}_L} \left(\frac{\displaystyle\int_{\mathbb{S}^2} h(\hat{\boldsymbol{u}}) |f(\hat{\boldsymbol{u}})|^2 ds(\hat{\boldsymbol{u}})}{\displaystyle\int_{\mathbb{S}^2} g(\hat{\boldsymbol{u}}) |f(\hat{\boldsymbol{u}})|^2 ds(\hat{\boldsymbol{u}})} \right), \tag{3.1}$$

where $h(\hat{\boldsymbol{u}})$ and $g(\hat{\boldsymbol{u}})$ represent the weighting functions and λ is the ratio of the weighted energies of the function. We note that the different choices of the weighting functions $h(\hat{\boldsymbol{u}})$ and $g(\hat{\boldsymbol{u}})$ in (3.1) lead to different variations of the Slepian problem on the sphere. Using (2.11), the spectral domain formulation for (3.1) is given by

$$\lambda = \frac{\sum_{\ell m}^{L-1} (f)_\ell^m \sum_{\ell' m'}^{L-1} H_{\ell\ell'}^{mm'} \overline{(f)_{\ell'}^{m'}}}{\sum_{\ell m}^{L-1} (f)_\ell^m \sum_{\ell' m'}^{L-1} G_{\ell\ell'}^{mm'} \overline{(f)_{\ell'}^{m'}}}, \tag{3.2}$$

where

$$H_{\ell\ell'}^{mm'} \triangleq \int_{\mathbb{S}^2} h(\hat{\boldsymbol{u}}) Y_\ell^m(\hat{\boldsymbol{u}}) \overline{Y_{\ell'}^{m'}(\hat{\boldsymbol{u}})} ds(\hat{\boldsymbol{u}}) \tag{3.3}$$

$$G_{\ell\ell'}^{mm'} \triangleq \int_{\mathbb{S}^2} g(\hat{\boldsymbol{u}}) Y_\ell^m(\hat{\boldsymbol{u}}) \overline{Y_{\ell'}^{m'}(\hat{\boldsymbol{u}})} ds(\hat{\boldsymbol{u}}). \tag{3.4}$$

By defining the coupling matrices $\boldsymbol{H}$ and $\boldsymbol{G}$ with elements $H_{\ell\ell'}^{mm'}$ and $G_{\ell\ell'}^{mm'}$ respectively and adopting the same indexing of these matrices as adopted for indexing the spherical harmonic coefficients in a vector $\boldsymbol{f}$ in (2.12), we can rewrite (3.2) in the matrix form as

$$\lambda = \max_{\boldsymbol{f}} \left(\frac{\boldsymbol{f}^H \boldsymbol{H} \boldsymbol{f}}{\boldsymbol{f}^H \boldsymbol{G} \boldsymbol{f}} \right). \tag{3.5}$$

3.1.1 Classical Slepian Concentration Problem

For the classical Slepian problem on the sphere [23,34], we have the following weighting functions in the spatial domain:

$$h(\hat{\boldsymbol{u}}) = I_R(\hat{\boldsymbol{u}}), \tag{3.6}$$

$$g(\hat{\boldsymbol{u}}) = 1,$$

where $I_R(\hat{\boldsymbol{u}})$ represents the indicator function of the region R defined as

$$I_R(\hat{\boldsymbol{u}}) \triangleq \begin{cases} 1 & \hat{\boldsymbol{u}} \in R, \\ 0 & \hat{\boldsymbol{u}} \in \mathbb{S}^2 \backslash R. \end{cases} \tag{3.7}$$

Here $R \subset \mathbb{S}^2$ represents a region that may be a single connected region or a union of disjoint sub-regions such that $R = R_a \cup R_b \cup \ldots$. The area of the region R is given by $|R| = \displaystyle\int_R ds(\hat{\boldsymbol{u}})$. The solution of the classical Slepian problem yields a family of L^2 eigenfunctions referred to as the classical Slepian functions. These eigenfunctions are mutually orthogonal over the regions R and $\mathbb{S}^2 \backslash R$ and orthonormal over the unit sphere. Due to the optimal localization and the orthogonality of the classical Slepian functions over the region R, these have been used in applications which include, but are not limited to, spectral analysis, signal estimation, signal interpolation and extrapolation and polar gap problem in geodesy and cosmology [34, 64, 65].

3.1.2 Differential Slepian Concentration Problem

Here we present a variation of the Slepian problem by considering two disjoint regions on the sphere. We counter-balance the energy concentration between the two regions such that the energy concentration in one region is enhanced at the expense of diminishing energy concentration in the other. Let R_1 and R_2 be the two regions, such that $R_1 \cap R_2 = \emptyset$, where the energy concentration is required to be maximised and minimised respectively at the same time. For this variant of the Slepian concentration problem, the weighting functions are defined to be

$$\begin{aligned} h(\hat{\boldsymbol{u}}) &= I_{R_1}(\hat{\boldsymbol{u}}) - I_{R_2}(\hat{\boldsymbol{u}}), \\ g(\hat{\boldsymbol{u}}) &= 1, \end{aligned} \tag{3.8}$$

where $I_{R_1}(\hat{\boldsymbol{u}})$ and $I_{R_2}(\hat{\boldsymbol{u}})$ represent the indicator functions for the regions R_1 and R_2 respectively.

By defining the inner product over the region R_k as

$$\langle f_1, f_2 \rangle_{R_k} \triangleq \int_{R_k} f_1(\hat{\boldsymbol{u}}) \overline{f_2(\hat{\boldsymbol{u}})}\, ds(\hat{\boldsymbol{u}}), \tag{3.9}$$

that quantifies the cross-energy spectrum of two functions f_1, f_2 over the region R_k, the numerator in (3.1), for the choice of weighting functions given in (3.8), takes the following form

$$\int_{\mathbb{S}^2} h(\hat{\boldsymbol{u}}) |f(\hat{\boldsymbol{u}})|^2 ds(\hat{\boldsymbol{u}}) = \langle f, f \rangle_{R_1} - \langle f, f \rangle_{R_2}. \tag{3.10}$$

Due to the fact that (3.10) represents the difference of energy of the function over the two regions, we refer to this variant of the concentration problem as the differential Slepian problem. It is trivial to show that the problem in (3.10) reduces to the classical Slepian problem if $R_2 = \emptyset$. Analogous to (3.5), the differential Slepian concentration problem can be written in spectral domain form as the Rayleigh quotient

$$\lambda = \max_{\boldsymbol{f}} \left(\frac{\boldsymbol{f}^H \boldsymbol{H} \boldsymbol{f}}{\boldsymbol{f}^H \boldsymbol{f}} \right), \tag{3.11}$$

where

$$\boldsymbol{H} = {}_1\boldsymbol{D} - {}_2\boldsymbol{D}, \quad \boldsymbol{G} = \boldsymbol{I}, \tag{3.12}$$

$${}_k\boldsymbol{D} = \begin{bmatrix} {}_kD_{00}^{00} & \cdots & {}_kD_{00}^{L-1\,L-1} \\ \cdots & \ddots & \cdots \\ {}_kD_{L-1\,L-1}^{00} & \cdots & {}_kD_{L-1\,L-1}^{L-1\,L-1} \end{bmatrix}, \; k = 1, 2, \tag{3.13}$$

with

$${}_kD_{\ell\ell'}^{mm'} = \int_{R_k} Y_\ell^m(\hat{\boldsymbol{u}}) \overline{Y_{\ell'}^{m'}(\hat{\boldsymbol{u}})} ds(\hat{\boldsymbol{u}}) \qquad k = 1, 2. \tag{3.14}$$

The solution $\boldsymbol{f}$ that maximises λ in (3.11) is also a solution of the eigenvalue problem

$$\boldsymbol{H}\boldsymbol{f} = \lambda \boldsymbol{f}. \tag{3.15}$$

Since $\boldsymbol{H}$ is Hermitian matrix, the solution of the eigenvalue problem, (3.15), yields a set of L^2 real eigenvalues $\{\lambda_\alpha\}$ and L^2 orthogonal eigenvectors $\{\boldsymbol{f}_\alpha\}$ for $\alpha = 1, 2, \ldots, L^2$ which we choose to be orthonormal such that

$$\begin{aligned}\langle \boldsymbol{f}_\alpha, \boldsymbol{f}_\beta \rangle_{\mathbb{C}} &= \delta_{\alpha\beta}, \quad \alpha, \beta = 1, 2, \ldots, L^2, \\ \langle \boldsymbol{f}_\alpha, \boldsymbol{H} \boldsymbol{f}_\beta \rangle_{\mathbb{C}} &= \lambda_\alpha \delta_{\alpha\beta}, \quad \alpha, \beta = 1, 2, \ldots, L^2.\end{aligned} \tag{3.16}$$

The choice of the weighting function $h(\hat{\boldsymbol{u}})$ in (3.8) implies that $|\lambda_\alpha| \leq 1$. We index the eigenvalues and the associated eigenvectors in the non-increasing order such that $1 \geq \lambda_1 \geq \lambda_2 \ldots \lambda_{L^2} \geq -1$. Using (3.3), we express (3.15) as

$$\sum_{\ell' m'}^{L-1} \int_{\mathbb{S}^2} h(\hat{\boldsymbol{u}}) Y_\ell^m(\hat{\boldsymbol{u}}) \overline{Y_{\ell'}^{m'}(\hat{\boldsymbol{u}})} ds(\hat{\boldsymbol{u}}) (f)_{\ell'}^{m'} = \lambda (f)_\ell^m, \tag{3.17}$$

By multiplying (3.17) with $Y_\ell^m(\hat{\boldsymbol{v}})$ followed by the summation over $0 \leq \ell' < L$ and $|m'| \leq \ell'$, we obtain the formulation of an equivalent eigenvalue problem in the spatial domain represented by the Fredholm equation given by

$$\int_{\mathbb{S}^2} D(\hat{\boldsymbol{u}}, \hat{\boldsymbol{v}}) f(\hat{\boldsymbol{v}}) ds(\hat{\boldsymbol{v}}) = \lambda f(\hat{\boldsymbol{u}}), \tag{3.18}$$

where

$$D(\hat{\boldsymbol{u}}, \hat{\boldsymbol{v}}) = \left(\sum_{\ell m}^{L-1} Y_\ell^m(\hat{\boldsymbol{u}}) Y_\ell^m(\hat{\boldsymbol{v}}) \right) \left(I_{R_1}(\hat{\boldsymbol{u}}) - I_{R_2}(\hat{\boldsymbol{u}}) \right). \tag{3.19}$$

Each eigenvector $\boldsymbol{f}_\alpha$ presents the spectral domain representation of the eigenfunction $f_\alpha \in \mathcal{H}_L$. The spatial domain eigenfunction $f_\alpha(\hat{\boldsymbol{u}})$, related to the eigenvector $\boldsymbol{f}_\alpha$ through $\langle f_\alpha, Y_\ell^m \rangle = (f_\alpha)_\ell^m$, for $\alpha = 1, 2, \ldots, L^2$ is referred to as the differential Slepian function. The eigenvalue λ_α quantifies the difference in the energy concentration of the eigenfunction f_α over the regions R_1 and R_2. The differential Slepian function $f_1(\hat{\boldsymbol{u}})$, associated with the largest eigenvalue, is the eigenfunction with maximum energy concentration in the region R_1. Similarly, the differential Slepian function $f_{L^2}(\hat{\boldsymbol{u}})$, associated with the lowest eigenvalue, is the eigenfunction with maximum energy concentration in the region R_2.

3.1.3 Properties of Differential Slepian Functions

Property 1: Orthogonality of the Differential Slepian Functions: The differential Slepian functions are orthonormal over $\mathbb{S}^2$, i.e.,

$$\langle f_\alpha, f_\beta \rangle_{\mathbb{S}^2} = \delta_{\alpha\beta}, \tag{3.20}$$

which simply follows from the orthonormality of the spherical harmonics and (3.16). The differential Slepian functions are orthogonal over the regions R_1 and R_2 such that,

$$\langle f_\alpha, f_\beta \rangle_{R_1} - \langle f_\alpha, f_\beta \rangle_{R_2} = \lambda_\alpha \ \delta_{\alpha\beta}, \tag{3.21}$$

which can be shown using (3.16). Furthermore, the differential Slepian functions are nearly orthogonal over R_1, that is,

$$\begin{aligned} \alpha = \beta : &\qquad \langle f_\alpha, f_\alpha \rangle_{R_1} \geq \lambda_\alpha \\ \alpha \neq \beta : &\quad |\, \langle f_\alpha, f_\beta \rangle_{R_1} | \leq \frac{\sqrt{(1-\lambda_\alpha)(1-\lambda_\beta)}}{2}. \end{aligned} \tag{3.22}$$

Similar results hold true for the region R_2:

$$\begin{aligned} \alpha = \beta : &\qquad \langle f_\alpha, f_\alpha \rangle_{R_2} \geq -\lambda_\alpha \\ \alpha \neq \beta : &\quad |\, \langle f_\alpha, f_\beta \rangle_{R_2} | \leq \frac{\sqrt{(1+\lambda_\alpha)(1+\lambda_\beta)}}{2}. \end{aligned} \tag{3.23}$$

For $\alpha \neq \beta$ the cosine of the angle between any two differential Slepian functions is defined as

$$|\cos \gamma_{f_\alpha, f_\beta}| \triangleq \frac{\langle f_\alpha, f_\beta \rangle}{|f_\alpha|\, |f_\beta|}, \tag{3.24}$$

and can be computed as

$$|\cos\gamma_{f_\alpha,f_\beta}| \leq \frac{1}{2}\frac{\sqrt{(1-\lambda_\alpha)(1-\lambda_\beta)}}{\lambda_\alpha\,\lambda_\beta}, \quad \lambda_\alpha,\lambda_\beta > 0, \tag{3.25}$$

$$|\cos\gamma_{f_\alpha,f_\beta}| \leq \frac{1}{2}\frac{\sqrt{(1+\lambda_\alpha)(1+\lambda_\beta)}}{\lambda_\alpha\,\lambda_\beta} \quad \lambda_\alpha,\lambda_\beta < 0. \tag{3.26}$$

We provide the derivation of these relationships in Appendix A.

Property 2: Completeness of the Differential Slepian Functions: The differential Slepian functions form a complete basis for the space $\mathcal{H}_L$. This follows from the orthonormality of the differential Slepian functions and the dimensionality of $\mathcal{H}_L$.

Property 3: Spectrum of Eigenvalues: Despite the matrix $\boldsymbol{H}$ being indefinite, the eigenvalues are real and lie in $[-1,+1]$ due to the normalization adopted in (3.11). The eigenvalues closer to $+1$ (or -1) represent optimal (maximal) energy concentration in the region R_1 (or R_2). The sum of eigenvalues of the differential Slepian problem is given by

$$\begin{aligned} N_H &= \sum_{\alpha=1}^{L^2}\lambda_\alpha = \mathrm{trace}({}_1\boldsymbol{D}) - \mathrm{trace}({}_2\boldsymbol{D}) \\ &= \sum_{\ell m}^{L}({}_1D_{\ell\ell}^{mm} - {}_2D_{\ell\ell}^{mm}) = \int_{\mathbb{S}^2} D(\hat{\boldsymbol{u}},\hat{\boldsymbol{u}})ds(\hat{\boldsymbol{u}}) \\ &= \int_{\mathbb{S}^2}\sum_{\ell=0}^{L-1}\frac{2\ell+1}{4\pi}P_\ell^0(\hat{\boldsymbol{u}}\cdot\hat{\boldsymbol{u}})\left(I_{R_1}(\hat{\boldsymbol{u}}) - I_{R_2}(\hat{\boldsymbol{u}})\right)ds(\hat{\boldsymbol{u}}) \\ &= \sum_{\ell=0}^{L-1}\frac{2\ell+1}{4\pi}\left(\int_{R_1} ds(\hat{\boldsymbol{u}}) - \int_{R_2} ds(\hat{\boldsymbol{u}})\right) \\ &= \frac{L^2}{4\pi}(|R_1| - |R_2|), \end{aligned} \tag{3.27}$$

where $|R_k|, k=1,2$ represents the area of the k-th region and we have employed the spherical harmonic addition theorem [1]. To find the number of optimally concentrated eigenfunctions in the region R_k, the Shannon number (the sum of the eigenvalues of the classical Slepian problem solved for the k-th region, denoted by N_k) seems to be a good estimate. It is easy to show that $N_H = N_1 - N_2$. For the differential Slepian problem, it can be shown that the difference between the Shannon number, say N_1, obtained when the classical Slepian problem is applied to region R_1 and the sum of positive eigenvalues of the differential problem is equal to the sum of the Shannon number, say N_2, obtained when the classical Slepian problem is applied to region R_2 and the sum of negative eigenvalues of the differential problem. This can be expressed mathematically as

$$N_1 - \sum_{\alpha} \lambda_{\alpha}^{+} = N_2 + \sum_{\alpha} \lambda_{\alpha}^{-}, \tag{3.28}$$

where λ_{α}^{+} and λ_{α}^{-} represent the positive and negative eigenvalues of the differential Slepian problem respectively.

Property 4: Symmetrical Solutions: Since ${}_1\boldsymbol{D} - {}_2\boldsymbol{D} = -({}_2\boldsymbol{D} - {}_1\boldsymbol{D})$, the solution to the original problem in (3.10) holds, with just an inversion in the signs of the eigenvalues λ_α, that is, if we switch the role of R_1 and R_2 as the regions where we require enhanced and diminished energy concentration respectively.

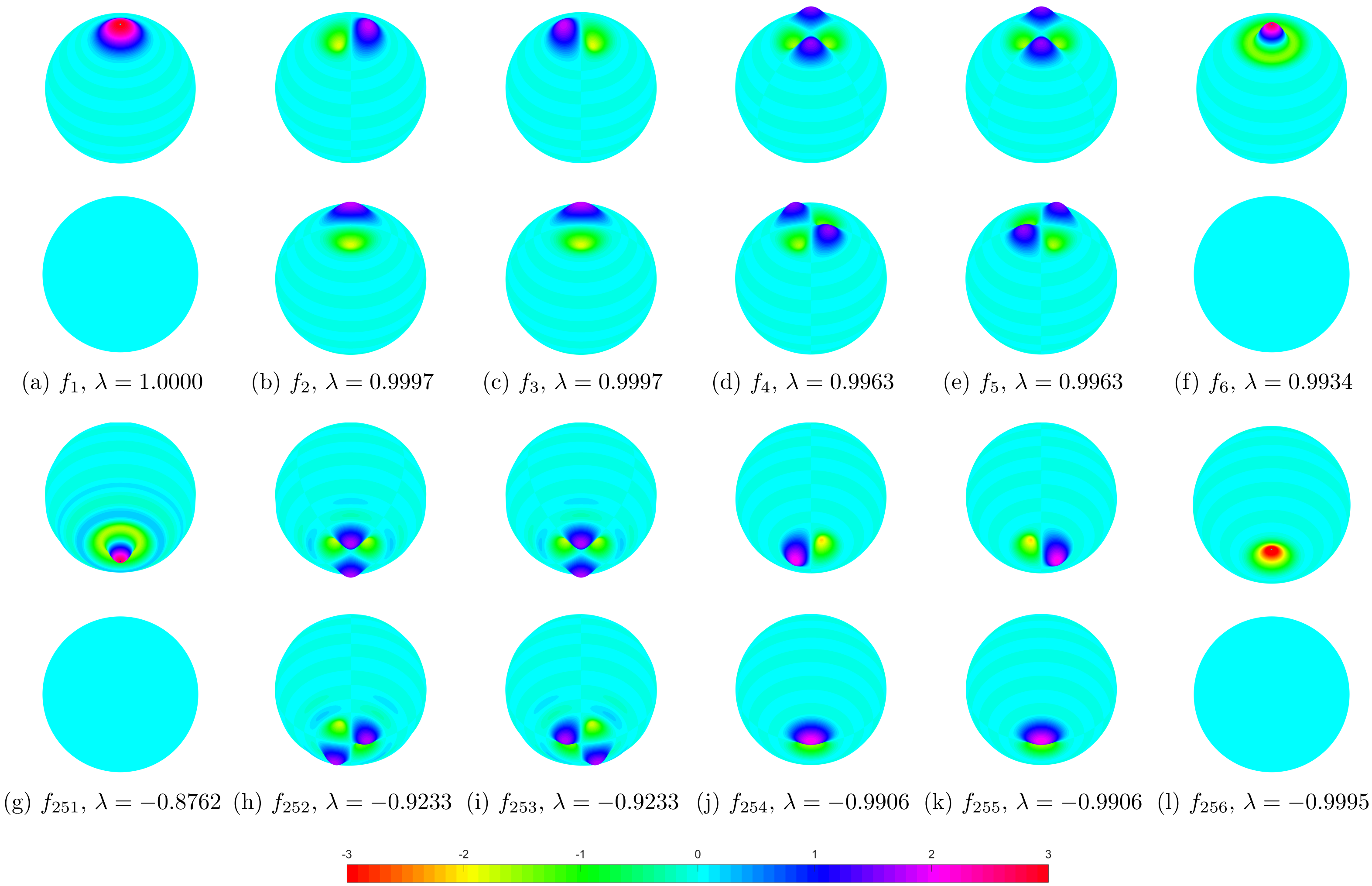

(a) f_1, $\lambda = 1.0000$ (b) f_2, $\lambda = 0.9997$ (c) f_3, $\lambda = 0.9997$ (d) f_4, $\lambda = 0.9963$ (e) f_5, $\lambda = 0.9963$ (f) f_6, $\lambda = 0.9934$

(g) f_{251}, $\lambda = -0.8762$ (h) f_{252}, $\lambda = -0.9233$ (i) f_{253}, $\lambda = -0.9233$ (j) f_{254}, $\lambda = -0.9906$ (k) f_{255}, $\lambda = -0.9906$ (l) f_{256}, $\lambda = -0.9995$

Figure 3-1: Slepian functions in the spatial domain obtained as a solution of differential concentration problem for regions $R_1 = \{\hat{\boldsymbol{u}}(\theta,\phi) \in \mathbb{S}^2 | \, \theta \leq \pi/6\}$, $R_2 = \{\hat{\boldsymbol{u}}(\theta,\phi) \in \mathbb{S}^2 | \, \theta \geq 7\pi/8\}$ and band-limit $L = 16$. For each subplot, the top and bottom plots represent the real and imaginary part of the Slepian function respectively. The first six Slepian functions are optimally concentrated in the region R_1 and are plotted in (a)-(f) with eigenvalues indicated and view set at azimuth of 0 and elevation of $\pi/4$. The last six Slepian functions are optimally concentrated in the region R_2 and are plotted in (g)-(l) with eigenvalues indicated and view set at azimuth of 0 and elevation of $3\pi/4$.

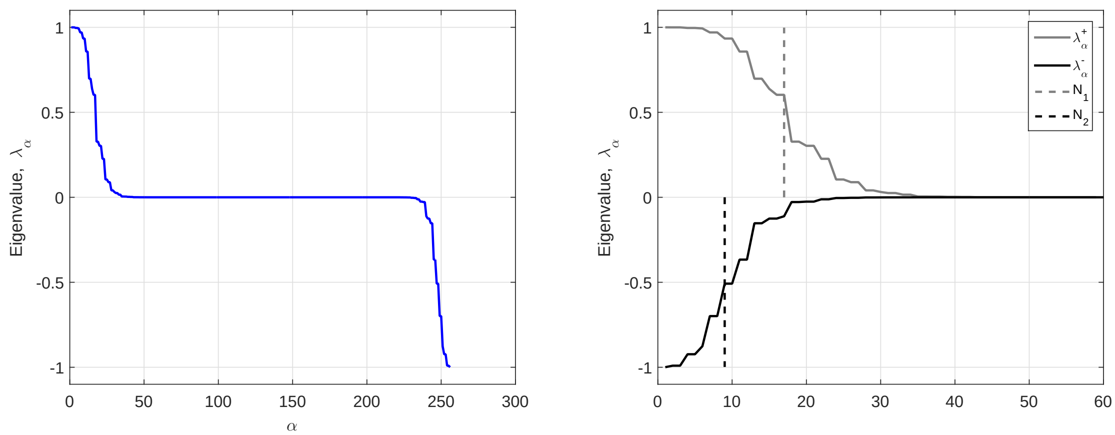

(a) Spectrum of Eigenvalues

(b) Positive and negative eigenvalues spectra

Figure 3-2: Spectrum of eigenvalues obtained when the differential Slepian concentration problem is solved using (3.11) for $L = 16$. (a) The consolidated spectrum of eigenvalues, showing the two transitions associated with the two regions. (b) The positive and negative eigenvalue spectra. The dashed lines show the Shannon numbers $N_1 = 16$ and $N_2 = 9$ respectively for the two regions.

3.1.4 An Illustrative Example

For the differential Slepian concentration problem, we provide an illustration and analyse the eigenfunctions, spectrum of eigenvalues, orthogonality properties and energy enhancement enabled by the eigenfunctions over the regions of interest. We solve the differential concentration problem for R_1 taken as North polar cap of co-latitudinal radius $\theta_1 = \pi/6$, that is, $R_1 = \{\hat{\boldsymbol{u}}(\theta,\phi) \in \mathbb{S}^2 | \, \theta \leq \pi/6\}$, R_2 as South polar cap of co-latitudinal radius $\theta_2 = \pi/8$, that is, $R_2 = \{\hat{\boldsymbol{u}}(\theta,\phi) \in \mathbb{S}^2 | \, \theta \geq 7\pi/8\}$ and band-limit $L = 16$. Fig. 3-1 shows the real and imaginary parts of the first 6 eigenfunctions, $f_1, f_2, \ldots, f_6$ and the last 6 eigenfunctions, $f_{251}, f_{252}, \ldots, f_{256}$, where it is evident that the last 6 eigenfunctions are mostly concentrated in the region R_2 (Property 3).

We also analyse the spectrum of eigenvalues in Fig. 3-2, where the two phase transitions visible in Fig. 3-2 (a) are associated with the two regions. We also plot the positive and negative eigenvalues spectra in Fig. 3-2 (b). The dashed lines show the Shannon number N_1 and N_2 associated with the eigenfunctions obtained from the solution of the classical Slepian problem on regions R_1 and R_2 respectively.

To analyse the mutual orthogonality of the eigenfunctions over the spatial regions of interest, we compute the inner product of the eigenfunctions as well as the bounds on the inner product given in (3.22) and (3.23). The actual inner products are plotted in Fig. 3-3 (a) and (b) that are consistent with the bounds plotted in Fig. 3-3 (c) and (d).

The differential Slepian problem gives eigenfunctions which have increased energy in the region R_1 while the energy in the region R_2 decreases. We compare the energies of the classical Slepian functions constructed for region R_1 and differential Slepian functions and illustrate the reduction of energy in the region R_2 in Fig. 3-4, where E_{class} is the energy of the classical Slepian functions in the region R_2 and the energy E_{diff} refers to the energy of the differential Slepian functions in the region R_2. It can be seen in the figure that E_{diff} is less than E_{class} thus validating the claim made in the prequel.

3.1.5 Rotationally Symmetric Antipodal Regions

The regions R_1 and R_2 associated with the differential Slepian problem can have any arbitrary orientation on the sphere. If the two regions are oriented as shown in Fig. 3-5(a), they are categorized as rotationally symmetric around $\hat{\boldsymbol{v}}_1(\vartheta, \varphi) \in \mathbb{S}^2$ (or $\hat{\boldsymbol{v}}_2(\pi - \vartheta, \pi + \varphi) \in \mathbb{S}^2$) and antipodal regions (since $\hat{\boldsymbol{v}}_1$ is antipodal to $\hat{\boldsymbol{v}}_2$, i.e., $\hat{\boldsymbol{v}}_1 = -\hat{\boldsymbol{v}}_2$).

For the sake of simplification in the computation of the differential Slepian functions, the rotationally symmetric antipodal regions are rotated by $\pi - \varphi$ around z-axis and then by ϑ around y-axis such that the rotated regions $\tilde{R}_1$ and $\tilde{R}_2$ are centered at (rotationally symmetric around) the North ($\hat{\boldsymbol{\eta}}$) and South poles of the unit sphere respectively as shown in Fig. 3-5(b). The regions are now *azimuthally* symmetric antipodal regions and form a special case of rotationally symmetric antipodal regions. Owing to the orientation of the azimuthally symmetric regions, the formulation of the differential Slepian concentration problem is significantly simplified. For the azimuthally symmetric region R_k, the formulation of ${}_kD_{\ell\ell'}^{mm'}$ is simplified by exploiting

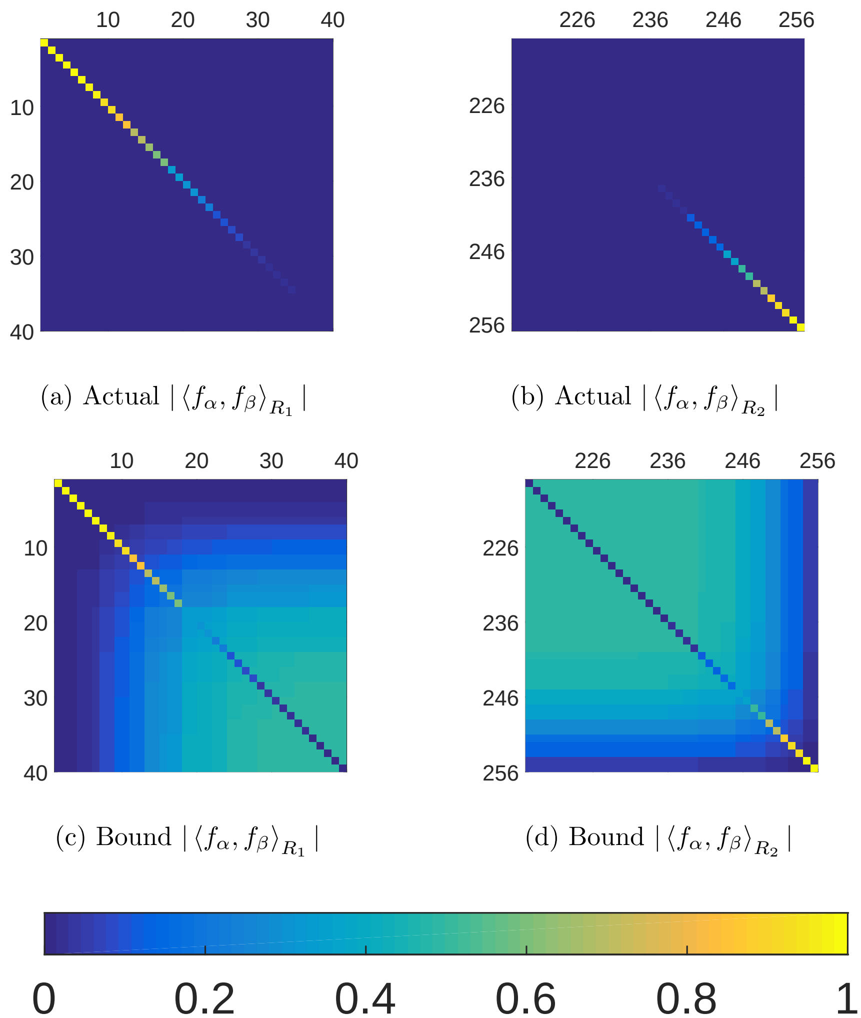

(a) Actual $|\langle f_\alpha, f_\beta\rangle_{R_1}|$

(b) Actual $|\langle f_\alpha, f_\beta\rangle_{R_2}|$

(c) Bound $|\langle f_\alpha, f_\beta\rangle_{R_1}|$

(d) Bound $|\langle f_\alpha, f_\beta\rangle_{R_2}|$

Figure 3-3: Actual inner product of eigenfunctions on region R_1 and R_2 in the top row and their bounds in the bottom row respectively.

the orthogonality of complex exponentials along longitude such that

$$ {}_kD_{\ell\ell'}^{mm'} = 2\pi\delta_{mm'} \underbrace{\int_{\theta_{1k}}^{\theta_{2k}} Y_\ell^m(\theta,0)\overline{Y_{\ell'}^m(\theta,0)}\sin\theta d\theta}_{\triangleq\, {}_kD_{\ell\ell'}^{m}}, \; k=[1,2]. $$

Here $\theta_{11}=0$ and $\theta_{22}=\pi$, whereas θ_{21} and θ_{12} represent the co-latitudinal radii for the rotated regions $\tilde{R}_1$ and $\tilde{R}_2$ respectively. The integral represented by ${}_kD_{\ell\ell'}^m$ can be

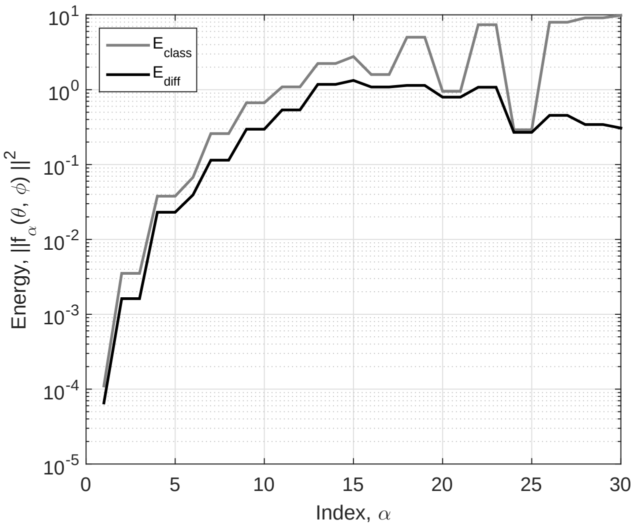

Figure 3-4: E_{class} and E_{diff} represent the energy of the region R_2 calculated using the classical and differential Slepian approach respectively.

evaluated analytically for all $\ell, \ell' \geq m$ as [34, 41]

$$
\begin{aligned}
{}_kD^m_{\ell\ell'} = (-1)^m \frac{\sqrt{(2\ell+1)(2\ell'+1)}}{2} \sum_{q=|\ell-\ell'|}^{|\ell+\ell'|} \begin{pmatrix} \ell & q & \ell' \\ 0 & 0 & 0 \end{pmatrix} \\
\times \begin{pmatrix} \ell & q & \ell' \\ m & 0 & -m \end{pmatrix} \Big(P^0_{q-1}(\cos\theta_{2k}) + P^0_{q+1}(\cos\theta_{1k}) \\
- P^0_{q+1}(\cos\theta_{2k}) - P^0_{q-1}(\cos\theta_{1k}) \Big).
\end{aligned}
\tag{3.29}
$$

Here the arrays of indices are the Wigner-$3j$ symbols [1]. Consequently, the coupling matrix $\boldsymbol{H}$ in (3.15) reduces to a block diagonal matrix of the form: $\boldsymbol{H} = \text{diag}(\boldsymbol{H}_0, \boldsymbol{H}_1, \boldsymbol{H}_1, \ldots, \boldsymbol{H}_L, \boldsymbol{H}_L)$. Here we can see that every submatrix $\boldsymbol{H}_m, m \neq 0$ appears twice because of the doubly degenerate angular order $\pm m$. Therefore, instead of solving the eigenvalue equation (3.15) of size L^2, we only solve a series of $(L-m) \times (L-m)$ harmonic domain eigenvalue problems of the form

$$
\boldsymbol{H}_m \boldsymbol{f}_m = \lambda \boldsymbol{f}_m \tag{3.30}
$$

for each $m = 0, 1, \ldots, L-1$. The submatrix $\boldsymbol{H}_m$ is of the form

$$\boldsymbol{H}_m = \begin{bmatrix} H_{mm} & \ldots & H_{m,L-1} \\ \ldots & \ddots & \ldots \\ H_{L-1,m} & \ldots & H_{L-1,L-1} \end{bmatrix}, \tag{3.31}$$

where every $H_{\ell\ell'} = {}_1D^m_{\ell\ell'} - {}_2D^m_{\ell\ell'}$ and the vector of spherical harmonic coefficients is given as

$$\boldsymbol{f}_m = [f_m, \ldots, f_{L-1}]^T. \tag{3.32}$$

Once we obtain the differential Slepian functions for the azimuthally symmetric antipodal regions, they are rotated back to the original location by applying rotation operator $\mathcal{X}(\vartheta, \varphi)$ on each Slepian function that rotates the signal in a sequence of ϑ around y-axis and φ around z-axis. The spherical harmonic coefficients of the Slepian function f for azimuthally symmetric antipodal regions and the rotated Slepian functions $\mathcal{X}(\vartheta, \varphi)f$ for rotationally symmetric antipodal regions are related by [1]

$$(\mathcal{X}(\vartheta, \varphi)f)^m_\ell = \sum_{m'=-\ell}^{\ell} X^\ell_{m,m'}(\vartheta, \varphi)\,(f)^{m'}_\ell, \tag{3.33}$$

where

$$X^\ell_{m,m'}(\vartheta, \varphi) = e^{-im\vartheta} d^\ell_{m,m'}(\vartheta). \tag{3.34}$$

Here $d^\ell_{m,m'}$ denotes the Wigner-d function of degree ℓ and orders m, m' [1].

3.1.6 Weighted Slepian Concentration Problem on the Sphere

We present the weighted Slepian concentration problem by choosing the weighting function $h(\hat{\boldsymbol{u}})$ to be real, non-negative and bounded by unity, that is,

$$0 \le h(\hat{\boldsymbol{u}}) \le 1, \quad \forall\, \hat{\boldsymbol{u}} \in \mathbb{S}^2, \tag{3.35}$$

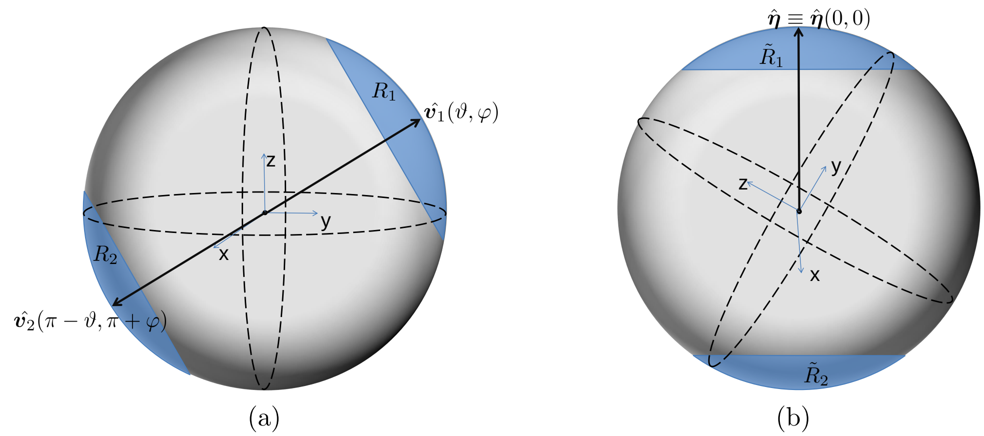

Figure 3-5: The blue part of the sphere shows the regions of interest. (a) Rotationally symmetric antipodal regions R_1 and R_2, (b) Azimuthally symmetric antipodal regions $\tilde{R}_1$ and $\tilde{R}_2$ obtained by rotating the sphere in (a) by $\pi - \varphi$ around z-axis and then by ϑ around y-axis.

and

$$g(\hat{\boldsymbol{u}}) = 1, \quad \forall\, \hat{\boldsymbol{u}} \in \mathbb{S}^2. \tag{3.36}$$

We note that the classical Slepian concentration problem is also a special case of the weighted concentration problem. However the latter is more flexible as the localization of the spatial domain distribution of the energy over some portion of the sphere can be controlled by judiciously choosing the weighting function $h(\hat{\boldsymbol{u}})$. For the choice of the weighting function, the Rayleigh quotient (3.5) is solved by finding eigenvectors of the matrix $\boldsymbol{H}$ with entries given in (3.3). Since $\boldsymbol{H}$ is positive-semi definite and Hermitian by definition, all the eigenvalues of $\boldsymbol{H}$ are real and non-negative and the corresponding eigenvectors can be chosen as orthonormal. The eigenvalue decomposition of $\boldsymbol{H}$ yields L^2 real eigenvectors $\boldsymbol{f}_\alpha$ with corresponding eigenvalue λ_α for $\alpha = 1, 2, \ldots, L^2$, where we index the eigenvalues (or eigenvectors) such that $\lambda_1 \geq \lambda_2 \geq \ldots \geq \lambda_{L^2} \geq 0$. For each eigenvector $\boldsymbol{f}_\alpha$, we obtain the spatial domain eigenfunction $f_\alpha(\hat{\boldsymbol{u}})$ which we refer to as weighted Slepian function. Eigenvalue λ_α serves as a measure of the energy of the weighted signal $\sqrt{h(\hat{\boldsymbol{u}})}f_\alpha(\hat{\boldsymbol{u}})$.

3.1.7 Properties of Weighted Slepian Functions

The weighted Slepian functions exhibit three-fold orthogonality. Firstly, since the eigenvectors are orthonormal, the eigenfunctions are orthonormal in $\mathcal{H}_L$ by isomorphism, that is,

$$\langle \boldsymbol{f}_\alpha, \boldsymbol{f}_\beta \rangle_{\mathbb{C}} = \langle f_\alpha, f_\beta \rangle = \delta_{\alpha\beta}. \tag{3.37}$$

Secondly, since the eigenvectors satisfy

$$\langle \boldsymbol{H}\boldsymbol{f}_\alpha, \boldsymbol{f}_\beta \rangle_{\mathbb{C}} = \boldsymbol{f}_\beta^H \boldsymbol{H}\boldsymbol{f}_\alpha = \lambda_\alpha \langle \boldsymbol{f}_\alpha, \boldsymbol{f}_\beta \rangle_{\mathbb{C}} = \lambda_\alpha \delta_{\alpha\beta}, \tag{3.38}$$

we have, by isomorphism, the following spatial domain orthogonality of the eigenfunctions with respect to a weighted spatial domain inner product

$$\langle f_\alpha, f_\beta \rangle_h \triangleq \int_{\mathbb{S}^2} h(\hat{\boldsymbol{u}}) f_\alpha(\hat{\boldsymbol{u}}) \overline{f_\beta(\hat{\boldsymbol{u}})} ds(\hat{\boldsymbol{u}}) = \lambda_\alpha \delta_{\alpha\beta}. \tag{3.39}$$

Finally, there is a third sense in which the eigenfunctions are orthogonal

$$\langle f_\alpha, f_\beta \rangle_{1-h} = (1 - \lambda_\alpha)\delta_{\alpha\beta}, \tag{3.40}$$

that is, with respect to the complementary weighted inner product. We further note that $\{f_\alpha/\sqrt{\lambda_\alpha}\}$ and $\{f_\alpha/\sqrt{1-\lambda_\alpha}\}$, for $\lambda_\alpha > 0$ are orthonormal with respect to the weighted inner product and complementary weighted inner product respectively.

3.1.8 Application 1: Estimation of Localized Energy Spectrum

The band-limited differential Slepian functions serve as a good choice for localization functions due to their optimal spatial concentration and orthogonality properties. For a global function $p \in L^2(\mathbb{S}^2)$, we obtain its localized version using the differential

Slepian function $f(\hat{\boldsymbol{u}})$ as

$$\Psi(\hat{\boldsymbol{u}}) = f(\hat{\boldsymbol{u}})p(\hat{\boldsymbol{u}})\,. \tag{3.41}$$

Using the background presented in Section 2.1.6, we find the energy spectrum of the localized function $\Psi(\hat{\boldsymbol{u}})$. We assume that the spherical harmonic coefficients of the function p are zero-mean random variables, and the energy spectrum only depends on ℓ (i.e., the function has isotropic energy spectrum). The global energy spectrum is given by

$$\mathbb{E}\left[(p)_\ell^m \overline{(p)_{\ell'}^{m'}}\right] = \frac{S_{pp}(\ell)}{2\ell+1}\,\delta_{\ell\ell'}\delta_{mm'}, \tag{3.42}$$

where $\mathbb{E}[\,\cdot\,]$ is the expectation operator. Let the localized energy spectrum be represented as $S_{\Psi\Psi}$. Using the theoretical framework presented in [4, 64], the relation between S_{pp} and the expected value of $S_{\Psi\Psi}$ is given by

$$\begin{aligned}\mathbb{E}\left[S_{\Psi\Psi}(\ell)\right] &\triangleq \sum_{m=-\ell}^{\ell} \mathbb{E}\left[(\Psi)_\ell^m \overline{(\Psi)_\ell^m}\,\right] \\ &= (2\ell+1)\sum_{q=0}^{L-1} S_{ff}(q) \sum_{r=|\ell-q|}^{\ell+q} S_{pp}(r)\begin{pmatrix} q & r & \ell \\ 0 & 0 & 0\end{pmatrix}^2, \end{aligned} \tag{3.43}$$

where the quantity $\left(\begin{smallmatrix} q & r & \ell \\ 0 & 0 & 0\end{smallmatrix}\right)$ represents the Wigner 3-j symbols [1].

To illustrate the effectiveness of the differential Slepian functions as the localization window functions, we estimate the white and red stochastic processes on the sphere. The energy spectrum of various stochastic processes follows the power law given by

$$S_{pp}(\ell) \sim \ell^{\epsilon}. \tag{3.44}$$

When the energy per angular degree is constant, i.e., for $\epsilon = 0$, the process is called a white process. If $\epsilon = -2$, we may refer to the process as a red process. The definition of these processes may vary from one application to another [64]. For the band-limit $L = 16$, and the regions R_1 and R_2 being taken as North and South polar caps of radii $\pi/6$ and $\pi/8$, the estimate of the energy spectrum for white and red process is plotted in Fig. 3-6 and Fig. 3-7 respectively. The estimates are obtained using the

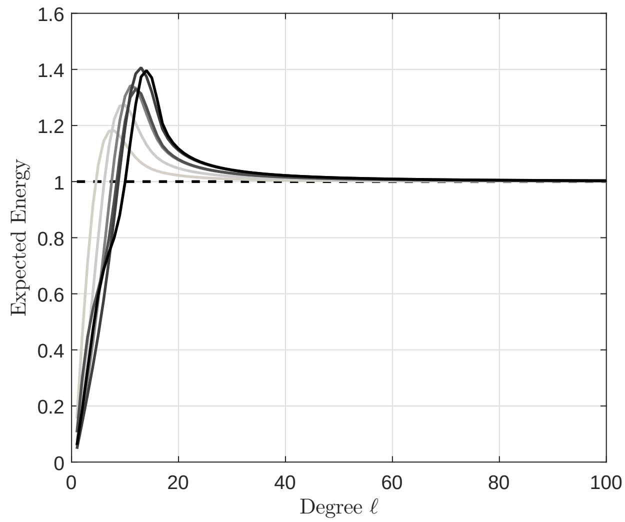

Figure 3-6: Expected localized energy spectral density of a global white process using differential Slepian functions for $L = 16$. The dashed line represents the global white process ($\epsilon = 0$). The expectations of the localized spectra were obtained using the 6 Slepian functions previously shown in Fig. 3-1.

first 6 most concentrated window functions previously plotted in Fig. 3-1. It can be observed that the localized estimates approach the global spectra for both white and red processes. The spectral bias for low degrees $\ell < L$ is simply a consequence of the fact that the localized estimate of the spectrum is a smoothed version of the global spectrum (3.43). Each differential Slepian function $f(\hat{\boldsymbol{u}})$, used in (3.41) for spatial localization, leads to a different estimate. Such single-taper estimates can be combined as a weighted sum to obtain a multi-taper spectral estimate analogous to the one proposed in [4, 33, 58, 64].

3.1.9 Application 2: Robust Signal Modeling

Like the classical Slepian functions, the proposed weighted Slepian functions serve as alternative basis functions for the representation of the band-limited signal. Using the orthonormal weighted Slepian functions $\{f_\alpha(\hat{\boldsymbol{u}})\}$, any bandlimited function $g \in \mathcal{H}_L$

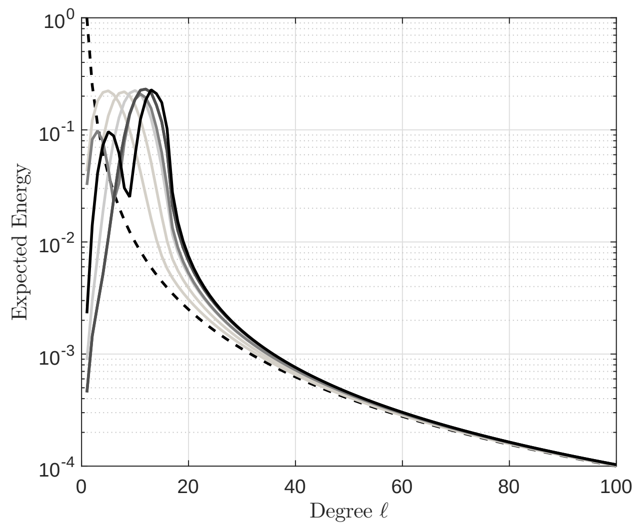

Figure 3-7: Expected localized energy spectral density of a global red process using differential Slepian functions for $L = 16$. The dashed line represents the global red process ($\epsilon = -2$). The expectations of the localized spectra were obtained using the 6 Slepian functions previously shown in Fig. 3-1.

can be expanded as

$$g(\hat{\boldsymbol{u}}) = \sum_{\alpha=1}^{L^2} (g)_\alpha f_\alpha(\hat{\boldsymbol{u}}) = \sum_{\alpha=1}^{L^2} \sqrt{\lambda_\alpha}\, (g)_{h:\alpha} f_\alpha(\hat{\boldsymbol{u}}), \tag{3.45}$$

where

$$(g)_\alpha \triangleq \langle g, f_\alpha \rangle, \quad (g)_{h:\alpha} \triangleq \langle g, f_\alpha / \sqrt{\lambda_\alpha} \rangle_h. \tag{3.46}$$

Therefore, if the band-limited function g is determined from the local information implicit in the weighting function h, we can determine the coefficients of the band-limited function as

$$(g)_\alpha = \frac{1}{\sqrt{\lambda_\alpha}} \langle g, f_\alpha \rangle_h. \tag{3.47}$$

For example with $h(\hat{\boldsymbol{u}}) = I_R(\hat{\boldsymbol{u}})$ (classical problem), the information about the function is available over the region R only. The energy associated with the α-th eigenfunction with respect to the weighted localized inner product is $|(g)_{h:\alpha}|^2$. However, this implies the energy on the sphere is $|(g)_{h:\alpha}|^2/\lambda_\alpha$. Therefore, we may see a significant growth in the energy on the sphere or significant enhancement of noise for small values of λ in the computation of $(g)_\alpha$ using (3.47).

3.2 Slepian Concentration Problem on the Ball

3.2.1 Overview

Here we review the Slepian concentration problem on the ball for finding the band-limited functions with maximum energy concentration in the spatial region or the space-limited functions with maximum energy concentration in the spectral region [23, 33, 34].

In [34], the problem of maximising the concentration of unit energy band-limited function $f \in \mathcal{H}_{PL}$ within the spatial region $R \subset \mathbb{B}^3$ has been presented using a Fredholm integral equation as

$$\left(\mathcal{S}_R \mathcal{S}_{PL} \mathcal{S}_R f\right)(\hat{\boldsymbol{r}}) = \lambda f(\hat{\boldsymbol{r}}), \quad \hat{\boldsymbol{r}} \in \mathbb{B}^3. \tag{3.48}$$

Here $\mathcal{S}_R$ is a spatial selection operator with kernel given by

$$S_R(\hat{\boldsymbol{r}}, \hat{\boldsymbol{r}}') \triangleq I_R(\hat{\boldsymbol{r}})\delta(\hat{\boldsymbol{r}}, \hat{\boldsymbol{r}}'), \tag{3.49}$$

where $I_R(\hat{\boldsymbol{r}}) = 1$ for $\hat{\boldsymbol{r}} \in R \subset \mathbb{B}^3$ and $I_R(\hat{\boldsymbol{r}}) = 0$ for $\hat{\boldsymbol{r}} \in \mathbb{B}^3 \backslash R$ represents the indicator function for the region R and $\delta(\hat{\boldsymbol{r}}, \hat{\boldsymbol{r}'})$ is the Dirac delta function on the ball [41]. $\mathcal{S}_{PL}$ in (3.48) is a spectral selection operator $\mathcal{S}_{PL}$ with kernel given by

$$S_{PL}(\hat{\boldsymbol{r}}, \hat{\boldsymbol{r}'}) \triangleq \sum_{\ell mp}^{(L,P)} Z_{\ell mp}(\hat{\boldsymbol{r}}) \, \overline{Z_{\ell mp}(\hat{\boldsymbol{r}'})}. \tag{3.50}$$

We note that the operators $\mathcal{S}_R$ and $\mathcal{S}_{PL}$ limit the signal within the spatial region R and spectral region A_{PL} respectively.

Using signal expansion in Fourier-Laguerre basis functions, given in (2.26), and the kernel representations in (3.49) and (3.50), the concentration problem in (3.48) can be equivalently formulated as an algebraic eigenvalue problem of size PL^2, given by

$$\sum_{\ell' m' p'}^{(L,P)} f_{\ell' m' p'} \int_R Z_{\ell' m' p'}(\hat{\boldsymbol{r}}) \overline{Z_{\ell m p}(\hat{\boldsymbol{r}})} dv(\hat{\boldsymbol{r}}) = \lambda f_{\ell m p},$$

where $\ell, m, p \in A_{PL}$. Solving this eigenvalue problem we get PL^2 band-limited eigenfunctions. Let f_u denote the eigenfunctions for $u \in [1, PL^2]$. The eigenfunctions are indexed such that $1 > \lambda_1 \geq \lambda_2 \geq \ldots \geq \lambda_{PL^2} > 0$ where λ_u denotes the eigenvalues.

Likewise for unit energy space-limited function $h \in \mathcal{H}_R$, the maximisation of the spectral concentration within the spectral region A_{PL}, is an eigenvalue problem similar to (3.48) and is given by [34]

$$\left(\mathcal{S}_{PL} \mathcal{S}_R \mathcal{S}_{PL} h\right)(\hat{\boldsymbol{r}}) = \lambda h(\hat{\boldsymbol{r}}), \quad \hat{\boldsymbol{r}} \in R. \tag{3.51}$$

Here $\mathcal{H}_R$ represents the space of finite-energy space-limited functions. Since integral equations in (3.48) and (3.51) are same for $\hat{\boldsymbol{r}} \in R$ [34], the band-limited eigenfunctions of (3.48) are similar to the space-limited eigenfunctions of (3.51) in the region R. For each band-limited eigenfunction $f_u \in \mathcal{H}_{PL}$, we have an associated space-limited eigenfunction $h_u = \mathcal{S}_R f_u \in \mathcal{H}_R$, for $u \in [1, PL^2]$. The eigenvalue $0 < \lambda_u < 1$ associated with each function quantifies the energy concentration of the space-limited eigenfunction h_u in the spectral region A_{PL} and the band-limited eigenfunction f_u in the region R, that is,

$$\|f_u\|_R^2 \equiv \langle f_u, f_u \rangle_R \triangleq \langle \mathcal{S}_R f_u, \mathcal{S}_R f_u \rangle = \lambda_u, \tag{3.52}$$

$$\|h_u\|_{PL}^2 \triangleq \langle \mathcal{S}_{PL} h_u, \mathcal{S}_{PL} h_u \rangle = \lambda_u. \tag{3.53}$$

3.2.2 Problem Definition

The set of band-limited eigenfunctions $f_u \in \mathcal{H}_{PL}$, $u \in [1, PL^2]$ forms orthonormal bases, whereas that of space-limited eigenfunctions $h_u \in \mathcal{H}_R$, $u \in [1, PL^2]$ forms orthogonal bases. Let the subspace spanned by these eigenfunctions be $\mathcal{H}_{PL}$ and

$\widetilde{\mathcal{H}}_R \subset \mathcal{H}_R \subset L^2(\mathbb{B}^3)$, respectively (both are finite dimensional.) Therefore, using eigenfunctions we can represent signals more economically, i.e. using less number of basis functions, than using Fourier-Laguerre basis functions, especially if the signal is band-limited and spatially concentrated in some region R, or if it is space-limited and concentrated in some spectral region A_{PL}. Practically, signals may not be entirely limited in spectral domain nor in spatial domain, and representing such signals demands bases (or eigenfunctions) that maximise the concentration of energy in both spectral and spatial domains. In the following, our objective is to develop basis functions which maximise the product of concentration of energy in both spectral and spatial domains. We aim to develop basis functions for the joint subspace $\mathcal{H}_{PL} + \widetilde{\mathcal{H}}_R$, that is, the vector sum of $\mathcal{H}_{PL}$ and $\widetilde{\mathcal{H}}_R$. The basis functions are designed such that the product of concentration of energy in the spectral region A_{PL} and that in the spatial region R is maximised [101].

3.2.3 Design of Optimal Basis Functions

Since the band-limited eigenfunctions f_u, $u \in [1, PL^2]$ and the space-limited eigenfunctions $h_u = \mathcal{S}_R f_u$, $u \in [1, PL^2]$ are designed to have maximal concentration in the spatial region R and the spectral region A_{PL} respectively, we hereby form a new class of functions as a weighted linear combination of these eigenfunctions, as follows:

$$g_u(\hat{\boldsymbol{r}}) \triangleq \alpha_u\, f_u(\hat{\boldsymbol{r}}) + \beta_u\, h_u(\hat{\boldsymbol{r}}), \qquad h_u(\hat{\boldsymbol{r}}) = (\mathcal{S}_R f_u)(\hat{\boldsymbol{r}}), \tag{3.54}$$

for $u \in [1, PL^2]$, where the weights α_u and β_u are optimally chosen to maximise the product of the measures of the energy concentration of the unit energy function g_u in the spectral region A_{PL} and in the spatial region R. Since $f_u \in \mathcal{H}_{PL}$ and $h_u \in \widetilde{\mathcal{H}}_R$, we note that every $g_u \in \mathcal{H}_{PL} + \widetilde{\mathcal{H}}_R$. The space-limited and band-limited eigenfunctions satisfy the following orthogonality relations [101]

$$\begin{aligned} &\|h_u\|_R^2 = \langle h_u, h_v\rangle_R = \langle f_u, h_v\rangle_R = \|f_u\|_R^2 = \delta_{u,v}\lambda_u, \\ &\|h_u\|_{PL}^2 = \lambda_u^2, \qquad \|f_u\|_{PL}^2 = \langle f_u, f_u\rangle = \delta_{u,v} \end{aligned} \tag{3.55}$$

for $u, v \in [1, PL^2]$, where $\delta_{u,v}$ is the Kronecker delta. We determine the weights α_u and β_u in the following theorem.

Theorem 1. *For any unit energy function $g_u \in \mathcal{H}_{PL} + \widetilde{\mathcal{H}}_R$, the product of the energy concentration in the the spectral region A_{PL} and that in the spatial region $R \subset \mathbb{B}^3$ is maximised, when α_u and β_u have the values:*

$$\alpha_{u,1} = X, \quad \beta_{u,1} = \frac{X}{\sqrt{\lambda_u}}, \qquad \alpha_{u,2} = Y, \quad \beta_{u,2} = -\frac{Y}{\sqrt{\lambda_u}}, \tag{3.56}$$

where $X = (2 + 2\sqrt{\lambda_u})^{-1/2}$ and $Y = (2 - 2\sqrt{\lambda_u})^{-1/2}$.

Proof. This problem can be formulated as a constrained maximisation problem given by

$$\text{maximise } \|g_u\|_R^2 \, \|g_u\|_{PL}^2 \text{ subject to } \|g_u\|^2 = 1,$$

with the Lagrangian $\mathcal{L}$ given as

$$\mathcal{L} = \|g_u\|_R^2 \, \|g_u\|_{PL}^2 + \gamma(\|g_u\|^2 - 1).$$

Noting $\|g_u\|_R^2 = \lambda_u(\alpha_u + \beta_u)^2$ and $\|g_u\|_{PL}^2 = (\alpha_u + \beta_u\lambda_u)^2$ yields the two solutions for α_u and β_u given in (3.56).

□

For the two pairs of weights α_u and β_u obtained in Theorem 1, we define a set of functions as

$$g_{u,k}(\hat{\boldsymbol{r}}) = \alpha_{u,k}\, f_u(\hat{\boldsymbol{r}}) + \beta_{u,k}\, (\mathcal{S}_R f_u)(\hat{\boldsymbol{r}}), \tag{3.57}$$

for $u \in [1, PL^2], k = [1, 2]$ with the energy concentration given by,

$$\|g_{u,k}\|_R^2 = \|g_{u,k}\|_{PL}^2 = \frac{1 - (-1)^k \sqrt{\lambda_u}}{2}, \quad k = 1, 2, \tag{3.58}$$

which we obtain by substituting the values for $\alpha_{u,k}$ and $\beta_{u,k}$ in their respective norm functions.

We yet need to check the completeness of the basis functions in (3.57) for the joint subspace $\mathcal{H}_{PL} + \widetilde{\mathcal{H}}_R$. From (3.55) it can be seen that the functions $g_{u,1}$ and $g_{v,2}$ for $u, v \in [1, PL^2]$, $u \neq v$ are orthonormal (unit energy constraint on $g_{u,k}$) for any values of $\alpha_{u,1}$, $\alpha_{v,2}$, $\beta_{u,1}$ and $\beta_{v,2}$. Also from (3.56), it can be easily shown that $g_{u,1}$ and $g_{u,2}$ become orthonormal for each $u \in [1, PL^2]$. The joint subspace has dimension $2PL^2$ (each of the subspaces $\widetilde{\mathcal{H}}_R$ and $\mathcal{H}_{PL}$ is of dimension PL^2), therefore, the $2PL^2$ number of orthonormal functions $g_{u,k} \in \mathcal{H}_{PL} + \widetilde{\mathcal{H}}_R$ for $u \in [1, PL^2]$, and $k = 1, 2$ completely span the joint subspace $\mathcal{H}_{PL} + \widetilde{\mathcal{H}}_R$.

3.2.4 Integral Operator Formulation

We now have a set of functions which form the basis for the subspace $\mathcal{H}_{PL} + \widetilde{\mathcal{H}}_R$. These functions are referred to as optimal basis functions for the ball since they are optimal by design in a sense that the product of measures of the concentration of energy in the spectral region A_{PL} and the spatial region R is maximised. From the set of optimal basis functions, the functions of more significance are the ones that are highly concentrated in the spatial or spectral region of interest. From (3.58), we can see that energy concentration of each $g_{u,k}$ is same in both the spatial and spectral regions. These measures however do not account for the *simultaneous* concentration in the both the spatial and spectral domains. Using the Fredholm integral equation, we develop a linear integral operator which will serve as a measure for the simultaneous energy concentration in the regions of interest in the spatial and spectral domains.

Theorem 2. *The function $w \in L^2(\mathbb{B}^3)$, that maximises the product of concentration of energy in the spectral region A_{PL} and that in the spatial region $R \subset \mathbb{B}^3$, is an* *eigenfunction of an integral operator $\mathcal{S}_M$ with kernel $S_M(\hat{\boldsymbol{r}}, \hat{\boldsymbol{r}'})$ given by*

$$S_M(\hat{\boldsymbol{r}}, \hat{\boldsymbol{r}'}) = \frac{I_R(\hat{\boldsymbol{r}}) + I_R(\hat{\boldsymbol{r}'})}{2} \sum_{\ell mp}^{(L,P)} Z_{\ell mp}(\hat{\boldsymbol{r}}) \, \overline{Z_{\ell mp}(\hat{\boldsymbol{r}'})}, \tag{3.59}$$

and the eigenvalue, denoted by μ, of the eigenfunction w such that $(\mathcal{S}_M w)(\hat{\boldsymbol{r}}) = \mu w(\hat{\boldsymbol{r}})$ is given by

$$\mu = \|w\|_R^2 (2\|w\|_R^2 - 1). \tag{3.60}$$

Proof. We consider $W(\hat{\boldsymbol{r}}) = w(\hat{\boldsymbol{r}}) + \epsilon z(\hat{\boldsymbol{r}})$, where w is a unit energy function, $z \in L^2(\mathbb{B}^3)$ and $\epsilon \in \mathbb{R}$ quantifies the small perturbation in the solution. The energy concentration in the spectral region A_{PL} and the spatial region R is given as $\|w\|_{PL}^2$ and $\|w\|_R^2$ respectively. By applying the variational principle, we find the function w for which the product of concentration of energy in the spatial and spectral region, defined as

$$V = \frac{\|W\|_R^2}{\|W\|^2} \frac{\|W\|_{PL}^2}{\|W\|^2}, \tag{3.61}$$

is maximised. Here the factor $\|W\|^2$ is used to ensure unit energy normalization. As $0 \leq V \leq 1$, we maximize V by maximising $\log V$ as

$$\frac{d}{d\epsilon} (\log V) \Big|_{\epsilon=0} = \frac{d}{d\epsilon} \left(\log \frac{\|W\|_R^2}{\|W\|^2} + \log \frac{\|W\|_{PL}^2}{\|W\|^2} \right) \Big|_{\epsilon=0} = 0.$$

By substituting $\|W\|_R = \langle \mathcal{S}_R W, \mathcal{S}_R W \rangle$ and $\|W\|_{PL} = \langle \mathcal{S}_{PL} W, \mathcal{S}_{PL} W \rangle$, we can simplify the above equation as

$$\begin{aligned} \frac{1}{2\,\|w\|_R^2} \left(\mathcal{S}_R(w\, z) \right)(\hat{\boldsymbol{r}}) + \frac{1}{2\|w\|_L^2} \left(\mathcal{S}_{PL}(w\, z) \right)(\hat{\boldsymbol{r}}) \\ - w(\hat{\boldsymbol{r}}) z(\hat{\boldsymbol{r}}) = 0, \end{aligned}$$

which holds for every $z \in L^2(\mathbb{B}^3)$.

Using the method described in [101] and employing the orthonormality of Fourier-Laguerre basis functions, it can be shown that

$$\begin{aligned}\langle \mathcal{S}_R\mathcal{S}_{PL}w, \mathcal{S}_R w\rangle &= \overline{\langle \mathcal{S}_{PL}\mathcal{S}_R w, \mathcal{S}_{PL} w\rangle}\\ &= \sum_{\ell m p}^{(L,P)} w_{\ell m p}\langle Z_{\ell m p}, w\rangle_R,\end{aligned}$$

and we conclude that

$$\|w\|_R^2 = \|w\|_L^2. \tag{3.62}$$

After rearranging terms we arrive at the result

$$\begin{aligned}&2\,\|w\|_R^2(2\|w\|_R^2-1)\,w(\hat{\boldsymbol{r}}) = \left(\mathcal{S}_{PL}\mathcal{S}_R w + \mathcal{S}_{PL}w\right)(\hat{\boldsymbol{r}}),\ \ \hat{\boldsymbol{r}}\in R,\\ &2\,\|w\|_R^2(2\|w\|_R^2-1)\,w(\hat{\boldsymbol{r}}) = \left(\mathcal{S}_{PL}\mathcal{S}_R w\right)(\hat{\boldsymbol{r}}),\ \ \hat{\boldsymbol{r}}\in \mathbb{B}^3\backslash R.\end{aligned} \tag{3.63}$$

Using the kernels for the operators $\mathcal{S}_R$ and $\mathcal{S}_{PL}$, given in (3.49) and (3.50), respectively, we conclude that $\mathcal{S}_M w(\hat{\boldsymbol{x}}) = \mu\, w(\hat{\boldsymbol{x}})$, where the kernel of the operator $\mathcal{S}_M$ is given in (3.59) and μ given in (3.60). □

Now we show that the basis functions $g_{u,k}$, $u \in [1, PL^2]$, $k = 1, 2$ are the eigenfunctions of the integral operator $\mathcal{S}_M$.

Theorem 3. *Optimal basis functions $g_{u,k}$, given in* (3.57)*, are the only eigenfunctions of the operator $\mathcal{S}_M$.*

Proof. First we show that the optimal basis functions are eigenfunctions of the operator $\mathcal{S}_M$. By substituting function w in (3.63) with any basis function, we obtain $(\mathcal{S}_M g_{u,k})(\hat{\boldsymbol{r}}) = \mu_{u,k} g_{u,k}(\hat{\boldsymbol{r}})$. Here the eigenvalue $\mu_{u,k} = \|g_{u,k}\|_R^2(2\|g_{u,k}\|_R^2 - 1)$ as given in (3.60) is a measure of concentration of energy in the spatial and spectral regions. To show that the optimal basis functions are the only eigenfunctions of the operator, we first note that the operator $\mathcal{S}_M$ is self-adjoint which directly follows from the definition of its kernel $S_M(\hat{\boldsymbol{r}}, \hat{\boldsymbol{r}'})$ given in (3.59). It can also be shown that $\mathcal{S}_M$ is a

Hilbert-Schmidt operator. The self-adjointness and square-integrability together with the fact that zero is not an eigenvalue of the operator $\mathcal{S}_M$ imply that eigenfunctions of the operator form complete basis functions for $\mathcal{H}_{PL} + \widetilde{\mathcal{H}}_R$. This, together with the prior discussion that optimal basis functions are a complete set of basis functions for the subspace $\mathcal{H}_{PL} + \widetilde{\mathcal{H}}_R$, completes the proof of this theorem. $\square$

There are several consequences of Theorem 3. This implies that $\mathcal{S}_M$ is a projection operator which projects a signal $x \in L^2(\mathbb{B}^3)$ to the subspace $\mathcal{H}_{PL} + \widetilde{\mathcal{H}}_R$. Furthermore, it maps any signal in $\mathcal{H}_{PL} + \widetilde{\mathcal{H}}_R$ to a signal in $\mathcal{H}_{PL} + \widetilde{\mathcal{H}}_R$. We review the properties of optimal basis functions in the next section.

3.2.5 Properties of Optimal Basis Functions

Orthogonality of Eigenfunctions: The optimal basis functions $g_{u,k}$ are orthogonal over both $\mathcal{H}_{PL}$ and $\mathcal{H}_R$, i.e.,

$$\langle g_{u,k}, g_{v,k} \rangle_R = \|g_{u,k}\|_R^2 \delta_{u,v}, \quad \langle g_{u,k}, g_{v,k} \rangle_{PL} = \|g_{u,k}\|_{PL}^2 \delta_{u,v}.$$

Spectrum of Eigenvalues: For eigenvalues indexed as $1 > \lambda_u \geq \lambda_v > 0$, we have the following distribution for the product of concentration of energy in the spatial and spectral domains for optimal basis functions for $u < v$ and $u, v \in [1, PL^2]$:

$$\begin{aligned} 1 > &\|g_{u,1}\|_R^2 \|g_{u,1}\|_{PL}^2 \; > \; \|g_{v,1}\|_R^2 \|g_{v,1}\|_{PL}^2 > 0.25, \\ 0.25 > &\|g_{u,2}\|_R^2 \|g_{u,2}\|_{PL}^2 \; > \; \|g_{v,2}\|_R^2 \|g_{v,2}\|_{PL}^2 > 0. \end{aligned}$$

For $k = 1$ the eigenvalue $\mu_{u,k}$ decreases monotonically to 0 as u increases from 1 to PL^2, whereas for $k = 2$ it decreases from a negative value to a minimum and then increases to 0 as u increases from 1 to PL^2.

3.2.6 Signal Representation in Optimal Basis Function

We order the optimal basis functions $g_{u,k}$, $u \in [1, PL^2]$, $k = 1, 2$, as ψ_1, ψ_2, $\ldots$, ψ_{2PL^2}, in decreasing order of eigenvalues' magnitudes. As mentioned before, we can project any signal $x \in L^2(\mathbb{B}^3)$ to the subspace $\mathcal{H}_{PL} + \widetilde{\mathcal{H}}_R$ using the optimal basis functions as

$$x(\hat{\boldsymbol{r}}) = \sum_{u=1}^{2PL^2} \langle x, \psi_u \rangle \, \psi_u(\hat{\boldsymbol{r}}), \tag{3.64}$$

where the inner product is evaluated as

$$\begin{aligned} \langle x, \psi_u \rangle = \sum_{\ell mp}^{(L,P)} x_{\ell mp} (\psi_u)_{\ell mp} = \sum_{\ell mp}^{(L,P)} x_{\ell mp} \times \\ \Big(\alpha_u (f_u)_{\ell mp} + \beta_u \sum_{\ell' m' p'}^{(L,P)} (f_u)_{\ell' m' p'} K_{\ell mp, \ell' m' p'}\Big) \end{aligned} \tag{3.65}$$

and $K_{\ell mp,\ell' m' p'} = \displaystyle\int_R Z_{\ell' m' p'}(\hat{\boldsymbol{r}}) \overline{Z_{\ell mp}(\hat{\boldsymbol{r}})} dv(\hat{\boldsymbol{r}})$ [41]. If the signal x is spatially concentrated in the region R and spectrally concentrated in the region A_{PL}, it is expected that we can represent it using fewer number of terms as the inner product $\langle x, \psi_u \rangle$ decays to 0 as u increases from 1 to $2PL^2$.

Part II

Sampling Schemes on the Sphere

Chapter 4

Improvements in the Optimal Dimensionality Sampling Scheme

In this chapter, we first review the optimal dimensionality sampling scheme on the sphere and the associated spherical harmonic transform and later introduce variations and improvements in this scheme to achieve a transform with higher accuracy. The computation of the SHT associated with the optimal-dimensionality sampling requires the inversion of a series of linear systems in an iterative manner. The stability of the inversion depends on the placement of iso-latitude rings of samples along co-latitude. In this chapter, we have developed a method to place these iso-latitude rings of samples with the objective of improving the well-conditioning of the linear systems involved in the computation of the SHT. We also propose a multi-pass SHT algorithm to iteratively improve the accuracy of the SHT of band-limited signals. Furthermore, we propose an antipodally symmetric sampling scheme of optimal dimensionality for the sampling of band-limited signals. The proposed scheme takes $\sim L^2$ number of samples for the sampling of spherical signal of band-limit L and the accurate computation of its spherical harmonic transform (SHT).

4.1 Optimal Dimensionality Sampling on the Sphere

Recently, an optimal-dimensionality sampling scheme has been proposed in [2] for the accurate computation of the SHT of band-limited signals using only L^2 samples. Optimal-dimensionality sampling has been customized to serve the needs of applications in acoustics [6] and diffusion MRI [25]. Although the SHT associated with this sampling scheme requires the optimal number of samples, it has computational complexity of $O(L^{3.37})$. The computation of the SHT for optimal-dimensionality sampling involves inversion of a series of systems of linear equations. In this scheme, L iso-latitude rings of samples are placed on the sphere at locations (to be explained shortly) given in vector $\boldsymbol{\theta}$, defined as

$$\boldsymbol{\theta} \triangleq [\theta_0\,, \theta_1\,, \ldots, \theta_{L-1}]\,. \tag{4.1}$$

Each successive ring has different number of points in it. For instance, the ring placed at θ_k contains $2k+1$ equiangular points along longitude ϕ.

4.1.1 SHT Formulation

We provide here a brief review of the formulation of the SHT using the optimal dimensionality sampling scheme. For a deeper understanding of the SHT algorithm the reader is directed to the original manuscript [2]. For a signal $f \in \mathcal{H}_L$ we define a vector $\boldsymbol{g}_m$, for every $|m| < L$ as

$$\boldsymbol{g}_m \triangleq \ \left[G_m(\theta_{|m|}), G_m(\theta_{|m|+1}), \ldots, G_m(\theta_{L-1})\right]^T, \tag{4.2}$$

where $G_m(\theta_k)$ for each $\theta_k \in \boldsymbol{\theta}$ is given as

$$G_m(\theta_k) \triangleq \int_0^{2\pi} f(\theta_k, \phi) e^{-im\phi} d\phi = 2\pi \sum_{\ell=m}^{L-1} (f)_\ell^m \tilde{P}_\ell^m(\theta_k). \tag{4.3}$$

Here $\tilde{P}_\ell^m(\theta_k) \triangleq Y_\ell^m(\theta_k, 0)$ denotes scaled associated Legendre functions. The second equality in (4.3) is obtained by using (2.3) and (2.11) and employing the orthogonality of complex exponentials. By defining another vector $\boldsymbol{f}_m$ as

$$\boldsymbol{f}_m = \left[(f)^m_{|m|}, (f)^m_{|m|+1}, \dots, (f)^m_{L-1}\right]^T, \tag{4.4}$$

containing the spherical harmonic coefficients of order m, we formulate a linear system given as

$$\boldsymbol{g}_m = \boldsymbol{P}_m \, \boldsymbol{f}_m, \tag{4.5}$$

where the $\boldsymbol{P}_m$ is an $(L - |m|) \times (L - |m|)$ matrix with elements given by

$$\boldsymbol{P}_m(i, j) = \tilde{P}^m_{|m|+j-1}(\theta_{|m|+i-1}). \tag{4.6}$$

4.2 Optimized Samples Placement and Multi-Pass SHT

The spherical harmonic coefficients for each order $|m| \leq L$ contained in $\boldsymbol{f}_m$ can be recovered by solving the linear system given in (4.5). Computation of the SHT, that is, the computation of spherical harmonic coefficients of the signal $f \in \mathcal{H}_L$ sampled according to the optimal-dimensionality sampling scheme, involves the inversion of a series of linear systems formed by the matrix $\boldsymbol{P}_m$ (defined in (4.6)) for $m = 0, 1, \dots, L-1$ [2]. A condition number minimization method has been proposed in [2] to determine the locations of these iso-latitude rings indexed in (4.1) such that the matrix $\boldsymbol{P}_m$ for each $m = 0, 1, \dots, L-1$ is well-conditioned and the SHT can be accurately computed. With an objective to improve the accuracy of the SHT, we consider the problem of determining the locations of iso-latitude rings of samples which reduce (improve) the condition number (ratio of the largest to the smallest eigenvalue value) of the matrices $\boldsymbol{P}_m,\ m = 0, 1, \dots, L-1$. To further improve the accuracy of the SHT, we also propose a multi-pass SHT algorithm which iteratively reduces the error between the given signal (samples in spatial domain) and the signal synthesized using the computed spherical harmonic coefficients.

4.2.1 Condition Number Minimization

The recovery of $\boldsymbol{f}_m$ for each $|m| < L$ using (4.5) requires inversion of the $\boldsymbol{P}_m$ matrix for each $|m| < L$. For accurate computation of the SHT, it is therefore necessary that the matrix $\boldsymbol{P}_m$ is invertible and well-conditioned. Since $\boldsymbol{P}_m$ is a matrix of associated Legendre polynomials of order m and degrees $|m| \leq \ell < L$ evaluated at θ_i, $i = |m|, |m+1|, \ldots, L-1$, its accurate inversion depends on the locations of the iso-latitude rings indexed in (4.1). To determine the locations of the iso-latitude rings, we propose a condition number minimization technique, herein referred to as the *elimination method*, for the construction of the vector $\boldsymbol{\theta}$.

Let Ω be a set of L equiangular co-latitude angles between 0 and π defined as

$$\Omega \triangleq \left\{ \frac{\pi\,(2t+1)}{2L-1} \right\}, \quad t = 0, 1, \ldots, L-1. \tag{4.7}$$

For $m = 0$, the $\boldsymbol{P}_m$ matrix is formed by inserting all elements of set Ω in (4.6) and has dimension $L \times L$. Since $\boldsymbol{P}_m$, for m=1, requires $L-1$ co-latitude angles, we eliminate one element, say Ω_j, from the set Ω and calculate the condition number, denoted by κ_m, of $\boldsymbol{P}_m$ using all possible $L-1$ combinations of residual elements $\Omega \backslash \Omega_j$. The element Ω_j, whose elimination results in the lowest condition number of $\boldsymbol{P}_m$, is then selected as the first element of the $\boldsymbol{\theta}$ vector. The Ω set is then updated as $\Omega \leftarrow \Omega \backslash \Omega_j$. The same procedure is carried out for the construction of the $\boldsymbol{\theta}$ vector for $m = 2, 3, \ldots, L-1$ which we summarize below in the form of an algorithm.

The $\boldsymbol{\theta}$ vector constructed using the proposed elimination method is optimized in a sense that the it generates $\boldsymbol{P}_m$ matrices of lower condition number as compared to the optimal-dimensionality sampling scheme. This improvement in the condition number comes from the fact that the proposed elimination method has $L-|m|$ choices for θ_m such that the condition number of matrix $\boldsymbol{P}_m$ is minimized. In contrast, the method proposed in [2] has $|m|$ choices for the selection of θ_m and minimization of the condition number of matrix the $\boldsymbol{P}_m$. As an illustration, the condition number

Algorithm 1 Elimination Method

Require: $\boldsymbol{\theta}$ given L

procedure ELIMINATION METHOD

  $\Omega \triangleq \left\{ \frac{\pi\,(2t+1)}{2L-1} \right\}_{t=0,1,\ldots,L-1}$.

  for $m = 0, 1, \ldots, L-1$ **do**

    for $j = 0, 1, \ldots, L-m$ **do**

      $\alpha_j \leftarrow \Omega \backslash \Omega_j$

      evaluate $\boldsymbol{P}_m$ using (4.6) and

      compute condition number κ_m

    end for

    determine index k for minimum value of κ_m

    update $\theta_m \leftarrow \Omega_k$

    update $\Omega \leftarrow \alpha_k$

  end for

  return $\boldsymbol{\theta}$

end procedure

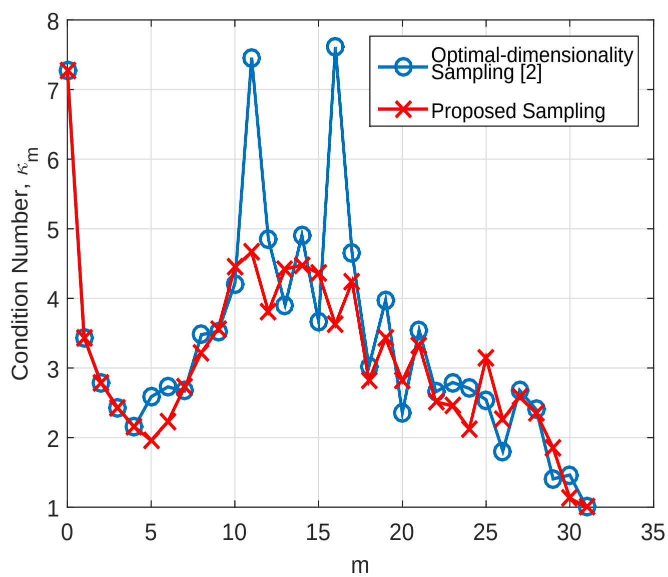

Figure 4-1: The condition number κ_m of the matrix $\boldsymbol{P}_m$, $m = 0, 1, \ldots, L-1$ using the proposed optimized placement of iso-latitude rings and the design proposed in [2] for band-limit $L = 32$.

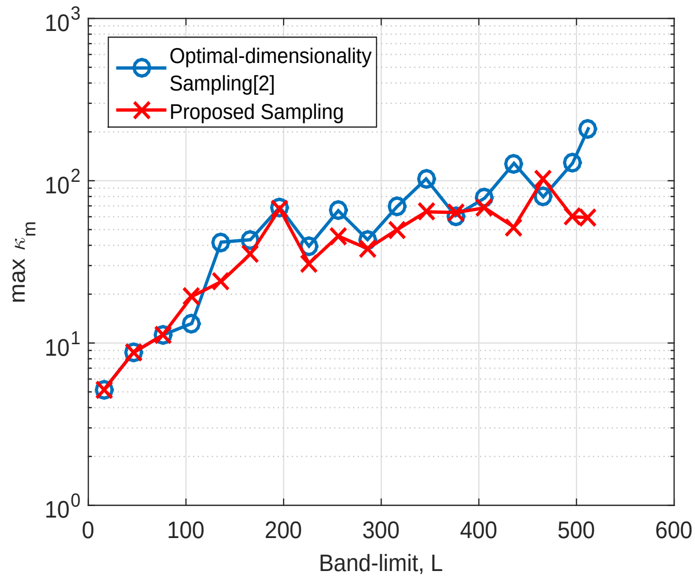

Figure 4-2: The maximum of the condition number $\max(\kappa_m)$, $0 \leq m < L$ for different band-limits $16 \leq L \leq 512$.

κ_m of the matrix $\boldsymbol{P}_m$, $m = 0, 1, \ldots, L-1$ using the proposed optimized placement of iso-latitude rings and the design proposed in [2] is plotted in Fig. 4-1 for band-limit $L = 32$. We also plot the maximum of the condition number κ_m obtained for different band-limits $16 \leq L \leq 512$ in Fig. 4-2. It is evident that the proposed elimination method improves the well-conditioning of the systems involved in the computation of the SHT algorithm associated with the optimal-dimensionality sampling on the sphere.

4.2.2 Multi-pass SHT

In the computation of the SHT of the band-limited signal sampled according to the optimal-dimensionality sampling scheme, the spherical harmonic coefficients are computed iteratively for each order in a sequence $|m| = L-1, L-2, \ldots, 0$. The SHT is inherently iterative in nature as the spherical harmonic coefficients of order $|m|$ are used in the computation of the SHT of order $|m|-1$. Consequently, the error propagates and builds up in the iterative computation of spherical harmonic coefficients. To reduce this error building-up, we propose a multi-pass SHT algorithm which iteratively improves the accuracy of the SHT.

For a signal $f \in \mathcal{H}_L$ sampled by the optimal-dimensionality sampling scheme, the spherical harmonic coefficients can be accurately computed by the algorithm presented in [2][1]. We define the residual (error) between the signal f and the signal synthesized from the recovered spherical harmonic coefficients as

$$r_k(\theta,\phi) = f(\theta,\phi) - \sum_{\ell=0}^{L-1}\sum_{m=-\ell}^{\ell} (\tilde{f}_k)_\ell^m Y_\ell^m(\theta,\phi) \tag{4.8}$$

where $(\tilde{f}_k)_\ell^m$ denotes the spherical harmonic coefficient computed using the proposed SHT algorithm and $k = 1$ (indicating the number of times the transform has been carried out). Once residual is computed, we use the SHT algorithm to compute its spherical harmonic coefficients, denoted by $(\tilde{r_k})_\ell^m$, which we use to update $(\tilde{f}_k)_\ell^m$ as

$$(\widetilde{f_{k+1}})_\ell^m = (\tilde{f}_k)_\ell^m + (\tilde{r_k})_\ell^m. \tag{4.9}$$

We propose to iteratively use (4.8) and (4.9) to compute $(\tilde{f}_k)_\ell^m$ for $k = 1, 2, \ldots$, until the following stopping criterion is not satisfied

$$\max|r_{k+1}(\theta,\phi)| \leq \max|r_k(\theta,\phi)|, \tag{4.10}$$

where max is taken over the samples of the sampling scheme. Since the proposed method requires to compute the SHT multiple times, we refer to the proposed method for the computation of spherical harmonic coefficients as the multi-pass SHT. Later, we illustrate that the proposed method significantly improves the accuracy of the SHT.

[1]SHT can be computed accurately for band-limited signals sampled over optimal-dimensionality sampling scheme [2] using the `MATLAB` based package Novel Spherical Harmonic Transform (NSHT) publicly available at `www.zubairkhalid.org/nsht`.

4.2.3 Computational Complexity Analysis

Here we briefly discuss the computational complexity of the proposed elimination method for the placement of iso-latitude rings and the multi-pass SHT algorithm. The elimination method has the computational complexity of $O(L^5)$. However, it only needs to be run once for the determination of $\boldsymbol{\theta}$ for each L. Furthermore, we note that the complexity of the method presented in [2] for the placement of samples is also $O(L^5)$. For the optimal-dimensionality sampling scheme, the SHT can be computed with complexity of $O(L^{3.37})$. For the proposed multi-pass SHT algorithm, the complexity scales with the number of iterations, denoted by K, needed for the convergence of error. In the next section, we provide examples to illustrate that the proposed multi-pass SHT algorithm converges quickly in $K \ll L$ number of iterations.

4.2.4 Accuracy Analysis

In this section, we analyse the accuracy of the proposed multi-pass SHT algorithm of a band-limited signal evaluated using the optimal-dimensionality sampling scheme with iso-latitude rings placed using the proposed elimination method. We conduct numerical experiments to compare the proposed developments with the SHT proposed in [2]. In our experiment, we first take a band-limited signal $f \in \mathcal{H}_L$ by randomly generating its spherical harmonic coefficients $(f)_\ell^m$ with real and imaginary parts uniformly distributed in $[0, 1]$. We obtain the signal f in the spatial domain, that is, over the samples of the optimal-dimensionality sampling scheme (proposed sampling or [2]) using an inverse SHT. We then apply the SHT presented in [2] and the proposed multi-pass SHT algorithm to recover the spherical harmonic coefficients, denoted by $(\tilde{f})_\ell^m$ and $(\tilde{f}_k)_\ell^m$ respectively. We conduct experiments for 10 different signals to obtain the average value of the maximum error between reconstructed and original spherical harmonic coefficients defined as

$$E_{\max} \triangleq \max |(\tilde{f})_\ell^m - (f)_\ell^m|, \tag{4.11}$$

$$E_{\max}^k \triangleq \max |(\tilde{f}_k)_\ell^m - (f)_\ell^m|, \tag{4.12}$$

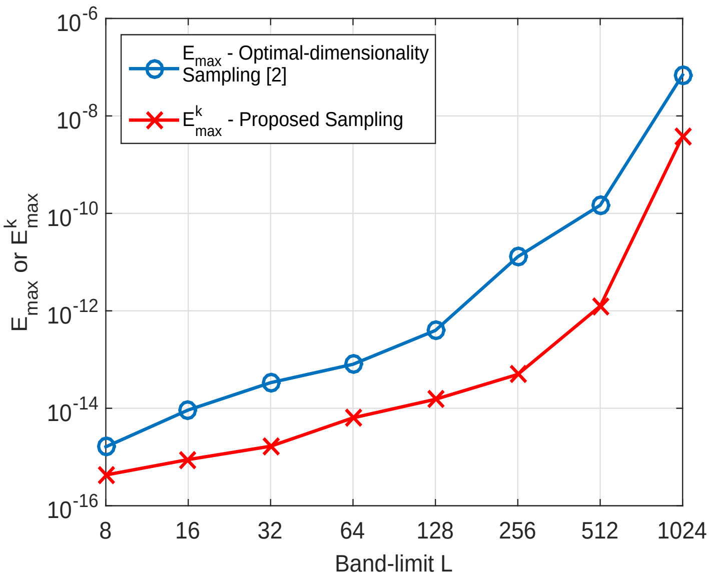

Figure 4-3: Maximum errors $E_{\max}$ and $E^k_{\max}$ between the original and recovered spherical harmonic coefficients using original optimal-dimensionality sampling scheme and the proposed sampling respectively for band-limits $8 \leq L \leq 1024$. Here k depends on the stopping criterion given in (4.10) and is different for each band-limit L.

which we plot for band-limits $8 \leq L \leq 1024$ in Fig. 4-3, where it can be observed that the proposed multi-pass SHT algorithm and optimized placement of samples results in the more accurate computation of the SHT.

We also analyse the convergence of the multi-pass SHT algorithm and the improvement in the accuracy of the SHT enabled by the proposed multi-pass SHT algorithm. We plot the maximum absolute error $E^k_{\max}$ for band-limits $L = 128$ and $L = 256$ in Fig. 4-4, where it can be observed that the proposed multi-pass SHT improves the accuracy of SHT and converges (quickly) in $K \ll L$ number of iterations.

4.3 Antipodally Symmetric Optimal Dimensionality Sampling

Next we propose an antipodally symmetric sampling scheme of asymptotic optimal dimensionality for the acquisition of band-limited signals. For a signal band-limited at L, the proposed scheme takes $\sim L^2$ number of samples. We develop the transform

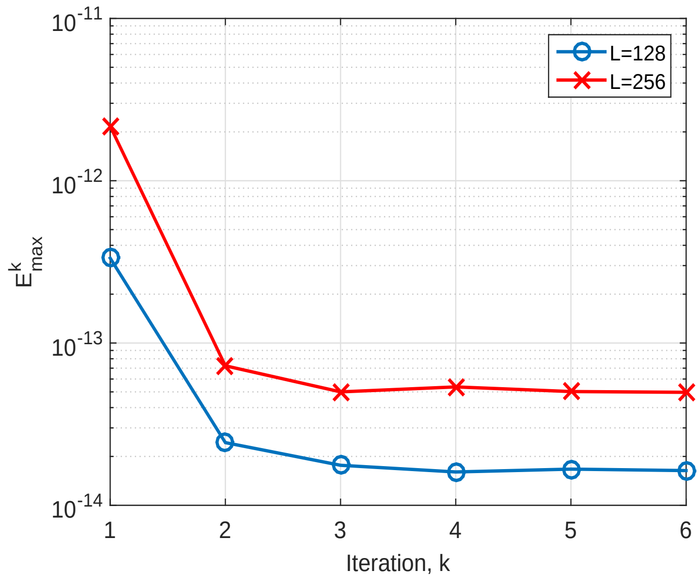

Figure 4-4: Maximum error $E^k_{\max}$, given in (4.12), between the original and recovered spherical harmonic coefficients for band-limits $L = 128$ and $L = 256$ and different iterations of the multi-pass SHT.

associated with the proposed sampling scheme for the accurate computation of the SHT. The SHT developed in this work (having complexity of the order $O(L^4)$) is computationally efficient by a factor of four thanks to the symmetry of placement of samples which is exploited to reduce the size of the matrices required to be inverted for the computation of the SHT.

4.3.1 Proposed Sampling Scheme — Structure and Design

We propose to place $L + 1$ iso-latitude rings (of samples) symmetric around the equator ($\theta = \pi/2$). With this consideration, we define the vector $\boldsymbol{\theta}$ containing the location of these $L + 1$ iso-latitude rings as

$$\boldsymbol{\theta} \triangleq [\theta_0, \pi - \theta_0, \ldots, \theta_{L-3}, \pi - \theta_{L-3}, \theta_{L-1}, \pi - \theta_{L-1}], \tag{4.13}$$

for odd L and

$$\boldsymbol{\theta} \triangleq [\theta_0, \pi - \theta_0, \ldots, \theta_{L-4}, \pi - \theta_{L-4}, \theta_{L-2}, \pi - \theta_{L-2}, \pi/2], \tag{4.14}$$

for even L. Here $\theta_0 = 0$ for both odd and even band-limits and θ_n denotes the n-th entry in the vector $\boldsymbol{\theta}$. We shortly present the location of the remaining rings along the co-latitude. We note that the placement of rings is symmetric around equator. In the iso-latitude ring placed at θ_n, we propose to place the samples along ϕ as

$$\phi_k^n \triangleq \begin{cases} \frac{2k\pi}{2n+1}, & n = 0,\, 2,\, \ldots,\, L-1, \quad k \in [0,\, 2n], \\ \frac{\pi(2k+1)}{2n-1}, & n = 1,\, 3,\, \ldots,\, L, \quad k \in [0,\, 2(n-1)], \end{cases} \tag{4.15}$$

for odd L and

$$\phi_k^n \triangleq \begin{cases} \frac{2k\pi}{2n+1}, & n = 0,\, 2,\, \ldots,\, L-2, \quad k \in [0,\, 2n], \\ \frac{\pi(2k+1)}{2n-1}, & n = 1,\, 3,\, \ldots,\, L-1, \quad k \in [0,\, 2(n-1)], \end{cases} \tag{4.16}$$

including $2L-1$ equiangular samples along ϕ on the ring $\theta_L = \pi/2$ for even L. We use $\mathfrak{E}_L$ and $\mathfrak{O}_L$ to denote the sampling schemes defined above for even and odd L respectively.

Antipodal Symmetry of Sampling Points: We note that the samples along ϕ in the proposed sampling schemes are placed such that the samples in the ring located at θ_n are antipodal to the samples in the ring located at θ_{n-1}, that is, $(\theta_{n-1}, \phi_k^{n-1}) = (\pi - \theta_{n-1}, \pi + \phi_k^n)$ for $n = 2,\, 4,\, \ldots,\, L-1$. As an example, Fig. 4-6 shows the proposed sampling scheme for $L = 21$.

Number of Points: The total number of samples in the proposed sampling schemes is given by

$$2 \sum_{\substack{n=0 \\ n\text{even}}}^{L-1} (2n+1) = L^2 + L, \quad L \ \text{ odd}. \tag{4.17}$$

$$2L - 1 + 2 \sum_{\substack{n=0 \\ n\text{even}}}^{L-2} (2n+1) = L^2 + L - 1, \quad L \text{ even}. \tag{4.18}$$

We note that the proposed sampling schemes for odd and even band-limits take the optimal number of samples asymptotically. Optimal number of samples is L^2 given by the degrees of freedom of the band-limited signal in harmonic space.

4.3.2 Spherical Harmonic Transform

We develop an algorithm for the computation of the spherical harmonic transform of the signal band-limited at L from its samples taken using the proposed sampling scheme. Following the philosophy proposed in [2], we here present the spherical harmonic transform algorithm for the case when the band-limit of the signal is odd. For signals with even band-limits, an equivalent formulation can be developed.

We assume that the samples of the band-limited signal $f \in \mathcal{H}_L$ are taken on the scheme $\mathfrak{O}_L$ proposed in the previous subsection. Exploiting the antipodal structure of the sampling scheme, we first split the band-limited signal f into antipodally symmetric (f_s) and antipodally asymmetric signals f_a given by

$$f_s(\theta_n, \phi_n) = \frac{1}{2}\big(f(\theta_n, \phi_n) + f(\pi - \theta_n, \pi + \phi_n)\big), \tag{4.19}$$

$$f_a(\theta_n, \phi_n) = \frac{1}{2}\big(f(\theta_n, \phi_n) - f(\pi - \theta_n, \pi + \phi_n)\big) \tag{4.20}$$

for all $(\theta_n, \phi_n) \in \mathfrak{O}_L$. It is trivial to show that $f = f_s + f_a$. Due to the antipodal symmetry and asymmetry of the spherical harmonics of even and odd degrees respectively, we have the following expansion of f_s and f_a

$$f_s(\theta_n, \phi_n) = \sum_{\ell=0, \ell\,\mathrm{even}}^{L-1} (f)_\ell^m Y_\ell^m(\theta_n, \phi_n), \tag{4.21}$$

$$f_a(\theta_n, \phi_n) = \sum_{\ell=1, \ell\,\mathrm{odd}}^{L-2} (f)_\ell^m Y_\ell^m(\theta_n, \phi_n). \tag{4.22}$$

The separation of the signal into antipodally symmetric and asymmetric signals en-

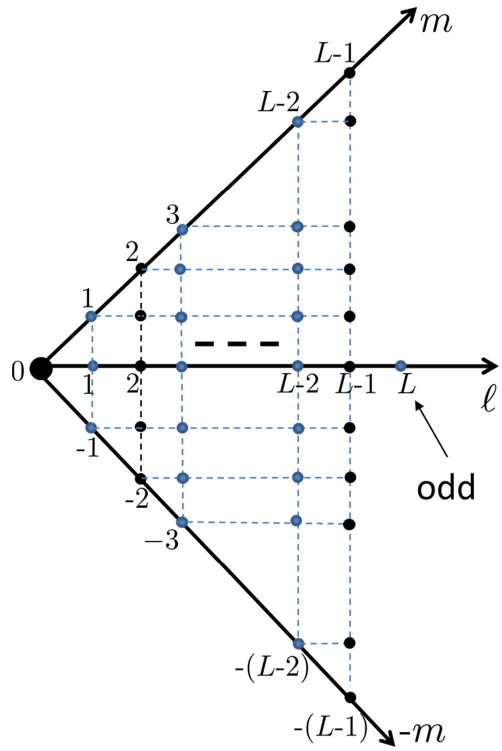

Figure 4-5: Representation of non-zero coefficients of the signal band-limited at odd degree L. The coefficients of the symmetric signal f_s and asymmetric signal f_a are indicated as black and blue dots respectively.

abled by the proposed sampling structure also splits the signal in the harmonic space into even degree harmonics and odd degree harmonics respectively. We illustrate this in Fig. 4-5, where we plot the spectral domain of the band-limited signal and indicate the non-zero coefficients of antipodally symmetric (even degrees, black solid dots) and antipodally asymmetric (odd degrees, blue dots).

4.3.3 Formulation of Spherical Harmonic Transform (SHT)

To formulate the SHT, we first define an iso-latitude transform, that is, the Fourier transform along ϕ for symmetric and asymmetric signals as

$$
\begin{aligned}
{}_sG_m(\theta) &\triangleq \int_0^{2\pi} f_s(\theta,\phi)e^{-im\phi}d\phi && (4.23)\\
&= 2\pi \sum_{\ell=2\lceil |m/2| \rceil, \ell \,\mathrm{even}}^{L-1} (f)_\ell^m \widetilde{Y}_\ell^m(\theta), && (4.24)
\end{aligned}
$$

$$
{}_aG_m(\theta) \triangleq \int_0^{2\pi} f_a(\theta,\phi)e^{-im\phi}d\phi \tag{4.25}
$$

$$
= 2\pi \sum_{\ell=2\lfloor|m/2|\rfloor+1,\ell\,\mathrm{odd}}^{L-2} (f)_\ell^m \widetilde{Y}_\ell^m(\theta), \tag{4.26}
$$

where $\widetilde{Y}_\ell^m(\theta) \triangleq Y_\ell^m(\theta,0)$. We also define vectors ${}_s\mathbf{f}_m$ and ${}_a\mathbf{f}_m$ as

$$
{}_s\mathbf{f}_m = \big[(f)_{2\lceil|m/2|\rceil}^m,\, (f)_{2\lceil|m/2|\rceil+2}^m,\, \ldots,\, (f)_{L-1}^m\big], \tag{4.27}
$$

$$
{}_a\mathbf{f}_m = \big[(f)_{2\lfloor|m/2|\rfloor+1}^m,\, (f)_{2\lfloor|m/2|\rfloor+3}^m,\, \ldots,\, (f)_{L-2}^m\big], \tag{4.28}
$$

containing m-th order spherical harmonic coefficients of even degrees and odd degrees respectively. Be defining

$$
{}_s\mathbf{g}_m = [{}_sG_m(\theta_{2\lceil|m/2|\rceil}),\, {}_sG_m(\theta_{2\lceil|m/2|\rceil+2}),\, \ldots,\, {}_sG_m(\theta_{L-1})],
$$

$$
{}_a\mathbf{g}_m = [{}_aG_m(\theta_{2\lceil|m/2|\rceil}),\, {}_aG_m(\theta_{2\lceil|m/2|\rceil+2}),\, \ldots,\, {}_aG_m(\theta_{L-1})],
$$

for each $|m| < L$, we can express ${}_s\mathbf{g}_m$ using the formulation of ${}_s\mathbf{f}_m$, which respectively contains spherical harmonic coefficients of order $|m| < L$ and even degrees $m \le \ell < L$ and iso-latitude transforms of order $|m| < L$ evaluated along the rings placed at $\theta_{2\lceil|m/2|\rceil}, \theta_{2\lceil|m/2|\rceil+2}, \ldots, \theta_{L-1}$, we can write (4.23) as

$$
{}_s\mathbf{g}_m = 2\pi {}_s\mathbf{P}_L^m \mathbf{f}_m, \quad |m| \le L, \tag{4.29}
$$

where ${}_s\mathbf{P}_L^m$, containing $\widetilde{Y}_\ell^m(\theta_n)$ consistent with the formulation of ${}_sG_m(\theta)$ in (4.23), is a square matrix of number of rows (or columns) equal to $(L-2\lceil|m/2|\rceil+1)/2$. We can similarly express ${}_a\mathbf{g}_m$ as

$$
{}_a\mathbf{g}_m = 2\pi {}_a\mathbf{P}_L^m \mathbf{f}_m, \quad |m| \le L. \tag{4.30}
$$

Using (4.29) and (4.30) for each order $|m| < L$, we can recover the spherical harmonic coefficients of order m and even and odd degrees respectively provided the rings are placed such that ${}_s\mathbf{P}_L^m$ and ${}_a\mathbf{P}_L^m$ are well-conditioned (invertible) and iso-latitude

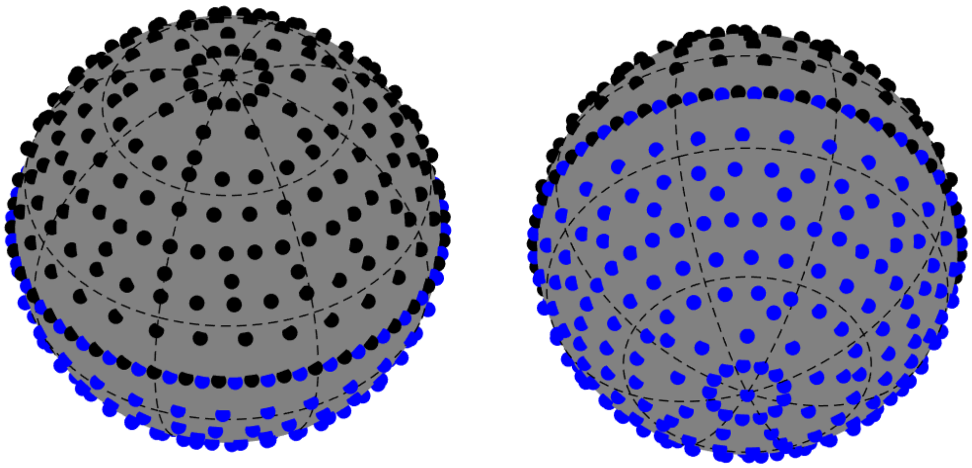

(a) (b)

Figure 4-6: Samples of the proposed sampling schemes are plotted for $L = 21$ with (a) North pole view and (b) South pole view. The points in the Northern hemisphere are are shown in black and the antipodally symmetric points in the Southern hemisphere are shown in blue.

transform along ϕ can be computed accurately. For the structure of the samples along ϕ of the proposed sampling scheme, an iso-latitude transform ${}_sG_m(\theta)$ and ${}_aG_m(\theta)$ can be computed accurately by taking FFT over the samples of symmetric and asymmetric signals respectively.

Remark 1. *We note that the computation of the spherical harmonic coefficients, that is, the spherical harmonic transform using the formulation proposed above requires the inversion of matrices* ${}_s\mathbf{P}_L^m$ *and* ${}_a\mathbf{P}_L^m$ *for each* $|m| < L$*. Therefore the computational complexity of the proposed transform is* $(O(L^4))$ *equal to the complexity of the transform associated with optimal dimensionality sampling without antipodal symmetry [2]. Although we require twice the number of matrices to be inverted, the size of the matrices in our formulation is half the size of matrices required to be inverted for the computation of SHT proposed in [2]. We therefore note the improvement in the SHT computation time by a factor of (approximately) 4 using the proposed scheme.*

4.3.4 Placement of Rings of Samples along Co-latitude

We now present a method to place the rings of samples along co-latitude, that is, we determine positions indexed in (4.13) such that the matrices ${}_s\mathbf{P}_L^m$ and ${}_a\mathbf{P}_L^m$ are well-conditioned. We first note that either ${}_s\mathbf{P}_L^m$ or ${}_a\mathbf{P}_L^{(m-1)}$ depend on $\theta_{2\lceil |m/2| \rceil}, \theta_{2\lceil |m/2| \rceil+2}, \ldots, \theta_{L-1}$ and ${}_s\mathbf{P}_L^{-m} = (-1)^m {}_s\mathbf{P}_L^m$ and ${}_a\mathbf{P}_L^{-m} = (-1)^m {}_a\mathbf{P}_L^m$.

Since the locations of the rings indexed in $\boldsymbol{\theta}$ given in (4.13) appear in pairs due to the antipodal symmetry of the proposed sampling scheme, we are only required to find the locations of the rings in the Northern hemisphere ($\theta \in [0, \pi/2)$). We take a set of equiangular $M > L$ samples in the Northern hemisphere along co-latitude given by

$$\Theta = \left\{ \frac{\pi(t)}{2M} \right\}, \quad t = 0, 1, \ldots, M-1. \tag{4.31}$$

We propose the following method to iteratively place the rings of samples along co-latitude.

- Choose $\theta_{L-1} = \pi(M-1)/2M$, that is the farthest sample from the poles in the set Θ.
- For each $m = L-3,\ L-5,\ \ldots 2$, choose θ_m from the set Θ such that sum of the condition numbers of the four matrices ${}_s\mathbf{P}^m$, ${}_s\mathbf{P}^{m-1}$, ${}_a\mathbf{P}^{m-1}$ and ${}_a\mathbf{P}^{m-2}$ is minimized.
- Choose the last ring location $\theta_0 = 0$.

As an example, we plot the sampling positions on the sphere for $L = 21$ in Fig. 4-6, where we use $M = 15L$ equiangular points in the set Θ. Such placement ensures that the SHT can be accurately computed by taking samples using the proposed sampling scheme and the associated SHT developed in the previous section.

4.3.5 Numerical Accuracy Analysis

We analyse the accuracy of the SHT developed for the proposed sampling scheme in this section. To evaluate the numerical accuracy, we obtain a band-limited test signal

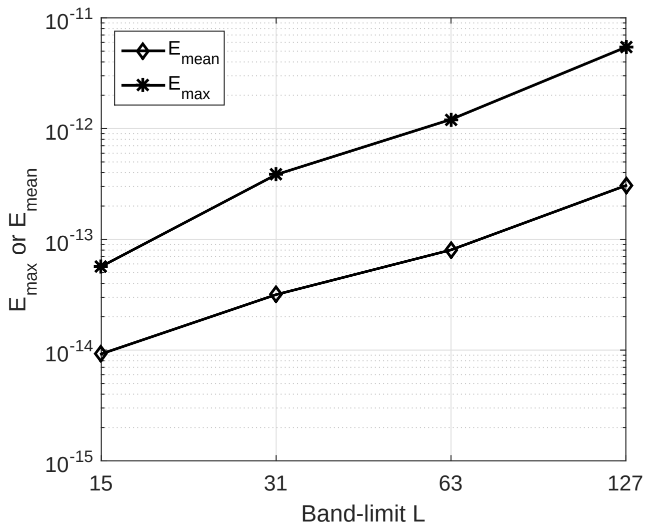

Figure 4-7: Plots of the maximum error E_{max} and the mean error E_{mean}, given in (4.32) and (4.33) respectively, for band-limits $15 \leq L \leq 127$.

f_{t} for band-limit $15 \leq L \leq 127$ in the harmonic domain by generating its spherical harmonic coefficients $(f_{\mathrm{t}})_\ell^m$ for $0 < \ell < L$ with real and imaginary parts uniformly distributed in the interval $[-1, 1]$. We then use (2.8) to obtain the signal at the samples of proposed sampling schemes $\mathfrak{E}_L$ or $\mathfrak{O}_L$. We then apply the proposed SHT to compute the spherical harmonic coefficients, denoted by $(f_{\mathrm{r}})_\ell^m$, of the reconstructed signal. We repeat this test 10 times for each band-limit and compute the average values for the maximum error E_{max} and the mean error E_{mean}, given by

$$E_{\mathrm{max}} \triangleq \max |(f_{\mathrm{t}})_\ell^m - (f_{\mathrm{r}})_\ell^m|, \tag{4.32}$$

$$E_{\mathrm{mean}} \triangleq \frac{1}{L^2} \sum_{\ell=0}^{L-1} \sum_{m=-\ell}^{\ell} |(f_{\mathrm{t}})_\ell^m - (f_{\mathrm{r}})_\ell^m|, \tag{4.33}$$

which are plotted in Fig. 4-7 over the range of band-limits, where it is evident that the proposed transform enables accurate computation of SHT with errors on the order of machine (double) precision.

Chapter 5

Spatially-Limited Sampling of Band-Limited Signals on the Sphere

Spherical signal processing techniques analyse signals in both the spatial and spectral domains. To extract spectral information of a signal, the spherical harmonic transform (SHT) given in (2.9) computes the spherical harmonic coefficients using samples of the signal in spatial domain. Sampling schemes have been proposed which lead to either theoretically exact or accurate computation of the SHT. All of these schemes assume that samples are available on the entire sphere. However, there are applications where samples cannot be taken over some region, for instance, the polar gap problem in geodesy [65], south polar cap region in HRTF measurements [7] and SDSS DR7 quasar binary mask in cosmology [41]. In this chapter, we consider a problem to compute the SHT when some region on the sphere is inaccessible. By enclosing the inaccessible region within an ellipsoidal region, followed by the rotation of the ellipsoidal region either to a polar cap region or the equatorial belt region, we propose spatially-limited iso-latitude sampling on the sphere for the computation of the SHT.

5.1 Regions on the Sphere

We first define different types of regions on the sphere which will be used in the subsequent sections. The (South) *polar cap* region, parameterized by co-latitudinal radius θ_p and denoted by $R_p(\theta_p)$, is defined as

$$R_p(\theta_p) \triangleq \{\hat{\boldsymbol{u}}(\theta, \phi) \in \mathbb{S}^2 | \theta_p \leq \theta \leq \pi, 0 \leq \phi < 2\pi\}, \tag{5.1}$$

with surface area $|R_p(\theta_p)| = \displaystyle\int_{R_p(\theta_p)} ds(\hat{\boldsymbol{u}}) = 2\pi(1 - \cos\theta_p)$, where $ds(\hat{\boldsymbol{u}}) = \sin\theta d\theta d\phi$ represents the differential surface element on $\mathbb{S}^2$.

We also define the *equatorial belt* region of co-latitudinal width $2\theta_e$ as

$$R_e(\theta_e) \triangleq \{(\theta, \phi) | \frac{\pi}{2} - \theta_e \leq \theta \leq \frac{\pi}{2} + \theta_e, 0 \leq \phi < 2\pi\}, \tag{5.2}$$

and note that $|R_e(\theta_e)| = 4\pi \sin\theta_e$. Lastly, we define an *ellipsoidal* region $R_{\mathcal{E}}(\theta_c, a)$ on the sphere, centered at the North pole, given as

$$R_{\mathcal{E}}(\theta_c, a) \triangleq \left\{\hat{\boldsymbol{u}}(\theta, \phi) \in \mathbb{S}^2 \,|\, \Delta\left(\hat{\boldsymbol{u}}\,, \hat{\boldsymbol{v}}_1\right) + \Delta\left(\hat{\boldsymbol{u}}, \hat{\boldsymbol{v}}_2\right) \leq 2a\right\}, \tag{5.3}$$

where $\hat{\boldsymbol{v}}_1 \equiv v_1(\theta_c, 0)$ and $\hat{\boldsymbol{v}}_2 \equiv v_2(\theta_c, \pi)$ represent the two foci, $\Delta(\hat{\boldsymbol{u}}, \hat{\boldsymbol{v}})$ measures the angular distance between two points $\hat{\boldsymbol{u}}, \hat{\boldsymbol{v}} \in \mathbb{S}^2$ [1] and a is the length of the semi-major axis aligned with the x-axis. The semi-minor axis of $R_{\mathcal{E}}(\theta_c, a)$ having length b, such that $\Delta\left(\hat{\boldsymbol{w}}\,, \hat{\boldsymbol{v}}_1\right) + \Delta\left(\hat{\boldsymbol{w}}, \hat{\boldsymbol{v}}_2\right) = 2a$, is aligned with the y-axis and $\hat{\boldsymbol{w}} \equiv w(b, \pi/2)$.

5.2 Sampling Design – Inaccessible Ellipsoidal Region

We first devise a sampling scheme on the sphere when the ellipsoidal region $R'_{\mathcal{E}}(\theta_c, a)$ is inaccessible. We later take into account the arbitrary shaped region by enclosing it with the ellipsoidal region. We propose to take iso-latitude rings of samples of the band-limited signal $f \in \mathcal{H}_L$ on the sphere over the accessible region. For the inaccessible ellipsoidal region $R'_{\mathcal{E}}(\theta_c, a)$, the iso-latitude rings of samples of the signal f can be taken on $\mathbb{S}^2 \backslash R_p(a)$ and therefore the surface area available for sampling is $4\pi - |R_p(a)| = 2\pi(1 + \cos a)$. If we rotate the signal and inaccessible ellipsoidal region by $\pi/2$ along z-axis and then by $\pi/2$ along y-axis, its semi-major and minor axes get aligned with the y-axis and z-axis respectively and the iso-latitude rings of samples of the *rotated* signal $\mathcal{D}(0, \pi/2, \pi/2)f$ can now be taken on $\mathbb{S}^2 \backslash R_e(b)$ of surface area $4\pi(1 - \sin b)$. If $(1 + \cos a) > 2(1 - \sin b)$ for a given inaccessible ellipsoidal region $R'_{\mathcal{E}}(\theta_c, a)$, we rotate the signal prior to sampling such that the major axis of the inaccessible ellipsoidal region is aligned with the y-axis as such judicious choice ensures the availability of larger area for the sampling of the signal. With this consideration, we propose to take L iso-latitude rings of samples at locations such that $\theta_k \in \Theta$ where

$$\Theta = \begin{cases} \theta \in [0, \pi - a] & (1 + \cos a) < 2(1 - \sin b) \\ \theta \in [0, \frac{\pi}{2} - b] \cup [\frac{\pi}{2} + b, \pi] & \text{otherwise.} \end{cases} \tag{5.4}$$

For a ring placed at θ_k, we take $2k+1$ equally spaced points along ϕ. Before we learn the method to determine the ring locations θ_k, $k = 0, 1, \ldots, L-1$ such that the SHT of the band-limited signal can be computed accurately, we reader is advised to review the formulation of the spherical harmonic transform presented in Section 4.1.1.

5.3 Placement of Iso-latitude Rings

The vector $\boldsymbol{f}_m$ containing the SHT coefficients of order m can be recovered by solving a system of linear equations provided $\boldsymbol{P}_m$ is well-conditioned and $\boldsymbol{g}_m$ can be computed correctly. For the proposed sampling scheme, $G_m(\theta_k)$ for $k = |m|, |m+1|, \ldots, L-1$ can be computed correctly by employing FFT as we have taken $2k+1$ samples along ϕ on a ring placed at θ_k [2]. We use the following method to determine the optimal location of L iso-latitude rings, that is $\theta_k, k = 0, 1, \ldots, L-1$, in a spatially limited region ($\theta_k \in \Theta$) such that the matrix $\boldsymbol{P}_m$ given in (4.6) is well-conditioned for each m.

- Consider a set of $N \gg L$ equiangular points taken over Θ.

- Choose the θ_{L-1} from Θ as the point farthest away from the poles ($\theta = 0$ or $\theta = \pi$).

- For $k = L-2, L-3..., 1, 0$, choose θ_k from the remaining elements of Θ for which the condition number of the matrix $\boldsymbol{P}_m$ defined in (4.6) is minimum.

Determining the location of the rings by using the method described above ensures well-conditioning of $\boldsymbol{P}_m$ matrix for every m. Consequently, the spherical harmonic transform can be accurately computed by solving the system given in $\boldsymbol{g}_m = \boldsymbol{P}_m \boldsymbol{f}_m$ for each $|m| = 0, 1 \ldots, L-1$. For the case when the ellipsoidal region and the signal are rotated to align the inaccessible region along equatorial belt region, we recover, through SHT, the coefficients of the rotated signal $\mathcal{D}(0, \pi/2, \pi/2)f$ which we can use in (2.15) to obtain the SHT of the signal f.

Multi-pass SHT

To further improve the accuracy of the computation of the SHT from the samples over the spatially limited region, we use a multi-pass algorithm Section 4.2.2.

5.3.1 Inaccessible Arbitrary Region

We have devised the sampling scheme when ellipsoidal region is inaccessible on the sphere. For the case when an arbitrary shaped region $R \subset \mathbb{S}^2$ is inaccessible, we propose to rotate the signal and the region R such that the region R is enclosed by the ellipsoidal region $R_{\mathcal{E}}(\theta_c, a)$, where we choose rotation parameters and ellipsoidal region parameters which ensure that $R_{\mathcal{E}} \cap R = R$ and $|R_{\mathcal{E}} - R|$ is minimized.

5.4 Accuracy Analysis

We here analyse the numerical accuracy of the proposed spatially-limited sampling scheme on the sphere and the associated multi-pass SHT. In order to analyse the accuracy, we carry out numerical experiments where we obtain a band-limited test signal $f_t \in \mathcal{H}_L$ by randomly generating its spherical harmonic coefficients $(f_t)_\ell^m$ with uniform distribution in the interval $[-1, 1]$ for both the real and imaginary parts and then synthesizing a signal f_t over the proposed sampling scheme when the ellipsoidal region $R_\mathcal{E}(\theta_c, a)$ is inaccessible. We use multi-pass SHT to recover the spherical harmonic coefficients denoted by $(f_r)_\ell^m$ and compute the mean error given by

$$E_{\text{mean}} \triangleq \frac{1}{L^2} \sum_{\ell=0}^{L-1} \left| (f_t)_\ell^m - (f_r)_\ell^m \right|, \tag{5.5}$$

which is averaged over 10 realizations of the experiment and plotted for the band-limit $L = 32$, semi-major axis length $a = 2\pi/10$, $3\pi/20$ and $\pi/10$ and different values of the flattening $0 \leq fl \triangleq \frac{a-b}{a} \leq 1$ of the ellipsoidal region in Fig. 5-1, where it can observed that the rotation of the ellipsoidal region to the equatorial belt region enables accurate reconstruction for the larger values of fl (directional ellipsoidal region). For the smaller values of fl, the reconstruction error is smaller if the ellipsoidal region is not rotated which is due to the fact that the surface area for sampling is larger when the ellipsoidal region of smaller fl is enclosed by the polar cap region than the equatorial belt region. We also extend our analysis and plot the mean error E_{mean} in Fig. 5-2 for different band-limits $8 \leq L \leq 64$, semi-major axis length $a = \pi/10$ and two values of flattening $fl = 0.5$ (when the ellipsoidal region remains at the North pole) and $fl = 0.95$ (when the ellipsoidal region is rotated to the equatorial belt). Accuracy analysis reveals that the proposed sampling design on the sphere enables accurate computation of the SHT when the samples of the band-limited signal are inaccessible over some region on the sphere. For a given inaccessible region $R \subset \mathbb{S}^2$, we note that the bounds on the reconstruction error can be obtained by taking into account the surface area $4\pi - |R|$ available for sampling and the signal band-limit L. However, it is the subject of future work.

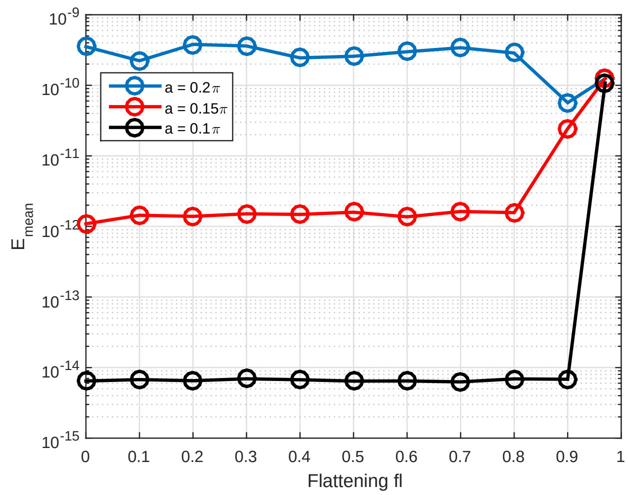

Figure 5-1: Mean error observed when flattening varies in the range $0 \leq fl < 1$ for a constant band-limit $L = 32$ and semi-major axis $a = 0.2\pi$, 0.15π and 0.1π.

5.5 Illustration

Here we use the proposed sampling scheme and the associated multi-pass SHT algorithm for the computation of the SHT of the signal obtained from the analytical HRTF model [102]. The following parameters are used in the model to obtain the HRTF signal f: head radius $a = 0.09$ m, distance from the center of the sphere to the source $r = 1$ m, sound frequency $f_s = 15$ kHz and speed of sound $c = 340$ m/s. Since the HRTF measurements are unreliable at the South polar region, we design the sampling scheme for the region $R = \{(\theta, \phi) | 0 \leq \theta \leq 8\pi/10, 0 \leq \phi < 2\pi\}$ for band-limit $L = 38$. We then use multi-pass SHT algorithm to obtain the reconstructed signal $\hat{f}$. We plot the absolute value of the signal $|f|$, sampling points of the proposed scheme over the accessible region, samples of the signal $|f|$ and the error $|f - \hat{f}|$ in Fig. 5-3, where it can be observed that the proposed sampling scheme enables the accurate reconstruction, with error on the order of 10^{-7}, over the inaccessible region.

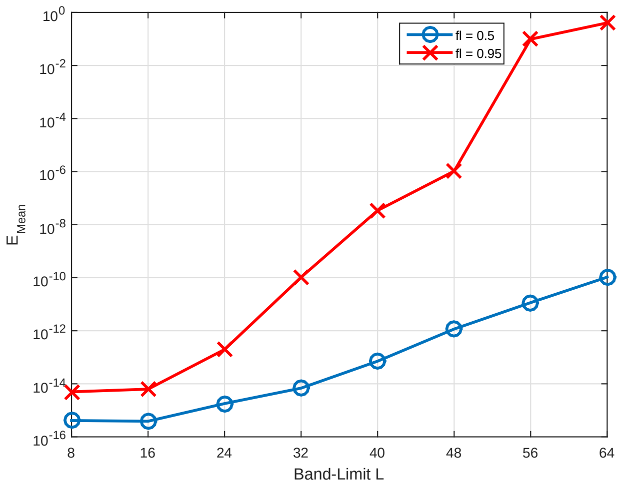

Figure 5-2: Mean error observed when ellipse remains at the North pole ($fl = 0.5$) and when it is rotated to the equatorial belt ($fl = 0.95$) as band-limit varies in the range $8 \leq L \leq 64$. Here $a = 0.1\pi$

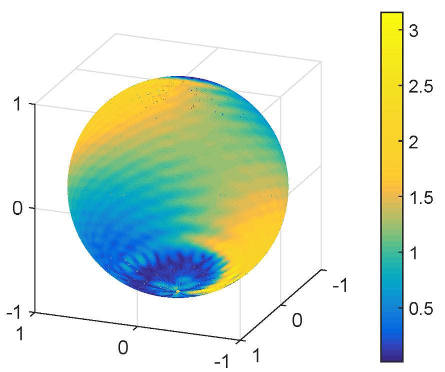

(a) $|f(\hat{\boldsymbol{x}})|$

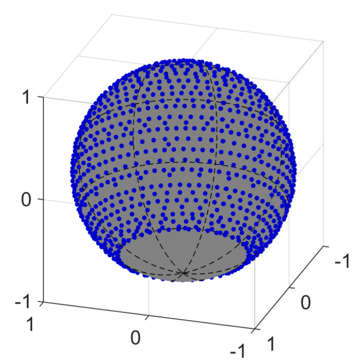

(b) Proposed Sampling Design

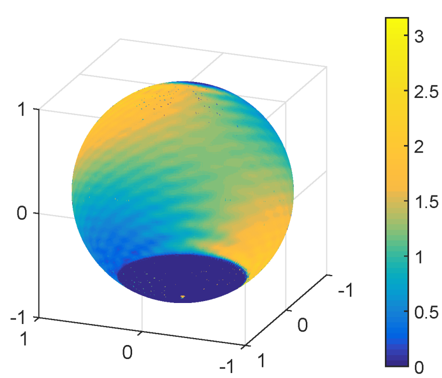

(c) $|f(\hat{\boldsymbol{x}})|$, $\hat{\boldsymbol{x}} \in \mathbb{S}^2 \backslash R$

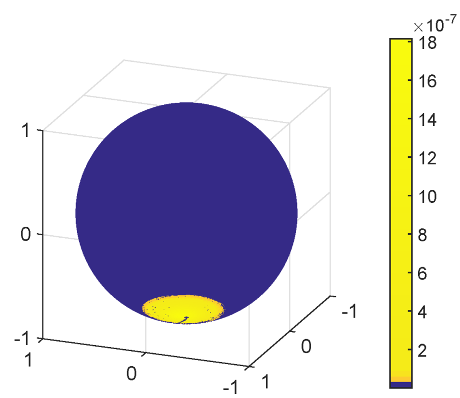

(d) $|f(\hat{\boldsymbol{x}}) - \hat{f}(\hat{\boldsymbol{x}})|$

Figure 5-3: HRTF signal (a) $|f|$, (b) the proposed sampling points for $L = 32$, (c) the known signal $|f|$ and (d) the reconstruction error $|f - \hat{f}|$.

Chapter 6

Efficient Equiangular Sampling on the Sphere

In this chapter, we consider those schemes which enable exact computation of the SHT of band-limited signals. It is desirable for a sampling scheme and its associated SHT algorithm to utilize the least number of samples, exhibit stability, be computationally efficient and have low complexity in order to exactly or accurately represent a band-limited signal on the sphere. In the light of these criteria, we propose a variant of the equiangular sampling scheme [85]: a method for the exact computation of the SHT with a slight increase in the complexity. The motivation behind the design of this scheme is to reduce the number of samples required to represent a spherical signal.

6.1 Equiangular Sampling Scheme on the Sphere

Here we briefly overview the equiangular sampling scheme [85], denoted by $\mathfrak{E}_L$ in this dissertation, which requires $\sim$ (asymptotically) $2L^2$ samples to compute a theoretically exact transform on the sphere. In this scheme, L iso-latitude rings of samples are placed on the sphere, where each ring has $2L-1$ points except for the ring located at the pole which has just one sample point. The co-latitude location of the rings is determined by

$$\theta_t = \frac{\pi(2t+1)}{2L-1}, \qquad \text{where } t \in \{0, 1, \ldots, L-1\}. \tag{6.1}$$

For any ring the sample points are placed along ϕ as

$$\phi_r = \frac{2\pi r}{2L-1}, \qquad \text{where } r \in \{0, 1, \ldots, 2L-2\}. \tag{6.2}$$

The complexity of the SHT associated with this scheme is $O(L^3)$.

6.1.1 Sampling Efficiency

We define the sampling efficiency of a sampling scheme $\mathfrak{X}$ as the ratio of the number of coefficients required to accurately represent a band-limited signal in the harmonic domain, to the number of samples required to represent a signal in the spatial domain. Mathematically it can be written as

$$E(\mathfrak{X}) = \frac{d_L}{N(\mathfrak{X})}, \tag{6.3}$$

where $N(\mathfrak{X})$ represents the total number of samples required by the sampling scheme $\mathfrak{X}$. The optimal value of $E(\mathfrak{X})$ is 1. The sampling efficiency of the equiangular scheme is $E(\mathfrak{C}_L) = \frac{1}{2}$.

6.2 Efficient Equiangular Sampling on the Sphere

We propose a sampling scheme, denoted by $\mathfrak{R}_L$, that requires less than $2L^2$ samples on the sphere to compute an exact SHT.

6.2.1 Proposed Sampling Scheme – Structure and Design

For $L = 2^n, \quad n \in \{1, 2, \ldots\}$, we place $L+1$ iso-latitude rings (of samples) on the sphere at the positions indexed in the vector $\boldsymbol{\theta}$ given by

$$\boldsymbol{\theta} \triangleq [0, \pi, \theta_1,\, \theta_2, \ldots,\, \theta_{L-1}], \tag{6.4}$$

such that the location θ_1 is chosen to be the center of the previous two values of co-latitude rings, that is, $\theta_1 = \pi/2$. We continue to place the remaining rings such that the new rings are placed between the centers of the previously placed rings. For example, the two rings $\theta_2 = \pi/4$, $\theta_3 = 3\pi/4$ are placed at the centers of the previous three rings and the next four rings are placed at the centers of the previous five rings.

We place different number of samples along longitude in each iso-latitude ring. The rings at the poles contain one sample point each. The ring at θ_1 has $2L-1$ equidistant samples along ϕ. For every $k = 1, 2, \ldots, \log_2 L$, the ring at $\theta_x, x \in [2^{k-1}, 2^k - 1]$ has $2L + 1 - 2^k$ samples with longitude location given as

$$\phi_n^x \triangleq \frac{2n\pi}{2L + 1 - 2^k}, \qquad n \in [0, 2L - 2^k]. \tag{6.5}$$

The total number of samples in the proposed sampling scheme $\mathfrak{R}_L$ is given by

$$N(\mathfrak{R}_L) = 2 + \sum_{k=1}^{\log_2 L} 2^{k-1}(2L + 1 - 2^k) = \frac{4}{3}L^2 - L + \frac{5}{3}. \tag{6.6}$$

As $L \to \infty$, the number of samples $N(\mathfrak{R}_L) \to 1.33$. Furthermore, the sampling efficiency of this scheme is $E(\mathfrak{R}_L) = \frac{3}{4}$.

6.2.2 Spherical Harmonic Transform (SHT) – Formulation

We now formulate the SHT associated with the efficient equiangular sampling scheme on the sphere. For a signal $f \in \mathcal{H}_L$, we define

$$F_m(\theta) \triangleq \int_0^{2\pi} f(\theta, \phi) e^{-im\phi} d\phi = 2\pi \sum_{\ell=|m|}^{L-1} (f)_\ell^m \tilde{Y}_\ell^m(\theta), \tag{6.7}$$

as the m-th order Fourier transform of the signal along longitude. Here $\tilde{Y}_\ell^m(\theta) = Y_\ell^m(\theta, 0)$ and we have used (2.8) and the orthogonality of complex exponentials to obtain the second equality. Using $F_m(\theta)$, the signal f can be represented as

$$f(\theta,\phi) = \sum_{m=-(L-1)}^{L-1} F_m(\theta)\, e^{im\phi}. \tag{6.8}$$

The spherical harmonic $\tilde{Y}_\ell^m(\theta)$, a polynomial of degree ℓ in $(\cos\theta)$, can be formulated as

$$\tilde{Y}_\ell^m(\theta) = (\sin\theta)^{|m|}\ Q_\ell^m(\theta), \quad m \geq 0 \tag{6.9}$$

where $Q_\ell^m(\theta)$ is a polynomial of degree $\ell - |m|$ in $(\cos\theta)$. Using (6.9), we can reformulate $F_m(\theta)$ in (6.7) as

$$F_m(\theta) = 2\pi(\sin\theta)^{|m|-1}\ \underbrace{\sin\theta \sum_{\ell=|m|}^{L-1} (f)_\ell^m Q_\ell^m(\theta)}_{H_m(\theta)}. \tag{6.10}$$

Here $H_m(\theta)$ is a polynomial of degree $L - |m|$ and therefore can be expanded in terms of complex exponentials as

$$H_m(\theta) = \sum_{m'=-(L-m)}^{(L-m)} H_{m,m'}\, e^{im'\theta}. \tag{6.11}$$

We further note that $H_m(0) = H_m(\pi) = 0, \quad |m| \neq 0$. Using the following expansion of spherical harmonic in terms of Wigner-d functions [1]

$$\tilde{Y}_\ell^m(\theta) = i^{-m}\sqrt{\frac{2\ell+1}{4\pi}} \sum_{u=-\ell}^{\ell} \Delta_{u,m}^\ell \Delta_{u,0}^\ell e^{iu\theta}, \tag{6.12}$$

where $\Delta_{u,m}^\ell = d_{u,m}^\ell(\pi/2)$ is the Wigner-d function of degree ℓ and orders u, m evaluated at $\pi/2$, we can compute the spherical harmonic transform as

$$\begin{aligned}
(f)_\ell^m &= \int_{\theta=0}^{\pi} F_m(\theta)\tilde{Y}_\ell^m(\theta)\sin\theta d\theta, \\
&= i^{-m}\sqrt{\pi(2\ell+1)} \sum_{m'=-(L-m)}^{(L-m)} \sum_{u=-\ell}^{\ell} H_{m,m'}\Delta_{u,m}^{\ell}\times \\
&\quad \Delta_{u,0}^{\ell} \underbrace{\int_{\theta=0}^{\pi} (\sin\theta)^m e^{i(u+m')\theta} d\theta}_{I(m,u+m')} . \qquad (6.13)
\end{aligned}$$

The integral in (6.13) can be computed as [103]

$$\begin{aligned}
I(p,q) &= \int_{\theta=0}^{\pi} (\sin\theta)^p e^{iq\theta} d\theta \\
&= \frac{\pi\, e^{iq\pi/2}\Gamma(p+2)}{2^p(p+1)\Gamma(\frac{p+q+2}{2})\Gamma(\frac{p-q+2}{2})} . \qquad (6.14)
\end{aligned}$$

The method of computing the spherical harmonic coefficients using this transform is explained below.

6.3 Computation of the Spherical Harmonic Transform (SHT)

For the computation of the SHT using the formulation in (6.13), we are required to compute $H_{m,m'}$, which can be computed using $H_m(\theta)$, which is simply a scaled multiple of $F_m(\theta)$. In the forth-coming subsections we give a detailed explanation of these steps for different values of the order m.

6.3.1 Compute SHT for order $|m| = L - 1$

Since $f(\theta, \phi)$ is composed of $2L-1$ complex exponentials as given in (6.8), we can compute $F_m(\theta)$ for all $|m| \leq L-1$ *exactly* by taking FFT over $2L-1$ samples along the longitude. Starting with the ring located at $\theta_1 = \pi/2$, we first compute $F_m(\theta_1)$ followed by $H_m(\theta_1)$ and then compute $H_{mm'}$ for $|m| = L-1$. Using $H_{L-1,m'}$, we can determine the spherical harmonic coefficients $(f)_\ell^m$ for $|m| = L-1$ and $\ell = L-1$.

We use $(f)_{L-1}^m$, $|m| = L-1$ to update the values of the signal at the samples taken on the rings placed at $\theta_2, \theta_3, \ldots, \theta_{L-1}$

$$f(\theta,\phi) \leftarrow f(\theta,\phi) - \tilde{f}_{L-1}(\theta,\phi), \tag{6.15}$$

where

$$\tilde{f}_m(\theta,\phi) = \sum_{\ell=m}^{L-1} \left((f)_\ell^m Y_\ell^m(\theta,\phi) + (f)_\ell^{-m} Y_\ell^{-m}(\theta,\phi)\right), \tag{6.16}$$

is the part of the signal $f(\theta,\phi)$ synthesized using the spherical harmonic coefficients of orders m, $-m$ and all degrees $m \le \ell < L$.

6.3.2 Compute SHT for orders $|m| = L-2$ and $|m| = L-3$

The signal after the update given in (6.15) can be expanded as

$$f(\theta,\phi) = \sum_{m=-(L-2)}^{L-2} F_m(\theta)\, e^{im\phi}, \tag{6.17}$$

which means that the computation of $F_m(\theta)$ now requires at-least $2L-3$ samples of the updated signal along longitude.

As we take $2L-3$ samples in the rings placed at θ_k, $k=[2,3]$, we compute $F_m(\theta_k)$ using FFT along longitude for these rings for all $|m| \le L-2$. Now we have $F_m(\theta_k)$ and $H_m(\theta_k)$ for $k=1,2,3$ since $F_m(\theta_1)$ has been already computed for all $|m| \le L-1$.

We extend the domain of co-latitude θ to $(\pi, 2\pi)$ so that we can utilize the FFT for the computation of $H_{mm'}$ from $H_m(\theta)$. Noting $\tilde{Y}_\ell^m(2\pi-\theta) = (-1)^m \tilde{Y}_\ell^m(\theta)$, we define $\tilde{H}_m(\theta)$ over the extended domain as

$$\tilde{H}_m(\theta) = \begin{cases} H_m(\theta), & \theta \in [0,\pi], \\ H_m(2\pi-\theta), & \theta \in (\pi, 2\pi). \end{cases} \tag{6.18}$$

Following this periodic extension, we have $H_m(\theta_k)$ for $|m| \leq L-2$ and for 8 equiangular points $(0, \pi, \theta_k, 2\pi - \theta_k,\ k = 1, 2, 3)$ and therefore FFT can be used to recover $H_{m,m'}$ for $|m| = L-2$ and $|m| = L-3$. Once $H_{m,m'}$ is determined, it is used to compute spherical harmonic coefficients $(f)_\ell^m$ for orders $|m| = L-2, L-3$ and all degrees $|m| \leq \ell < L$.

Next, we update the signal as

$$f(\theta, \phi) \leftarrow f(\theta, \phi) - \tilde{f}_{L-2}(\theta, \phi) - \tilde{f}_{L-3}(\theta, \phi). \tag{6.19}$$

6.3.3 Compute SHT for orders $1 \leq |m| < L-3$

For the remaining values of $|m|$, we follow the same pattern as discussed in Section III-A. For Example, $|m| = L-1$, we needed one ring. Then we worked with two more rings for $|m| = L-2$ and $|m| = L-3$. So now we will need four more rings to compute the coefficients of orders $|m| = L-3, \ldots, L-6$, and update the signal. After that we need eight more rings to determine the coefficients orders $|m| = L-7, \ldots, L-14$ and so on. We repeat this process for all orders up to $|m| = 1$.

6.3.4 Compute SHT for order $m = 0$

Since $F_0(\theta)$ is a polynomial in $\cos\theta$ of degree $L-1$, it can be expanded as

$$F_0(\theta) = \sum_{m'=-(L-1)}^{(L-1)} F_{0,m'}\, e^{im'\theta}. \tag{6.20}$$

We also define $F_0(\theta)$ over the extended domain $(\pi, 2\pi)$ as

$$F_0(2\pi - \theta) = F_0(\theta) \qquad \theta \in (\pi, 2\pi). \tag{6.21}$$

Following the computation of spherical harmonic coefficients of all orders $1 \leq |m| < L$, we have $F_0(\theta_k)$ for all $L+1$ rings ($\theta_k \in \boldsymbol{\theta}$, including samples at the poles). By defining F_0 over the extended domain $[0, 2\pi)$ as in (6.21), we extended $\tilde{F}_m(\theta_k)$ over $2L$ points.

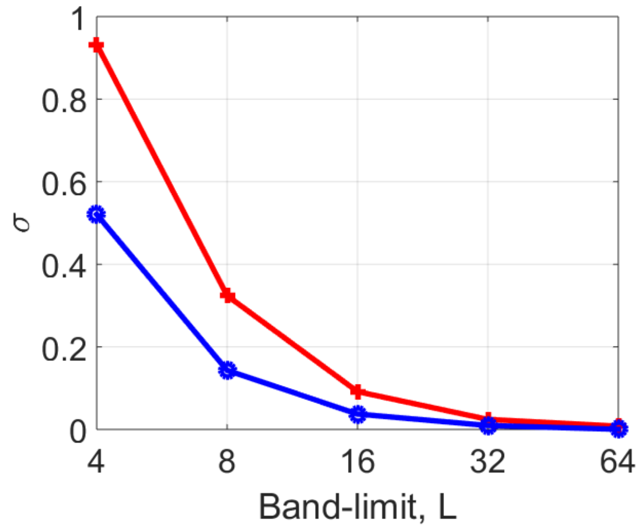

(a) Normalized Minimum Geodesic Distance

Figure 6-1: Comparison of the normalized minimum geodesic distance. The proposed and equiangular sampling scheme is shown in red and blue colour respectively.

We can use FFT over the extended domain to recover $F_{0,m'}$, formulated in (6.20), using which we compute the spherical harmonic coefficients for $m = 0$ as

$$\begin{aligned}(f)_\ell^0 &= \int_{\theta=0}^{\pi} F_0(\theta)\tilde{Y}_\ell^0(\theta)\sin\theta d\theta,\\ &= \sqrt{\pi(2\ell+1)}\sum_{m'=-(L-1)}^{(L-1)}\sum_{u=-\ell}^{\ell} F_{0,m'}\left(\Delta_{u,0}^{\ell}\right)^2 I(u+m').\end{aligned} \tag{6.22}$$

The integral in (6.22) can be computed as

$$I(q) = \int_{\theta=0}^{\pi}(\sin\theta)e^{iq\theta}d\theta = \begin{cases}\frac{2}{1-q^2} & q \text{ even},\\ \frac{\pm i\pi}{2} & q = \pm 1,\\ 0 & \text{otherwise},\end{cases} \tag{6.23}$$

6.4 Analysis and Evaluation

We now discuss some attributes of the efficient sampling scheme $\mathfrak{R}_L$. The SHT algorithm associated with the proposed scheme is an exact method but has a higher

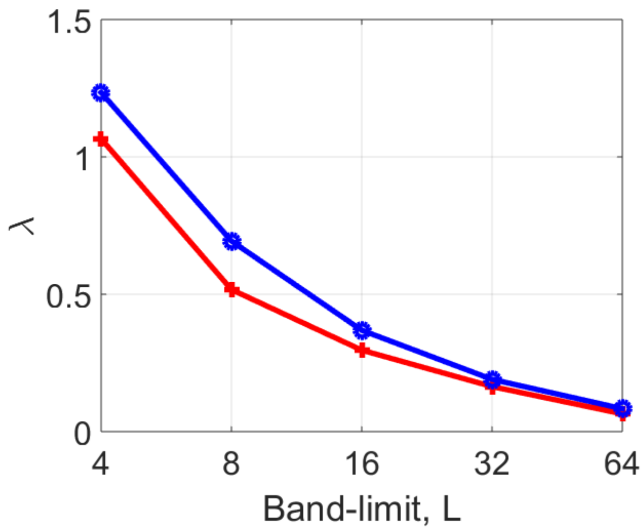

(a) Mesh Norm

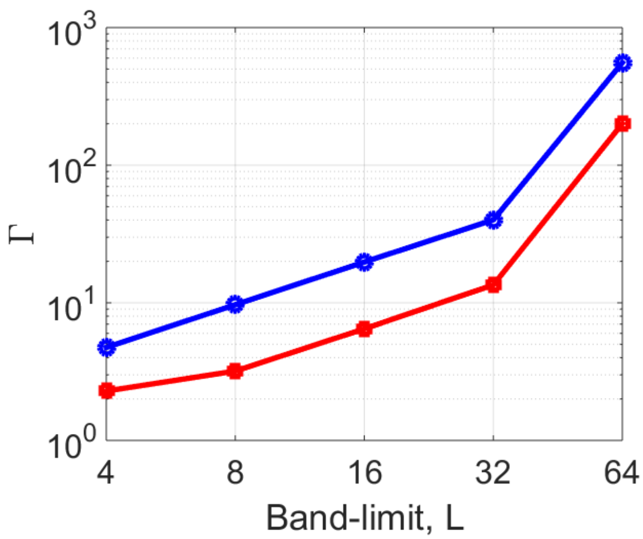

(b) Mesh Ratio

Figure 6-2: Comparison of the geometrical properties (a) mesh norm and (b) mesh ratio. The proposed and equiangular sampling scheme is shown in red and blue colour respectively.

complexity as compared to equiangular sampling scheme. We analyse a few geometrical properties defined below:

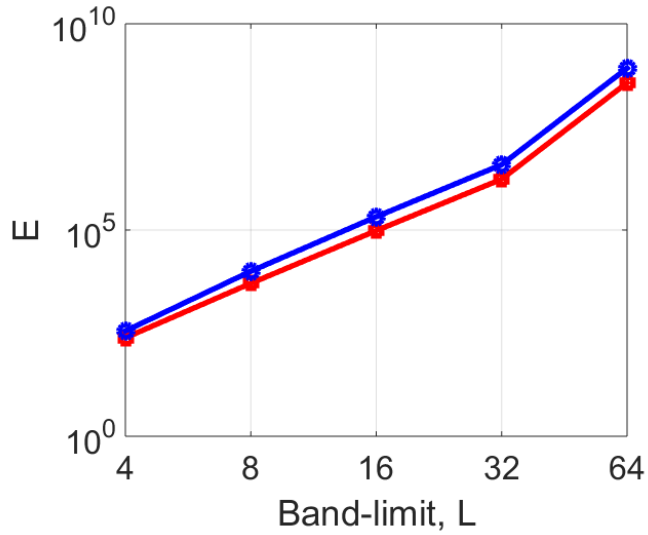

(a) Riesz s-energy

Figure 6-3: Comparison of the Riesz s-energy for $s = 1$. The proposed and equiangular sampling scheme is shown in red and blue colour respectively.

6.4.1 Normalized Minimum Geodesic Distance

The smallest great circle or spherical distance between two points $\hat{\boldsymbol{u}}(\theta_u, \phi_u)$ and $\hat{\boldsymbol{v}}(\theta_v, \phi_v)$ divided by the sampling efficiency, given by $\sigma(\mathfrak{R}_L) \triangleq \frac{1}{E(\mathfrak{R}_L)} \min_{\hat{\boldsymbol{u}}, \hat{\boldsymbol{v}} \in \mathfrak{R}_L} \Delta(\hat{\boldsymbol{u}}, \hat{\boldsymbol{v}})$, where

$$\Delta(\hat{\boldsymbol{u}}, \hat{\boldsymbol{v}}) = \cos^{-1}\left(\cos\theta_u \cos\theta_v + \sin\theta_u \sin\theta_v \cos(\phi_u - \phi_v)\right). \tag{6.24}$$

It is desirable to have a higher value of the normalized minimum geodesic distance.

6.4.2 Mesh Norm

The smallest (spherical) radius of a covering of the sphere by spherical caps centered at sampling point $\hat{\boldsymbol{u}} \in \mathfrak{R}_L$, mathematically given by

$$\lambda(\mathfrak{R}_L) \triangleq \frac{1}{E(\mathfrak{R}_L)} \max_{\hat{\boldsymbol{u}}} \min_{\hat{\boldsymbol{v}}} \Delta(\hat{\boldsymbol{u}}, \hat{\boldsymbol{v}}). \tag{6.25}$$

The lower the mesh norm, the better the sampling scheme.

6.4.3 Mesh Ratio

The ratio of twice the mesh norm to the normalized geodesic distance is called the mesh ratio and is mathematically given as

$$\Gamma(\mathfrak{R}_L) = \frac{2\lambda(\mathfrak{R}_L)}{\sigma(\mathfrak{R}_L)}. \tag{6.26}$$

A lower value of the mesh ratio is evidence of a good sampling scheme.

6.4.4 Riesz s-Energy

The Riesz s-energy is defined as

$$\mathcal{E}_s \;=\; \sum_{\hat{\boldsymbol{u}},\hat{\boldsymbol{v}}\in\mathfrak{R}_L \;\hat{\boldsymbol{u}}\neq\hat{\boldsymbol{v}}} \frac{1}{(\Delta(\hat{\boldsymbol{u}},\hat{\boldsymbol{v}}))^s}. \tag{6.27}$$

We prefer the Riesz s-energy to be lower for a good sampling scheme. We compare the geometrical properties of the equiangular sampling scheme and the proposed scheme in Fig. 6.1 – 6.3, where we can see that the proposed scheme (red lines) performs better than the equiangular scheme (blue lines).

Chapter 7

Conclusions and Future Work

This chapter draws conclusions and provides insights to the work presented in this thesis. In addition, the way forward to extend this research further and to improve the proposed design is also given.

7.1 Conclusions

In this thesis, we first presented Slepian functions on the sphere and the ball. We have propoesed a generalization of the Slepian concentration problem on the sphere by introducing weighting functions in the formulation of the problem. Assigning different values to the weighting functions, we have formulated the two variants: differential and weighted Slepian concentration problems of finding band-limited optimally concentrated functions on the sphere. The differential Slepian concentration problem takes into account two regions on the sphere and maximises the energy concentration of a band-limited signal in one region while the energy is minimized in the other region. The weighted Slepian concentration problem uses non-negative weighting as a window function in the formulation for the localization of the signal energy. The solution of each problem yields eigenfunctions, referred to as Slepian functions, that serve as alternative basis functions for the representation of band-limited functions. We have also presented and analysed the properties of the proposed Slepian functions. Furthermore, we demonstrated the usefulness of the proposed Slepian functions for signal representation, localized spectrum estimation and signal modeling to support the applications in cosmology, geophysics, acoustics and beyond.

Based on the Slepian problem on the unit ball, we have presented the design of complete orthonormal optimal basis functions with simultaneous maximal energy concentration in both the spectral (harmonic) and spatial domain. We design optimal basis as a linear combination of spectrally concentrated space-limited functions and spatially concentrated band-limited functions. The proposed developments have been presented in the form of 3 theorems. First, we have determined the optimal weights which maximise the product of concentration of energy in harmonic and spatial domains. We have also shown that the proposed optimal basis functions span the subspace given by the vector sum of subspace of space-limited spectrally concentrated functions and subspace of band-limited spatially concentrated functions. We have also formulated the integral operator as a projection operator that projects the signal on the ball to the vector sum of subspaces and maximises the product of energy concentrations in harmonic as well as spatial domains. We have also shown that the proposed optimal bases are the only eigenfunctions of the proposed integral operator. We reviewed some of the properties of proposed optimal bases.

The second area of focus in this thesis is related to the sampling schemes on the sphere and their associated spherical harmonic transforms (SHTs). We have proposed variations in the SHT associated with the optimal-dimensionality sampling scheme which consist of iso-latitude rings of samples and enables accurate computation of the SHT of band-limited signals using the optimal number of samples given by the degrees of freedom required to represent a band-limited signal in harmonic space. We have presented the elimination method for the iterative placement of iso-latitude rings of samples. The proposed placement reduces the condition number of matrices involved in the computation of SHT and consequently improves the accuracy of the SHT. We have also proposed the multi-pass SHT algorithm which iteratively reduces the residual between the given signal and the reconstructed signal and therefore improves the overall accuracy of the SHT. We have analysed the changes in the computational complexity and improvement in accuracy with the use of proposed variations in the computation of the SHT. We have also conducted numerical experiment to illustrate the improvement in accuracy enabled by the proposed methods.

We have proposed an antipodally symmetric sampling scheme on the unit sphere for the sampling of band-limited signals. Using the proposed scheme, the accurate computation of the SHT can be done by taking (asymptotically) L^2 number of samples of the signal with band-limit L. The proposed scheme attains optimal spatial dimensionality because the number of samples are asymptotically equal to the degrees of freedom of the signal in harmonic space. While formulating the SHT associated with the proposed sampling scheme, we used the antipodal symmetry of the sampling points. This separates the signal into antipodally symmetric and asymmetric signals due to which the signal also splits in harmonic space into the signals of even and odd spherical harmonic degrees. This type of splitting allows our method to be computationally efficient by a factor of four as compared to the existing sampling schemes that attain optimal spatial dimensionality. To analyse the numerical accuracy of the proposed SHT, we conducted numerical experiments and showed that the proposed sampling and its associated SHT enable accurate signal reconstruction for signals in the band-limit range $15 \leq L \leq 127$.

In chapter 5, we propose a spatially-limited sampling scheme for the computation of spherical harmonic coefficients (using a multi-pass SHT algorithm) of a band-limited signal when an arbitrary region on the sphere is inaccessible for taking signal measurements or samples. We propose to place iso-latitude rings of samples on the sphere after the exclusion of the minimum area ellipsoidal region enclosing the inaccessible region. Prior to sampling, the ellipsoidal region may be rotated to the polar cap or the equatorial belt depending upon the surface area available for placement of samples in each case. Placement of the rings according to the proposed method results in accurate computation of the SHT. The numerical accuracy of the proposed sampling scheme was analysed and gives promising results. As an illustration we compute the SHT of the HRTF signal using the proposed spatially-limited sampling method and note that its accuracy has improved as compared to the existing schemes.

Lastly, we proposed an efficient variant of the equiangular sampling scheme for the computation of spherical harmonic coefficients of a band-limited signal on the sphere. The proposed sampling scheme is an exact method to compute the SHTs. We also presented the harmonic formulation and method of computation of the SHT algorithm associated with the proposed scheme. Since the proposed sampling scheme uses fewer number of samples as compared to the equiangular sampling scheme, it results in a faster SHT algorithm with higher sampling efficiency. We also demonstrate that the proposed sampling scheme outperforms the equiangular sampling scheme in terms of the geometrical properties such as normalized minimum geodesic distance, mesh norm, mesh ratio and Riesz s-energy.

7.2 Future Work

Below we provide details of the potential future research directions:

- The variations of the sampling schemes which are proposed in this thesis require an optimal number of samples and exhibit the smallest attainable reconstruction error. Future research related to sampling schemes on the sphere should consider applications where the number of measurements required for the computation of the SHT is less than the optimal number. Reducing the samples in such a way will lead to a compromise on the accuracy of the SHT.

- The differential and weighted Slepian functions on the sphere presented in chapter 3 of this thesis, may be further extended to higher dimensions, i.e., on the ball $\mathbb{B}^3$. A manuscript related to this work is already under preparation, and mentioned here for ease of reference:

C5. **W. Nafees**, and Z. Khalid, “Differential and weighted Slepian functions on the Ball,” in *IEEE Int. Conf. Acoust., Speech and Signal Process., ICASSP’2021*, Toronto, Canada, June 2021, (to be submitted).

- In this thesis, we use the Fourier-Laguerre basis functions for the representation of signal on the ball in the harmonic domain. In chapter 3, we carried out spectral estimation on the sphere. It may be interesting to investigate how the Fourier-Laguerre basis functions can be utilized for localized spectral estimation on the ball.

- In chapter 4, we proposed the multi-pass SHT technique to reduce the reconstruction error in the SHT algorithm related to the optimal dimensionality sampling scheme. The multi-pass SHT method can be applied to other sampling schemes and their associated SHT algorithms to reduce the reconstruction error, for example, the equiangular sampling scheme.

- In chapter 6, we proposed an efficient equiangular sampling scheme on the sphere wherein we reduced the number of samples by compromising the complexity of the associated algorithm. We may explore other methods to reduce the number of samples required to represent a signal on the sphere by compromising some other attribute of the sampling scheme, for instance the exactness, efficiency, etc. The concept of polar optimization can be used for this purpose and a manuscript related to this work is already in the pipeline by the author, and being mentioned here as a reminder:

J3. **W. Nafees**, Z. Khalid, and J. D. McEwen, "Polar-optimized Equiangular Sampling Scheme on the Sphere," *IEEE Signal Process. Letters*, (to be submitted), 2020.

Appendix

Orthogonality of the Differential Slepian Functions

Proof. Using the definition of the differential Slepian functions:

$$\langle f_\alpha, f_\beta \rangle_{R_1} - \langle f_\alpha, f_\beta \rangle_{R_2} = \lambda_\alpha \langle f_\alpha, f_\beta \rangle_{\mathbb{S}^2} . \tag{7.1}$$

If $\alpha = \beta$, then $\langle f_\alpha, f_\alpha \rangle_{R_2} \geq 0$ and $\langle f_\alpha, f_\alpha \rangle_{\mathbb{S}^2} = 1$, therefore (7.1) reduces to

$$\langle f_\alpha, f_\alpha \rangle_{R_1} \geq \lambda_\alpha. \tag{7.2}$$

Say $\mathbb{S}^2 = R_1 + R_2 + R_*$, then for $\alpha \neq \beta$ we can rewrite (3.20) as

$$\langle f_\alpha, f_\beta \rangle_{R_1} + \langle f_\alpha, f_\beta \rangle_{R_2} + \langle f_\alpha, f_\beta \rangle_{R_*} = 0. \tag{7.3}$$

Adding (7.1) and (7.3) we get

$$2 \langle f_\alpha, f_\beta \rangle_{R_1} = - \langle f_\alpha, f_\beta \rangle_{R_*} . \tag{7.4}$$

Using the Cauchy-Schwarz inequality for $\langle f_\alpha, f_\beta \rangle_{R_*}$, we get

$$| \langle f_\alpha, f_\beta \rangle_{R_*} | \leq \sqrt{\langle f_\alpha, f_\alpha \rangle_{R_*}} \sqrt{\langle f_\beta, f_\beta \rangle_{R_*}}, \tag{7.5}$$

where

$$\begin{aligned}\sqrt{\langle f_\alpha, f_\alpha\rangle_{R_*}} &= \sqrt{\langle f_\alpha, f_\alpha\rangle_{\mathbb{S}^2} - \langle f_\alpha, f_\alpha\rangle_{R_1} - \langle f_\alpha, f_\alpha\rangle_{R_2}} \\ &\leq \sqrt{1 - \langle f_\alpha, f_\alpha\rangle_{R_1}} \\ &\leq \sqrt{1-\lambda_\alpha}. \end{aligned} \tag{7.6}$$

So (7.5) implies that $|\langle f_\alpha, f_\beta\rangle_{R_*}| \leq \sqrt{1-\lambda_\alpha}\,\sqrt{1-\lambda_\beta}$ and using this in (7.4) results in

$$|\langle f_\alpha, f_\beta\rangle_{R_1}| \leq \frac{1}{2}\sqrt{1-\lambda_\alpha}\,\sqrt{1-\lambda_\beta}. \tag{7.7}$$

To find the bound on the angle between two Slepian functions, we use (7.7) in the definiton of inner product as

$$|f_\alpha|_{R_1}|f_\beta|_{R_1}|\cos\gamma_{f_\alpha,f_\beta}| \leq \frac{1}{2}\sqrt{1-\lambda_\alpha}\,\sqrt{1-\lambda_\beta}. \tag{7.8}$$

Since

$$\lambda_\alpha = |f_\alpha|^2_{R_1} - |f_\alpha|^2_{R_2} \;\Rightarrow\; \lambda_\alpha \leq |f_\alpha|^2_{R_1}. \tag{7.9}$$

Then for positive eigenvalues, we can say $\sqrt{\lambda_\alpha} \leq |f_\alpha|_{R_1}$, or

$$\frac{1}{|f_\alpha|_{R_1}} \leq \frac{1}{\sqrt{\lambda_\alpha}}. \tag{7.10}$$

Rearranging (7.8) and employing (7.10), we can prove that

$$|\cos\gamma_{f_\alpha,f_\beta}| \leq \frac{1}{2}\frac{\sqrt{1-\lambda_\alpha}\,\sqrt{1-\lambda_\beta}}{\sqrt{\lambda_\alpha}\,\sqrt{\lambda_\beta}} \qquad \lambda_{\alpha,\beta} > 0. \tag{7.11}$$

$\square$

Bibliography

[1] R. A. Kennedy and P. Sadeghi, *Hilbert Space Methods in Signal Processing*. Cambridge, UK: Cambridge University Press, Mar. 2013.

[2] Z. Khalid, R. A. Kennedy, and J. D. McEwen, "An optimal-dimensionality sampling scheme on the sphere with fast spherical harmonic transforms," *IEEE Transactions on Signal Processing*, vol. 62, no. 17, pp. 4597–4610, 2014.

[3] M. Tegmark, M. A. Strauss, M. R. Blanton, K. Abazajian, S. Dodelson, H. Sandvik, X. Wang, D. H. Weinberg, I. Zehavi, N. A. Bahcall *et al.*, "Cosmological parameters from SDSS and WMAP," *Physical Review D*, vol. 69, no. 10, p. 103501, 2004.

[4] M. A. Wieczorek and F. J. Simons, "Minimum variance multitaper spectral estimation on the sphere," *J. Fourier Anal. Appl.*, vol. 13, no. 6, pp. 665–692, 2007.

[5] F. Lowes, "Spatial power spectrum of the main geomagnetic field, and extrapolation to the core," *Geophys. J. Int.*, vol. 36, no. 3, pp. 717–730, 1974.

[6] A. P. Bates, Z. Khalid, and R. A. Kennedy, "Novel sampling scheme on the sphere for head-related transfer function measurements," *IEEE/ACM Trans. on Audio, Speech and Lang. Process. (TASLP)*, vol. 23, no. 6, pp. 1068–1081, 2015.

[7] W. Zhang, M. Zhang, R. A. Kennedy, and T. D. Abhayapala, "On high-resolution head-related transfer function measurements: An efficient sampling

scheme," *IEEE Trans. Acoust., Speech, Signal Process.*, vol. 20, no. 2, pp. 575–584, 2012.

[8] R. Ramamoorthi and P. Hanrahan, "A signal-processing framework for reflection," *ACM Transactions on Graphics (TOG)*, vol. 23, no. 4, pp. 1004–1042, 2004.

[9] T. Bülow, "Spherical diffusion for 3D surface smoothing," *IEEE Trans. Pattern Anal. Mach. Intell.*, vol. 26, no. 12, pp. 1650–1654, Dec. 2004.

[10] R. Ng, R. Ramamoorthi, and P. Hanrahan, "Triple product wavelet integrals for all-frequency relighting," *ACM Trans. Graph.*, vol. 23, no. 3, pp. 477–487, Aug. 2004.

[11] C. Han, B. Sun, R. Ramamoorthi, and E. Grinspun, "Frequency domain normal map filtering," *ACM Trans. on Graphics*, vol. 26, no. 3, pp. 28:1–28:12, Jul. 2007.

[12] P. Schröder and W. Sweldens, "Spherical wavelets: Efficiently representing functions on a sphere," in *Wavelets in the Geosciences*. Springer, 2000, pp. 158–188.

[13] B. Leistedt and J. D. McEwen, "Exact wavelets on the ball," *IEEE Trans. Signal Process.*, vol. 60, no. 12, pp. 6257–6269, 2012.

[14] F. J. Simons and D. V. Wang, "Spatiospectral concentration in the Cartesian plane," *GEM-Int. J. Geomathematics*, vol. 2, no. 1, pp. 1–36, 2011.

[15] M. A. Wieczorek, "Gravity and topography of the terrestrial planets," *Treatise on geophysics*, vol. 10, no. 206, pp. 165–989, 2007.

[16] C. Armitage and B. D. Wandelt, "Deconvolution map-making for cosmic microwave background observations," *Physical Review D*, vol. 70, no. 12, p. 123007, 2004.

[17] K.-W. Ng, "Full-sky correlation functions for CMB experiments with asymmetric window functions," *Physical Review D*, vol. 71, no. 8, p. 083009, 2005.

[18] J. D. McEwen, P. Vielva, Y. Wiaux, R. B. Barreiro, L. Cayón, M. P. Hobson, A. N. Lasenby, E. Martinez-Gonzalez, and J. L. Sanz, “Cosmological applications of a wavelet analysis on the sphere,” *Journal of Fourier Analysis and Applications*, vol. 13, no. 4, pp. 495–510, 2007.

[19] J. McEwen, M. Hobson, A. Lasenby, and D. Mortlock, “A high-significance detection of non-Gaussianity in the Wilkinson microwave anisotropy probe 1-yr data using directional spherical wavelets,” *Monthly Notices of the Royal Astronomical Society*, vol. 359, no. 4, pp. 1583–1596, 2005.

[20] J.-L. Starck, Y. Moudden, P. Abrial, and M. Nguyen, “Wavelets, ridgelets and curvelets on the sphere,” *Astron. & Astrophys.*, vol. 446, no. 3, pp. 1191–1204, Feb. 2006.

[21] D. N. Spergel, R. Bean, O. Doré, M. R. Nolta, C. L. Bennett, J. Dunkley, G. Hinshaw, N. Jarosik, E. Komatsu, L. Page, H. V. Peiris, L. Verde, M. Halpern, R. S. Hill, A. Kogut, M. Limon, S. S. Meyer, N. Odegard, G. S. Tucker, J. L. Weiland, E. Wollack, and E. L. Wright, “Three-year Wilkinson Microwave Anisotropy Probe (WMAP) observations: Implications for cosmology,” *The Astrophysical Journal Supplement Series*, vol. 170, no. 2, pp. 377–408, 2007.

[22] T. S. Pollock, T. D. Abhayapala, and R. A. Kennedy, “Introducing space into MIMO capacity calculations,” *J. Telecommun. Syst.*, vol. 24, no. 2, pp. 415–436, Oct. 2003.

[23] A. Albertella, F. Sansò, and N. Sneeuw, “Band-limited functions on a bounded spherical domain: the Slepian problem on the sphere,” *J. Geodesy*, vol. 73, no. 9, pp. 436–447, Jun. 1999.

[24] Y. F. Alem, Z. Khalid, and R. A. Kennedy, “3D spatial fading correlation for uniform angle of arrival distribution,” *IEEE Commun. Lett.*, vol. 19, pp. 1073–1076, June 2015.

[25] A. P. Bates, Z. Khalid, and R. A. Kennedy, "Slepian spatial-spectral concentration problem on the sphere: Analytical formulation for limited colatitude–longitude spatial region," *IEEE Trans. on Signal Process.*, vol. 65, no. 6, pp. 1527–1537, 2016.

[26] P. Sadeghi, R. A. Kennedy, and Z. Khalid, "Commutative anisotropic convolution on the 2-sphere," *IEEE Trans. Signal Process.*, vol. 60, no. 12, pp. 6697–6703, Dec. 2012.

[27] J. R. Driscoll and D. M. Healy, Jr., "Computing Fourier transforms and convolutions on the 2-sphere," *Adv. Appl. Math.*, vol. 15, no. 2, pp. 202–250, Jun. 1994.

[28] R. A. Kennedy, T. A. Lamahewa, and L. Wei, "On azimuthally symmetric 2-sphere convolution," *Digital Signal Processing*, vol. 5, no. 11, pp. 660–666, Sep. 2011.

[29] J. D. McEwen, M. P. Hobson, and A. N. Lasenby, "Optimal filters on the sphere," *IEEE Trans. Signal Process.*, vol. 56, no. 8, pp. 3813–3823, Aug. 2008.

[30] B. T. T. Yeo, W. Ou, and P. Golland, "On the construction of invertible filter banks on the 2-sphere," *IEEE Trans. Image Process.*, vol. 17, no. 3, pp. 283–300, Mar. 2008.

[31] Z. Khalid, S. Durrani, R. A. Kennedy, and P. Sadeghi, "On the construction of low-pass filters on the unit sphere," in *Proc. IEEE Int. Conf. Acoust., Speech, Signal Process., ICASSP'2011*, Prague, Czech Republic, May 2011, pp. 4356–4359.

[32] Z. Khalid, P. Sadeghi, R. A. Kennedy, and S. Durrani, "Spatially varying spectral filtering of signals on the unit sphere," *IEEE Trans. Signal Process.*, vol. 61, no. 3, pp. 530–544, Feb. 2013.

[33] M. A. Wieczorek and F. J. Simons, "Localized spectral analysis on the sphere," *Geophys. J. Int.*, vol. 162, no. 3, pp. 655–675, Sep. 2005.

[34] F. J. Simons, F. A. Dahlen, and M. A. Wieczorek, “Spatiospectral concentration on a sphere,” *SIAM Rev.*, vol. 48, no. 3, pp. 504–536, 2006.

[35] F. J. Simons, I. Loris, G. Nolet, I. C. Daubechies, S. Voronin, P. A. Vetter, J. Charléty, and C. Vonesch, “Solving or resolving global tomographic models with spherical wavelets, and the scale and sparsity of seismic heterogeneity,” *Geophys. J. Int.*, vol. 187, pp. 969–988, 2011.

[36] F. Lanusse, A. Rassat, , and J.-L. Starck, “Spherical 3D isotropic wavelets,” *Astron. & Astrophys.*, vol. 540, p. A92, Apr. 2012.

[37] D. Slepian and H. O. Pollak, “Prolate spheroidal wave functions, Fourier analysis and uncertainity-I,” *Bell Syst. Tech. J.*, vol. 40, pp. 43–63, Jan. 1961.

[38] H. J. Landau and H. O.Pollak, “Prolate spheroidal wave functions, Fourier analysis and uncertainity-II,” *Bell Syst. Tech. J.*, vol. 40, pp. 65–84, Jan. 1961.

[39] D. Slepian, “Prolate spheroidal wave functions, Fourier analysis and uncertainity-IV: Extensions to many dimensions; generalized prolate spheroidal functions,” *Bell Syst. Tech. J.*, vol. 43, pp. 3009–3057, 1964.

[40] H. J. Landau and H. O.Pollak, “Prolate spheroidal wave functions, Fourier analysis and uncertainity-III: The dimension of the space of essentially time- and band-limited signals,” *Bell Syst. Tech. J.*, vol. 41, pp. 1295–1336, 1962.

[41] Z. Khalid, R. A. Kennedy, and J. D. McEwen, “Slepian spatial-spectral concentration on the ball,” *Appl. and Computational Harmonic Anal.*, vol. 40, no. 3, pp. 470–504, 2016.

[42] I. C. Moore and M. Cada, “Prolate spheroidal wave functions, an introduction to the Slepian series and its properties,” *Appl. and Computational Harmonic Anal.*, vol. 16, no. 3, pp. 208–230, 2004.

[43] J. A. Hogan and J. D. Lakey, *Duration and Bandwidth Limiting: Prolate Functions, Sampling, and Applications.* Springer Science & Business Media, 2011.

[44] R. S. Dilmaghani, M. Ghavami, B. Allen, and H. Aghvami, "Novel UWB pulse shaping using prolate spheroidal wave functions," in *Proc. 14th IEEE Personal, Indoor and Mobile Radio Commun., PIMRC 2003*, Sept. 2003, pp. 602–606.

[45] S. Haykin and D. J. Thomson, "Signal detection in a nonstationary environment reformulated as an adaptive pattern classification problem," *Proceedings of the IEEE*, vol. 86, no. 11, pp. 2325–2344, 1998.

[46] W. Xu and C. Chamzas, "On the extrapolation of band-limited functions with energy constraints," *IEEE Trans. Acoust., Speech and Signal Process.*, vol. 31, no. 5, pp. 1222–1234, 1983.

[47] L. Gosse, "Effective band-limited extrapolation relying on Slepian series and ℓ_1 regularization," *Computers & Mathematics with Appl.*, vol. 60, no. 5, pp. 1259–1279, 2010.

[48] M. A. Davenport and M. B. Wakin, "Compressive sensing of analog signals using discrete prolate spheroidal sequences," *Appl. and Computational Harmonic Anal.*, vol. 33, no. 3, pp. 438–472, 2012.

[49] S. Şenay, J. Oh, and L. F. Chaparro, "Regularized signal reconstruction for level-crossing sampling using Slepian functions," *Signal Process.*, vol. 92, no. 4, pp. 1157–1165, 2012.

[50] S. Şenay, L. F. Chaparro, and L. Durak, "Reconstruction of nonuniformly sampled time-limited signals using prolate spheroidal wave functions," *Signal Process.*, vol. 89, no. 12, pp. 2585–2595, 2009.

[51] R. Demesmaeker, M. G. Preti, and D. Van De Ville, "Augmented Slepians: Bandlimited functions that counterbalance energy in selected intervals," *IEEE Trans. on Signal Process.*, vol. 66, no. 15, pp. 4013–4024, 2018.

[52] G. G. Walter and X. Shen, "Sampling with prolate spheroidal wave functions," *Sampling Theory in Signal and Image Process.*, vol. 2, no. 1, pp. 25–52, 2003.

[53] K. Khare and N. George, "Sampling theory approach to prolate spheroidal wavefunctions," *J. Phys. A: Math. and General*, vol. 36, no. 39, p. 10011, 2003.

[54] D. Cheng and K. I. Kou, "Novel sampling formulas associated with quaternionic prolate spheroidal wave functions," *Advances in Appl. Clifford Algebras*, vol. 27, no. 4, pp. 2961–2983, 2017.

[55] S. Şenay, L. F. Chaparro, M. Sun, and R. J. Sclabassi, "Compressive sensing and random filtering of EEG signals using Slepian basis," in *Proc. 16th Eur. Signal Process. Conf., 2008.* IEEE, Aug. 2008, pp. 1–5.

[56] N. Hoogenboom, J.-M. Schoffelen, R. Oostenveld, L. M. Parkes, and P. Fries, "Localizing human visual gamma-band activity in frequency, time and space," *Neuroimage*, vol. 29, no. 3, pp. 764–773, 2006.

[57] B. R. Frieden, "VIII evaluation, design and extrapolation methods for optical signals, based on use of the prolate functions," in *Progress in Opt.* Elsevier, 1971, vol. 9, pp. 311–407.

[58] D. J. Thomson, "Spectrum estimation and harmonic analysis," *Proceedings of the IEEE*, vol. 70, no. 9, pp. 1055–1096, 1982.

[59] T. P. Bronez, "Spectral estimation of irregularly sampled multidimensional processes by generalized prolate spheroidal sequences," *IEEE Transactions on Acoustics, Speech, and Signal Processing*, vol. 36, no. 12, pp. 1862–1873, 1988.

[60] A. Hanssen, "Multidimensional multitaper spectral estimation," *Signal Processing*, vol. 58, no. 3, pp. 327–332, 1997.

[61] T.-C. Liu and B. Van Veen, "Multiple window based minimum variance spectrum estimation for multidimensional random fields," *IEEE Transactions on signal processing*, vol. 40, no. 3, pp. 578–589, 1992.

[62] I. Daubechies, "Time-frequency localization operators: a geometric phase space approach," *IEEE Transactions on Information Theory*, vol. 34, no. 4, pp. 605–612, 1988.

[63] C. D. Beggan, J. Saarimäki, K. A. Whaler, and F. J. Simons, "Spectral and spatial decomposition of lithospheric magnetic field models using spherical Slepian functions," *Geophys. J. Int.*, vol. 193, no. 1, pp. 136–148, 2013.

[64] F. A. Dahlen and F. J. Simons, "Spectral estimation on a sphere in geophysics and cosmology," *Geophys. J. Int.*, vol. 174, pp. 774–807, 2008.

[65] F. J. Simons and F. Dahlen, "Spherical Slepian functions and the polar gap in geodesy," *Geophys. J. Int.*, vol. 166, no. 3, pp. 1039–1061, 2006.

[66] M. J. Evans, J. A. Angus, and A. I. Tew, "Analyzing head-related transfer function measurements using surface spherical harmonics," *J. Acoust. Soc. America*, vol. 104, no. 4, pp. 2400–2411, 1998.

[67] A. P. Bates, Z. Khalid, and R. A. Kennedy, "On the use of Slepian functions for the reconstruction of the head-related transfer function on the sphere," in *Proc. 9th IEEE Int. Conf. Signal Process. Commun. Syst., ICSPCS 2015,*. IEEE, Dec. 2015, pp. 1–7.

[68] F. J. Simons, "Slepian functions and their use in signal estimation and spectral analysis," in *Handbook of Geomathematics*. Springer, 2010, pp. 891–923.

[69] A. Plattner and F. J. Simons, "Potential-field estimation using scalar and vector Slepian functions at satellite altitude," *Handbook of Geomathematics*, pp. 2003–2055, 2014.

[70] L. Longuevergne, B. R. Scanlon, and C. R. Wilson, "GRACE hydrological estimates for small basins: Evaluating processing approaches on the high plains aquifer, usa," *Water Resources Research*, vol. 46, no. 11, 2010.

[71] M. Tsitsvero, S. Barbarossa, and P. Di Lorenzo, "Signals on graphs: Uncertainty principle and sampling," *IEEE Trans. Signal Process.*, vol. 64, no. 18, pp. 4845–4860, 2016.

[72] D. Van De Ville, R. Demesmaeker, and M. G. Preti, "When Slepian meets fiedler: Putting a focus on the graph spectrum," *IEEE Signal Process. Lett.*, vol. 24, no. 7, pp. 1001–1004, 2017.

[73] R. Liégeois, I. Merad, and D. Van De Ville, "Time-resolved analysis of dynamic graphs: an extended Slepian design," in *Wavelets and Sparsity XVIII*, vol. 11138. International Society for Optics and Photonics, 2019, p. 1113810.

[74] M. Petrović and D. Van De Ville, "Slepian guided filtering of graph signals," in *Wavelets and Sparsity XVIII*, vol. 11138. International Society for Optics and Photonics, 2019, p. 111380D.

[75] A. P. Bates, Z. Khalid, and R. A. Kennedy, "Efficient computation of Slepian functions for arbitrary regions on the sphere," *IEEE Trans. Signal Process.*, vol. 65, no. 16, pp. 4379–4393, 2017.

[76] F. J. Simons, J. C. Hawthorne, and C. D. Beggan, "Efficient analysis and representation of geophysical processes using localized spherical basis functions," in *Wavelets XIII*, vol. 7446. International Society for Optics and Photonics, 2009, p. 74460G.

[77] F. J. Simons and A. Plattner, "Scalar and vector Slepian functions, spherical signal estimation and spectral analysis," in *Handbook of Geomathematics: Second Edition*. Springer Berlin Heidelberg, 2015, pp. 2563–2608.

[78] Z. Khalid, S. Durrani, P. Sadeghi, and R. A. Kennedy, "Spatio-spectral analysis on the sphere using spatially localized spherical harmonics transform," *IEEE Trans. Signal Process.*, vol. 60, no. 3, pp. 1487–1492, Mar. 2012.

[79] W. Freeden, M. Z. Nashed, and M. Schreiner, *Spherical Sampling*. Springer, 2018.

[80] N. Sneeuw, "Global spherical harmonic analysis by least-squares and numerical quadrature methods in historical perspective," *Geophys. J. Int.*, vol. 118, no. 3, pp. 707–716, Sep. 1994.

[81] R. G. Crittenden and N. G. Turok, “Exactly azimuthal pixelizations of the sky,” *Arxiv preprint astro-ph/9806374*, 1998.

[82] M. J. Mohlenkamp, “A fast transform for spherical harmonics,” *J. Fourier Anal. and Appl.*, vol. 5, no. 2-3, pp. 159–184, 1999.

[83] A. G. Doroshkevich, P. D. Naselsky, O. V. Verkhodanov, D. I. Novikov, V. I. Turchaninov, I. D. Novikov, P. R. Christensen, and Chiang, “Gauss – Legendre Sky Pixelization (GLESP) for CMB maps,” *Int. J. Mod. Phys. D.*, vol. 14, no. 02, pp. 275–290, Feb. 2005.

[84] D. M. Healy, Jr., D. Rockmore, P. J. Kostelec, and S. S. B. Moore, “FFTs for the 2-sphere - improvements and variations,” *J. Fourier Anal. and Appl.*, vol. 9, pp. 341–385, 2003.

[85] J. D. McEwen and Y. Wiaux, “A novel sampling theorem on the sphere,” *IEEE Trans. Signal Process.*, vol. 59, no. 12, pp. 5876–5887, Dec. 2011.

[86] J. Keiner, S. Kunis, and D. Potts, “Efficient reconstruction of functions on the sphere from scattered data,” *J. Fourier Anal. Appl.*, vol. 13, no. 4, pp. 435–458, May 2007.

[87] P. J. Kostelec and D. N. Rockmore, “FFTs on the rotation group,” *J. Fourier Anal. and Appl.*, vol. 14, pp. 145–179, Apr. 2008.

[88] J. D. McEwen, “Fast, exact (but unstable) spin spherical harmonic transforms,” *All Res. J. Phys.*, vol. 1, no. 1, 2011.

[89] K. M. Górski, E. Hivon, A. J. Banday, B. D. Wandelt, F. K. Hansen, M. Reinecke, and M. Bartelmann, “HEALPix: A Framework for High-Resolution Discretization and Fast Analysis of Data Distributed on the Sphere,” *Astrophys. J.*, vol. 622, pp. 759–771, Apr. 2005.

[90] J. Blais and M. Soofi, “Spherical harmonic transforms using quadratures and least squares,” in *Computational Science – ICCS 2006*, ser. Lecture Notes in Computer Science. Springer Berlin Heidelberg, 2006, vol. 3993, pp. 48–55.

[91] K. M. Huffenberger and B. D. Wandelt, “Fast and exact spin-s spherical harmonic transforms,” *Astrophys. J. Supp.*, vol. 189, no. 2, pp. 255–260, Aug. 2010.

[92] Reinecke, M. and Seljebotn, D. S., “Libsharp - spherical harmonic transforms revisited,” *Astron. & Astrophys.*, vol. 554, p. A112, 2013.

[93] W. Skukowsky, “A quadrature formula over the sphere with application to high resolution spherical harmonic analysis,” *J. Geodesy*, vol. 60, no. 1, pp. 1–14, Mar. 1986.

[94] C. Tscherning, R. Forsberg, A. Albertella, F. Migliaccio, and F. Sanso, “The polar gap problem,” *Space-wise approaches to gravity field determination in Polar areas, Eotvos to mGal, Finsal report*, vol. 10, pp. 331–336, 2000.

[95] F. G. Lemoine, N. K. Pavlis, S. C. Kenyon, R. H. Rapp, E. Pavlis, and B. Chao, “New high-resolution model developed for Earth’s gravitational field,” *Eos, Transactions American Geophysical Union*, vol. 79, no. 9, pp. 113–118, 1998.

[96] R. Forsberg, A. Olesen, F. Ferraccioli, T. Jordan, and K. Matsuoka, “Airborne geophysical surveys of unexplored regions of Antarctica-results of the ESA polargap campaign,” in *AGU Fall Meeting Abstracts*, 2016.

[97] M. Tegmark, “A method for extracting maximum resolution power spectra from microwave sky maps,” *Monthly Notices of the Royal Astronomical Society*, vol. 280, no. 1, pp. 299–308, 1996.

[98] G. Lewsi. (2014, Aug.) Cosmic radiation: the dawn of new physics or statistical slip-up? [Online]. Available: https://phys.org/news/2014-08-cosmic-dawn-physics-statistical-slip-up.html

[99] N. Sneeuw and M. Van Gelderen, “The polar gap,” in *Geodetic boundary value problems in view of the one centimeter geoid.* Springer, 1997, pp. 559–568.

[100] Q. Jin, Z. Luo, and K. M. Wong, "An optimum complete orthonormal basis for signal analysis and design," *IEEE Trans. Inf. Theory*, vol. 40, no. 3, pp. 732–742, May 1994.

[101] Z. Khalid and R. A. Kennedy, "Maximal multiplicative spatial-spectral concentration on the sphere: Optimal basis," in *2015 IEEE International Conference on Acoustics, Speech and Signal Processing (ICASSP)*. IEEE, 2015, pp. 4160–4164.

[102] R. O. Duda and W. L. Martens, "Range-dependence of the HRTF for a spherical head," in *Proceedings of 1997 Workshop on Applications of Signal Processing to Audio and Acoustics*, Oct 1997, pp. 5 pp.–.

[103] I. Gradshteyn, I. Ryzhik, and R. H. Romer, "Tables of integrals, series, and products," 1988.